SLAC-143

A Study of Non-Strange Boson Resonances Produced by Quasi-Monochromatic Photon Beams of Energies Between 4.3 and 7.5 GeV in a Hydrogen Bubble Chamber

Michael M. Menke

SLAC Report No. 143

December 1971

AEC Contract AT(04-3)-515

STANFORD LINEAR ACCELERATOR CENTER
Stanford University • Stanford, California

DISCLAIMER

SLAC-143
UC-34
(EXP)

A STUDY OF NON-STRANGE BOSON RESONANCES PRODUCED BY QUASI-MONOCHROMATIC PHOTON BEAMS OF ENERGIES BETWEEN 4.3 AND 7.5 GeV IN A HYDROGEN BUBBLE CHAMBER

MICHAEL M. MENKE

STANFORD LINEAR ACCELERATOR CENTER

STANFORD UNIVERSITY

Stanford, California 94305

PREPARED FOR THE U. S. ATOMIC ENERGY COMMISSION UNDER CONTRACT NO. AT(04-3)-515

December 1971

Printed in the United States of America. Available from National Technical Information Service, U. S. Department of Commerce, 5285 Port Royal Road, Springfield, Virginia 22151.
Price: Printed Copy $3.00; microfiche $0.95.

ABSTRACT

The photoproduction of resonances has been studied in three exposures of a hydrogen bubble chamber to positron annihilation radiation of 4.3, 5.25 and 7.5 GeV nominal energies. The general analysis procedure and results on the three-prong event topology are presented. We study the highly constrained reaction $\gamma p \longrightarrow p\pi^+\pi^-$ over the energy range 2-8 GeV and the reactions $\gamma p \longrightarrow p\pi^+\pi^-\pi^o$ and $\gamma p \longrightarrow \pi^+\pi^+\pi^-n$ at the annihilation energies. Cross sections are given. Using various models to parameterize ρ^o photoproduction in $\gamma p \longrightarrow p\pi^+\pi^-$, the mean t-slope found is 7.0 ± 0.4 GeV^{-2}, while the ρ^o forward cross section decreases from about 130μb/GeV^2 at 3.3 GeV to about 100μb/GeV^2 at 7.5 GeV. The cross section for $\gamma p \longrightarrow \omega p$ is decomposed into an OPE and a diffractive part, which is found to be $1.5 \pm 0.3\mu$b. $(d\sigma(\rho)/dt)/(d\sigma(\omega)/dt)|_{t=0}$ is then 9.4 ± 2.3 at 7.5 GeV. In comparing $d\sigma/dt$ for vector meson production with that of Compton scattering via VDM for photon energies above 4 GeV, we find that for $\gamma_\rho^2/4\pi = 0.32 \pm 0.03$ there is good agreement at all s and t. This same value of $\gamma_\rho^2/4\pi$ relates our forward ρ^o cross sections to $\sigma_T(\gamma p)$ at all our energies. A search for $\rho' \longrightarrow 2\pi$ finds, at the 90% confidence level, $\sigma_{\rho'}(1250) < 0.3\mu$b and $\sigma_{\rho'}(1650) < 0.1\mu$b per 100 MeV width. Inelastic peripheral ρ^o production is seen in both the proton and the neutron channels, but with present statistics specific nucleon isobars cannot be associated with it. The quasi-two body reactions $\gamma p \longrightarrow \pi^-\Delta^{++}$, $\rho^-\Delta^{++}$, and $A_2^+ n$ are observed, with cross sections decreasing with photon energy like E_γ^{-a}. For the first two $a = 1.74 \pm 0.16$ and 0.6 ± 0.2 respectively, indicating that they are unlikely to have the same production mechanism. It follows that if the reaction $\gamma p \longrightarrow \rho^-\Delta^{++}$ is due to an OPE process, the required rho radiative decay width ($\sim$0.5 MeV) is much in excess of the value predicted by SU(3).

ACKNOWLEDGEMENTS

It is a pleasure to acknowledge the contributions of the many people who made this experiment possible. The experiment was carried out under the general direction of Dr. George Chadwick, who has been a major source of help and understanding both in matter of physics and in the many technical details of bubble chamber analysis. Other major sources of advice and co-operation were Drs. Yehuda Eisenberg, Peter Seyboth and Arie Shapira, all members of the collaboration which carried out the experiment. Much help and advice in the early phases of the work came from Drs. Aahron Levy and Gunter Wolf. Others who made material contributions at various stages are Drs. Zaven Guiragossian, Paul Klein, Ken Moffeit, William Podolsky, Ian Skillicorn, and Tai Ho Tan. Special thanks are due to my thesis supervisor, Professor Joseph Ballam, for his patience, constantly receptive attitude and aid in matters not only of physics but of personal life. Valuable comments and criticisms of this work have been received from the co-signers, Profs. William Bardeen and Mason Yearian.

The hospitality and support of my research by SLAC for the past several years has been greatly appreciated. I especially appreciate the conductive atmosphere created by the many people of SLAC, particularly those in Group B and the Theory Group. Helpful advice and consultations have been received from Profs. Fred Gilman, Haim Harari, David Leith and Adam Schwimmer. Also I appreciate the continual support and encouragement of the Stanford Physics Department during my graduate career here.

The help and cooperation of the SLAC Accelerator Operations Group and of Bob Watt and the 40" bubble chamber crew were superb. Special credit goes to all the scanners at SLAC, the Weizman Institute and Tel Aviv

University who diligently performed the task of locating and measuring the hadronic events in a nearly overwhelming background of uninteresting events (see Fig. II. 1). The help in data reduction and management from Ken Eyeman and Madge Tartar is also greatly appreciated. I also received friendly co-operation from the staff of our SLAC computation facility.

TABLE OF CONTENTS

LIST OF TABLES

FIGURE CAPTIONS

CHAPTER I

INTRODUCTION

Photoproduction and strong interaction physics have been closely related since the beginning of systematic experimentation using high energy accelerators. From unitarity and time reversal invariance alone it has been shown that the phases of the single pion photoproduction amplitude and the pion nucleon elastic scattering amplitude agree modulo pi below the threshold for two pion production. This result, known as the Watson theorem, is not sufficient to calculate the photoproduction amplitude in terms of elastic pion nucleon scattering, but it serves as a guide to the possible solution and illustrates the close connection between these two processes. Therefore it is not surprising that low energy photoproduction gave the first evidence of the pion nucleon resonance in the spin-isospin state (3/2, 3/2). Moreover, photoproduction data has helped to resolve ambiguities in the pion nucleon phase shifts, such as whether to use the Fermi or the Yang sign convention, and may be essential in disentangling the complex of nucleon isobar states above the (3/2, 3/2) resonance.

When photon beams of energy and intensity sufficient to produce significant numbers of multi-pion final state events became available, photoproduction proved a valuable method to examine the properties of pion-pion and multi-pion interactions and resonances, especially those with the same quantum numbers as the photon itself. Such resonant states are called neutral vector mesons. Their dominant role in photoproduction first became apparent with the experiments at the Cambridge Electron Accelerator (CEA) and

the Deutsches Electronen-Synchotron (DESY) in the mid-1960's. These experiments revealed that the neutral rho meson dominated the final state $p\pi^+\pi^-$ while the omega meson was the most significant effect seen in the final state $p\pi^+\pi^-\pi^o$. These same resonances were present in the five and six body final states, respectively. The utility of these experiments, however, was limited by their use of bremsstrahlung beams which provide no a priori photon energy determination and produce mostly low energy events. Clearly, a new type of photon beam was needed to extend these results to higher energies and to obtain the higher statistics necessary.

Therefore the first bubble chamber experiment performed at the Stanford Linear Accelerator Center (SLAC) was in fact a series of photoproduction exposures[1-7] using the SLAC positron annihilation radiation beam.[8] This beam produced high energy, monochromatic gamma rays to be used for photoproduction experiments in the SLAC 40" bubble chamber filled with liquid hydrogen. The previous bubble chamber experiments[9,10] and streamer chamber studies[11] yielded interesting information on the photoproduction of the neutral vector mesons ρ^o, ω, and ϕ, as well as some glimpses of more complicated photoproduction reactions in 4, 5, and 6 body final states, but were limited by lack of knowledge of the incoming photon energy. The present work had two distinct advantages over previous experiments which had only bremsstrahlung as a technique to produce high energy photons. First, the energy of the annihilation photons was known to ±2%, allowing constrained fits to be made to events with one or more neutral particles in the final state. Second, the monochromatic photons increased the yield of interesting high energy events relative to the bremsstrahlung induced events, most of which come from much lower energy photons. Furthermore, the annihilation

energy allowed the calculation (rather than the assumption that is necessary in the unconstrained fit) of a missing mass for the neutral system. This then allowed a clean separation of events with a single neutral particle in the final state from multineutral production, which has subsequently yielded a more complete picture of resonance photoproduction.

One of the outstanding questions in photoproduction physics has been the mechanism of neutral vector meson production. In addition to the track chamber experiments[9-11] mentioned above, this topic has been the subject of numerous counter studies.[12] These studies all indicated that ρ^o photoproduction is diffractive, maintaining a relatively constant cross section in the s channel center of mass system for $|t|$ up to 0.5 GeV^2. The shape of the rho, however, was found to be strongly skewed toward low dipion masses, and no fundamental explanation for this was known. The omega cross section, on the other hand, was found to be falling with energy in a way consistent with a combination of diffractive plus one pion exchange (OPE) production mechanisms. In addition, some evidence was seen for production of other resonances in 4 and higher body final states. For example, the associated production of $\rho^-\Delta^{++}$ in the four body final states was observed to decrease with energy. It was therefore thought to proceed via OPE and was used to estimate the radiative decay width of the rho into a pion and a gamma. Other resonances, like the A_2 meson, which had been expected with cross sections in the microbarn range were not observed.

The main problems existing in the physics of photoproduction when this experiment was performed can be summarized as follows. First, does the rho cross section remain constant at higher energies than those observed in the first photoproduction experiments, and is there continued indication

for s-channel helicity conservation? Second, what is the reason for the skewed shape of the neutral rho, how should ρ^0 cross sections be derived from the raw data on the reaction $\gamma p \longrightarrow p\pi^+\pi^-$, and what do these various models imply for the forward ρ^0 cross sections? Third, does the vector dominance model (VDM) accurately describe the photoproduction of vector mesons on hydrogen, and if so, what is the value of the photon-vector meson coupling constant (which appears to disagree when obtained by photoproduction in heavy nuclei[12] and by electron-positron annihilation into vector mesons[13]), and what are the subsequent implications for VDM?[14] Fourth, are there higher mass recurrences of the neutral rho in the dipion mass spectrum as predicted by the Veneziano model?[15] Fifth, do the diffractive and OPE parts of the omega production mechanism correspond to the SU(3) prediction and that expected from the known radiative decay width of the omega meson? Sixth, are there additional boson resonances produced in final states with at least one neutral particle, and if so what can be learned about their production mechanisms? The solution to many of these problems was tied to improved experimental techniques, because of the serious limitations imposed by using bremsstrahlung beams.

This experiment has been able to shed some light on most of the above questions, although certain basic theoretical questions like the differences between the rho meson observed in photoproduction and that observed in hadronic production and the reason for its apparently skewed shape remain unsolved. More specifically, the new contributions of this experiment to photoproduction physics are summarized briefly in the abstract and reviewed in some detail in the conclusion, where our results are compared to a great number of other experimental observations and theoretical

predictions.[16-24]

The SLAC annihilation radiation beam was produced by creating positrons from electrons at a point 1/3 of the way along the accelerator. The resulting positrons were then accelerated along the remaining 2/3 of the accelerator and finally allowed to annihilate in a liquid hydrogen target. The resulting annihilation photons obey two body kinematics and have an energy determined uniquely by their production angle and the incident positron energy. A residual bremsstrahlung background was still present, but the resulting photons were collimated at an angle chosen to enhance the monochromatic photons relative to this background.

Exposures were made at three mean annihilation photon energies, 4.3, 5.25, and 7.5 GeV. The experiment was performed as a collaboration of groups from SLAC, the Weizmann Institute of Science and Tel Aviv University. The 4.3 GeV film was measured and analyzed by the Weizmann Institute group, the 5.25 GeV film by the SLAC group and the 7.5 GeV film by all three groups. Since close collaboration was maintained during both the data taking and analysis phases of the experiment, all the data are presented as if from a single experiment. This not only enhances the statistical accuracy, but further permits an analysis of the energy dependence of resonance photoproduction, giving important clues to the production mechanisms as discussed above.

Since this beam was developed, other new techniques have become available for producing high energy photon beams. One such method employs laser photons which both receive a large amount of energy and maintain a high degree of polarization when they are backscattered off a high energy electron beam.[25] This method gives a high degree of

monochromaticity and polarization, but is limited by the power and repetition rate of current lasers. Hence, this technique is most suitable for detectors like the bubble chamber which also have a slow period but obtain more complete information. Such a beam has been developed at SLAC[26] and used in the 82 inch hydrogen bubble chamber. Preliminary data from this work have been published[27-32] and have provided a great deal of stimulation to our own work.

The number of pictures at various energies, the parameters of the electron beam, and the number of events measured are given in Table I. The experimental details of the beam, the bubble chamber, and analysis procedures are discussed in Chapter II. The determination of the channel cross sections and corrections for various backgrounds is discussed in Chapter III. The subsequent chapters describe the investigation of resonance photoproduction, explaining how these results were derived and comparing our data with other experimental data as well as various theoretical models.

TABLE I

Parameters and statistics of the three exposures.

Central photon energy (GeV)	4.3	5.25	7.5
Resolution (%)	±2.0	±2.0	±2.0
Positron energy (GeV)	8.5	10.0	12.0
Central production angle (mrad)	11.9	9.4	7.15
Photons/frame, $k > 0.9\, k_A$	~54	~70	~30
Total pairs/frame in scanning volume	15.8	16.2	11.7
Total frames	300K	252K	~940K
Total events measured	10178	9153	~24000

CHAPTER II

EXPERIMENTAL APPARATUS AND PROCEDURES

II. 1 The Hydrogen Bubble Chamber

The first comprehensive studies of multibody, high energy photoproduction were carried out in 1964-1966 using hydrogen bubble chambers at the Cambridge Electron Accelerator[9] (CEA) and the Deutsches Electronen-Synchotron[10] (DESY). The bubble chamber allows the observation of all charged tracks, secondary interactions on hadronic tracks, vertices of the interactions, and the decay of many strange particles. Therefore it is relatively simple to separate hadronic events from electromagnetic ones and further to classify events according to the number of hadrons produced. A bubble chamber picture containing a hadronic event from this experiment is shown in Fig. II. 1. The bubble density along hadronic tracks allows the ionization to be used to separate protons from kaons and pions in certain restricted but very useful momentum ranges, according to the approximate relation

$$I(p) = I(\min)\ (1 + m^2/p^2)\,, \qquad \text{(II. 1)}$$

where m is the particle mass and p is its momentum. Because the bubble chamber views a 4π geometry, there are no severe geometrical biases and therefore no complicated acceptances to be folded into the experimental data in order to obtain cross sections and angular distributions. For all these reasons, the bubble chamber is particularly well suited to exploratory experiments in which a wide range of properties is to be studied.

There are several disadvangages in studying photoproduction with the bubble chamber technique. First, a photograph must be taken on each beam

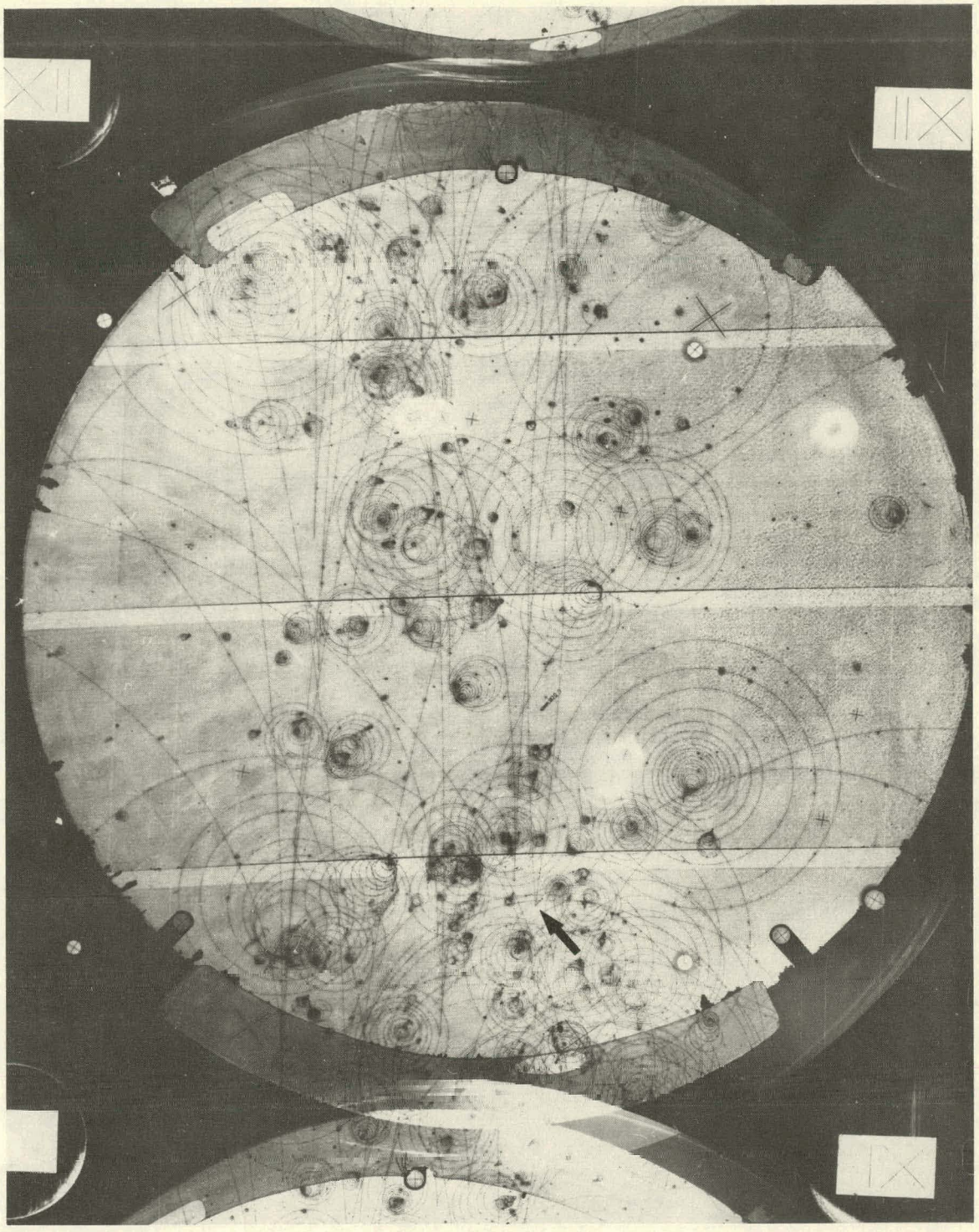

FIG. II. 1--A bubble chamber picture of a photoproduced three-prong hadronic event, which illustrates the copious background of electromagnetic events and the subsequent difficulty in isolating events with short proton tracks. The hadronic event originates just before the first of the three obvious lines crossing the bubble chamber in about the center of the chamber. The proton track is very short and highly ionized, whereas the pion tracks are minimum ionizing like the electromagnetic background and form a characteristic "fishtail" pattern which usually indicates a high energy, low momentum transfer event, a likely candidate for the reaction $\gamma p \longrightarrow \rho^{o} p$.

pulse, whether or not it contains a hadronic event, because it has proved extremely difficult to trigger a bubble chamber of standard construction on interesting photoproduced reactions. Furthermore, the purely electromagnetic processes such as pair production occur with a much higher probability (200 times higher) than photoproduction involving hadrons when high energy photons irradiate hydrogen. Since only a limited number of positron-electron pair, Compton electron and delta ray tracks can be tolerated before the hadronic events become obscured, it has proved necessary to reduce the flux in such exposures to a level where less than one picture in ten contains a hadronic event. This increases both the number of pictures needed to obtain a useful sample of events and the amount of scanning necessary to extract them. Second, and related to this large electromagnetic background, is the difficulty in observing events with very short proton tracks. An event with three charged hadronic tracks, one of which is a proton of very low momentum (140 MeV/c corresponds to a range of 1 cm in liquid hydrogen), is easily overlooked by scanners who can confuse these events with the dominant background of electron-positron pairs. In both the CEA and DESY experiments these scanning losses due to the "invisible" protons occured for $|t(p,p)| < 0.04$ $(GeV/c)^2$. Most of these events correspond to forward ρ^o production, which has been the subject of several counter studies covering the region where bubble chambers experience the most significant scanning losses. From counter experiments,[12] there is some evidence on how to correct the forward losses in the bubble chamber data, but it is still not completely understood. The method adopted in this and all other bubble chamber experiments to date has been to make a linear exponential extrapolation of $d\sigma/dt$ in the forward direction.

The SLAC 40" hydrogen bubble chamber is cyclindrical with a visible diameter of 1 meter and a depth of 50 cm. A schematic diagram of this chamber is shown in Fig. II.2. The piston expansion system has a reflective surface providing bright field illumination in the chamber. The light comes from circular flash lamps surrounding each camera lens. A very important feature of this chamber for photoproduction is the pair of large, thin aluminum beam windows. The area of these windows is 6.5" x 28" with total thickness 0.04", corresponding to less than 0.01 radiation lengths, which limits pair production from the chamber windows to less than 1/9 of those made in the hydrogen of the chamber. The large area of the beam windows was instrumental in allowing a useful flux of photons into the chamber, spread out so that events would not be obscured. The central magnetic field setting for this exposure was approximately 26 Kg and the field was uniform over the illuminated volume to 4%. The repetition rate in this experiment varied from 1 to 1.5 pulses per second.

The chamber is viewed by three camera lenses set on an equilateral triangle about 70 cm on a side. The lenses are mounted on a steel plate 10 cm thick, assuring a fixed relative position. The distance from the camera lens to the mid-plane of the chamber was 245.5 cm in space, resulting in a 17 degree stereo angle. The materials which cause the optical path to vary from the physical distance are the chamber window (Schottglass BK 7) and the quartz viewing ports. The lenses gave a demagnification of 1:17. The chamber is illuminated by flash tubes which surround the lenses. The light is reflected back to the camera by Scotchlite, a retrodirective material glued to a dish attached to the chamber piston. The reflected light after passing through the camera lens is bent by a 45 degree mirror and focussed on the

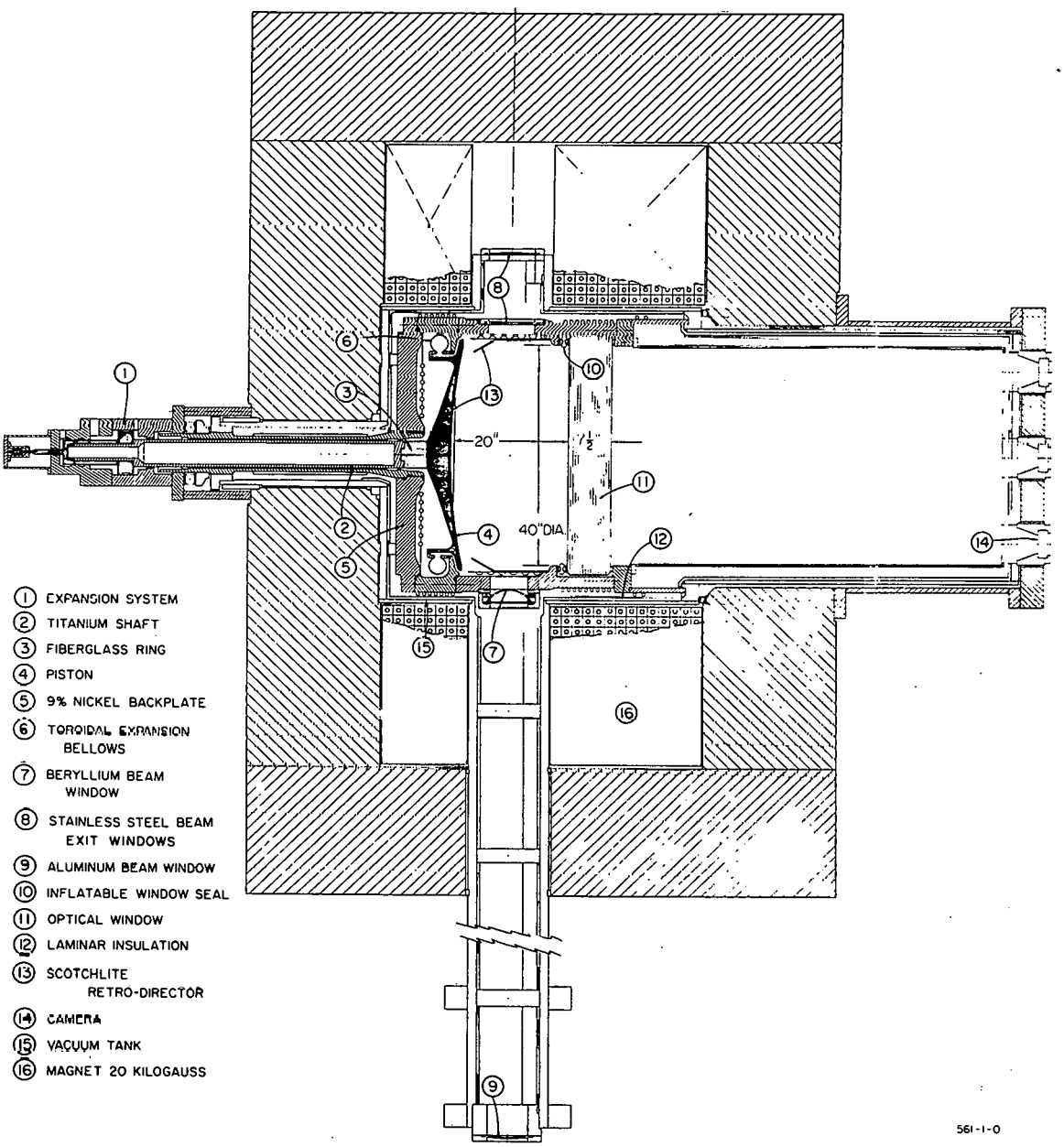

① EXPANSION SYSTEM
② TITANIUM SHAFT
③ FIBERGLASS RING
④ PISTON
⑤ 9% NICKEL BACKPLATE
⑥ TOROIDAL EXPANSION BELLOWS
⑦ BERYLLIUM BEAM WINDOW
⑧ STAINLESS STEEL BEAM EXIT WINDOWS
⑨ ALUMINUM BEAM WINDOW
⑩ INFLATABLE WINDOW SEAL
⑪ OPTICAL WINDOW
⑫ LAMINAR INSULATION
⑬ SCOTCHLITE RETRO-DIRECTOR
⑭ CAMERA
⑮ VACUUM TANK
⑯ MAGNET 20 KILOGAUSS

FIG. II.2--Horizontal cross-section of the SLAC 40-inch bubble chamber.

film plane. The film format was single strip, three view, on 70 mm perforated film.

In addition to the problems of studying photoproduction in a bubble chamber discussed above, the CEA and DESY experiments suffered from a further serious handicap since their bremsstrahlung beams delivered photons of unknown momentum. This is not a problem unique to bubble chambers, but rather a problem in using bremsstrahlung to produce photon beams. For charged particles, momentum analyzing crossed field and radio frequency separators can produce beams of very pure momentum and particle content. For neutrons and neutral K mesons time of flight techniques can give information on the beam momentum, but a photon beam can not be analyzed after it is created since it is both neutral and massless. In particular, for bremsstrahlung beams only an upper limit on the photon energy is known; furthermore, the bremsstrahlung spectrum is strongly weighted toward low energies, so that of the total reactions studied, relatively few are at high energy.

Because of these problems, photoproduction experiments using bremsstrahlung beams were able to study in detail only those channels in which all the particles produced were visible, so the 3-constraint fits were possible, or those containing very narrow and prominent resonances like the omega meson, and their statistics were strongly weighted toward low energy interactions. For events with one or more missing neutrals, the hypothesis with only a single neutral in the final state can always be fit by adjusting the incident energy in the 0-C fit. Hence it was very difficult in these experiments to do detailed studies of channels in which any of the particles are not observed. Although events at the tip of the bremsstrahlung spectrum and very narrow and well separated resonances like the omega

could be studied in more detail, new approaches were clearly needed for the creation of photon beams. One possible method involves tagging the photons at the time of the bremsstrahlung process by observing the scattered electron. This has been used successfully in doing several total cross section experiments.[21] Other approaches involve novel methods of creating the photon beams themselves, in such a way as to approach the ideal of a monochromatic beam. One such approach, which was used for this experiment, is summarized in the next section. A recent, and even more versatile method, which has been used in photoproduction experiments with great success is the backscattering of a laser beam from the SLAC electron beam to produce high energy, monochromatic, polarized photons.[26]

II. 2 The Annihilation Radiation Beam

In 1960 D. M. Binnie[33] observed that since the cross section for bremsstrahlung decreases much more rapidly with photon production angle than the cross section for positron annihilation in flight, it would be feasible to construct a quasi-monochromatic photon beam by impinging a well defined positron beam on a liquid hydrogen target and accepting through a collimator only a conical shell of photons, the inner angle of which would greatly exceed the characteristic angle m/E of the bremsstrahlung process. This effectively excludes most of the strongly forward-peaked bremsstrahlung (see Fig. II. 3). For the annihilation of a positron of energy E and mass m into two photons, one of which has energy K and laboratory angle θ with respect to the incident positron beam, one obtains the energy-angle relationship (for $E >> m$)

$$K = \frac{E}{1 + E\theta^2/2m} \quad . \qquad \text{(II. 2)}$$

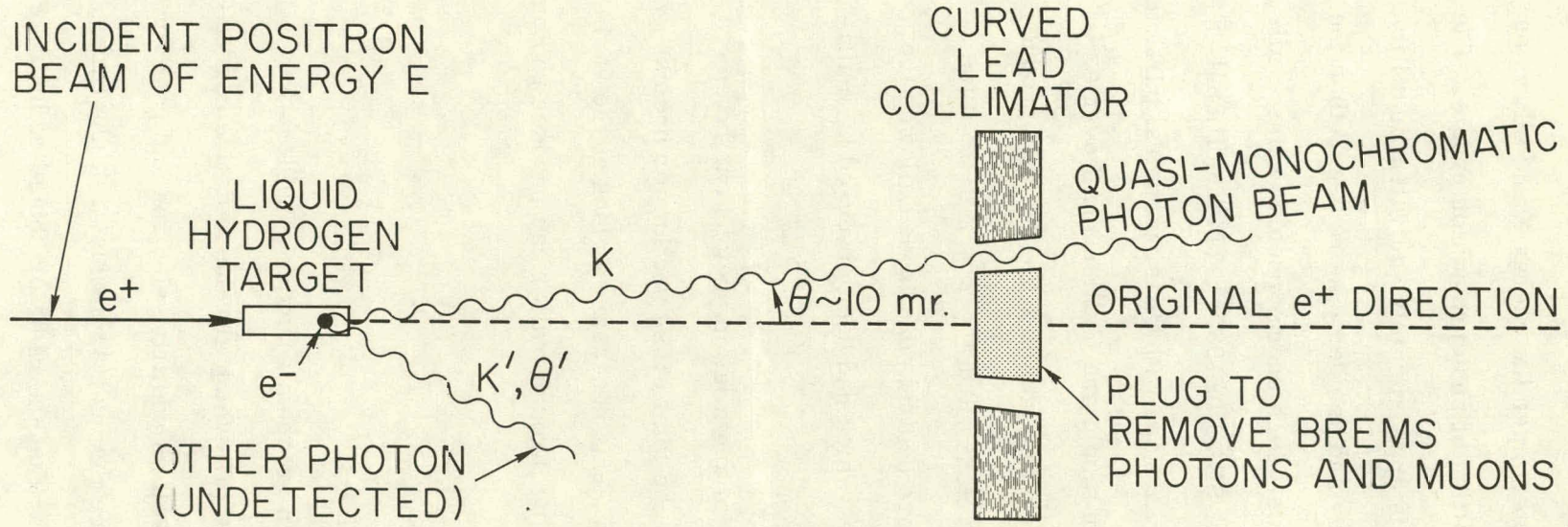

TWO BODY ANNIHILATION ENERGY FORMULA:

$$K = \frac{E}{1 + \frac{E}{M}\frac{\theta^2}{2}}$$

FIG. II. 3-- Schematic layout of a positron annihilation radiation beam.

Thus defining the production angle θ determines the energy K and allows an energy constraint to be applied in the fitting of photoproduction events. The high energy component of such a beam is approximately equivalent in utility to a charged beam of well defined energy and decidedly more useful than the bremsstrahlung beams which were the only high energy photon beams available until this beam was implemented at SLAC in 1967.[8] This additional constraint aids in the identification of reactions with missing neutral particles, in particular the discrimination between single and multi-neutral events. This ability to isolate relatively pure reaction samples for the photoproduction channels $p\pi^+\pi^-\pi^o$, $\pi^+\pi^+\pi^-n$, $p\pi^+\pi^+\pi^-\pi^-\pi^o$, and $\pi^+\pi^+\pi^+\pi^-\pi^-n$ from the corresponding reactions with two or more neutrals has indeed allowed the observation of several boson resonances which had been obscured by multi-neutral background in previous experiments.

To understand how the intensity of annihilation photons can be enhanced relative to the background when the total cross section for bremsstrahlung is orders of magnitude larger, it is necessary to look at the various processes by which positrons passing through matter can produce photons at an angle theta:

$$\begin{array}{llll} e^+ + e^- \longrightarrow 2\gamma & \text{(a)} & e^+ + e^- \longrightarrow e^+ + e^- + \gamma & \text{(c)} \\ e^+ + e^- \longrightarrow m\gamma \quad m>2 & \text{(b)} & e^+ + Z \longrightarrow e^{'} + Z + \gamma & \text{(d)}. \end{array} \qquad \text{(II. 3)}$$

In addition to the two photon annihilation process (a) under consideration, there are the multi-photon annihilations (b), which are the radiative corrections to the two photon process,[34] as well as positron-electron and positron-nucleus bremsstrahlung (c and d). Since the nuclear bremsstrahlung cross section is proportional to Z^2, it is clear that the radiator should be hydrogen.

Furthermore, there are two types of bremsstrahlung effects which give the main background: direct and indirect. Direct bremsstrahlung is simply wide angle bremsstrahlung at angles one or more orders of magnitude larger than the characteristic angle. Indirect bremsstrahlung is a two step process, a positron scattering, elastically or inelastically, through the photon beam angle followed by bremsstrahlung within the characteristic angle. Both of these processes are strongly peaked in the forward direction, decreasing with angle approximately as dx/x^3 ($x = E\theta/m$), whereas the two body annihilation process decreases only as dx/x.[35] Therefore the ratio of photons from positron annihilation to bremsstrahlung photons increases as x^2. It will be shown that for a reasonable signal to noise ratio, x must be in the range 200-300. For a typical SLAC positron energy, E = 10 GeV, x = 200 implies an annihilation photon energy of 5 GeV and an angle of 10.1 mrad. The choice to run with photon energy just half of the incoming positron energy is explained below.

The cross sections for positron annihilation and direct bremsstrahlung have been evaluated numerically,[36] with the results shown in Fig. II.4.[37] Fig. II.4 shows the ratio of bremsstrahlung photons to annihilation photons expected for two interesting conditions, E(brems) > 1 GeV and E(brems) > 0.02 GeV, with the indirect estimated to be 10% of the direct bremsstrahlung. For photon energies above 2.5 GeV the signal to noise improves rapidly as E increases until E = 2K, beyond which point the curves level off with little further improvement. Hence to optimize the monochromatic signal one should run with K < E/2. The condition K = E/2 is referred to as symmetric annihilation. However, since the maximum energy for a reliable positron beam at SLAC is about 12 GeV, to obtain photon energies higher than 6 GeV

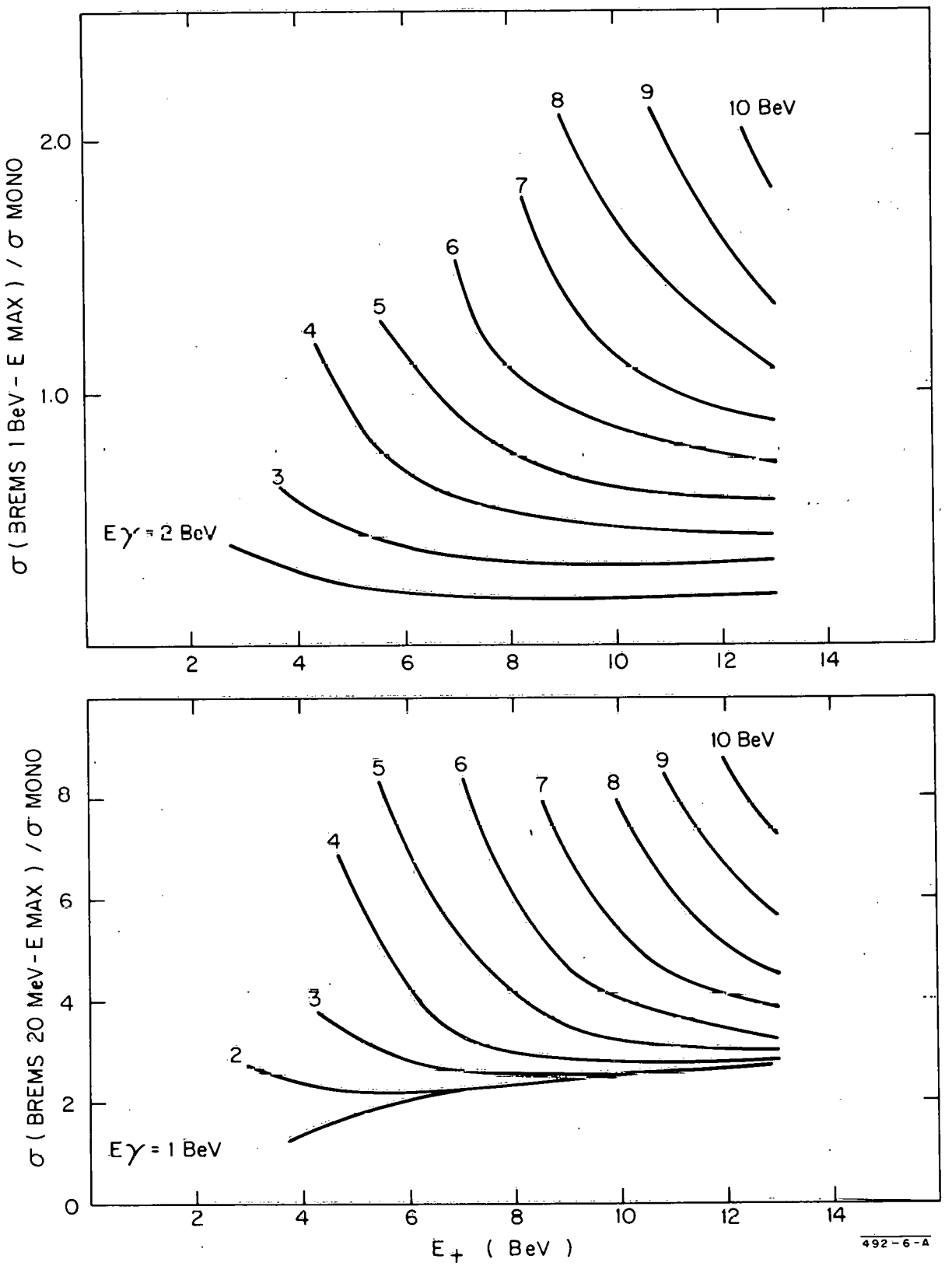

FIG. II.4 -- Noise to signal ratio for annihilation beam as a function of positron energy.

it was necessary to run at slightly less than optimal conditions. The 7.5 GeV spectrum suffered from this as will be seen in the beam spectra for the three exposures.

The limits on the resolution of the photon beam energy K may be due to either angular or momentum uncertainties. Differentiating (II.2),

$$\left.\frac{dK}{K}\right|_{\theta} = \frac{K}{E}\,\frac{dE}{E} \quad \text{and} \quad \left.\frac{dK}{K}\right|_{E} = \frac{-2(E-K)}{E}\,\frac{d\theta}{\theta} \,. \tag{II.4}$$

For symmetric conditions, which give the highest energy obtainable for minimum background, these equations reduce to

$$\left.\frac{dK}{K}\right|_{\theta} = \frac{1}{2}\,\frac{dE}{E} \quad \text{and} \quad \left.\frac{dK}{K}\right|_{E} = -\,\frac{d\theta}{\theta} \,. \tag{II.5}$$

Since the SLAC positron beam can easily obtain a full width $dE/E<1\%$, it works out that the beam energy resolution is dominated by the angular uncertainty $d\theta$. For the 10 GeV positron beam ($\theta = 0.01$ rad.), the beam will have $\pm 1\%$ resolution for $d\theta = \pm 0.1$ mrad. The contribution to the uncertainty in θ comes from: 1) uncertainty in production angle due to errors in position of the photon interaction, 2) uncertainty in the position of the H_2 target where the photon was created, and 3) uncertainty of the positron angle in the incident e^+ beam. The last is composed of the beam divergence plus the multiple scattering of the positron in the target material before annihilation. The mean square multiple scattering in hydrogen behaves as

$$\langle\theta^2\rangle = \left(\frac{15\ \text{MeV}}{E}\right)^2 \frac{t}{2} \,, \tag{II.6}$$

with t in radiation lengths. Since the divergence of the positron beam is estimated to be about 10^{-4} radians, implying a minimum energy spread of at

least ±1%, it is clear that each independent uncertainty should be kept down to this magnitude if possible. Thus t must be about 0.02 radiation lengths.

It has been shown[37] that the intensity of the photon beam in the region where the resolution is dominated by multiple scattering in the hydrogen target is proportional to the cube of the allowable resolution dK/K, according to the expression

$$I_\gamma = 0.024\, I_+ \frac{E}{K}\left[1 + \frac{K^2}{(E-K)^2}\right]\left(\frac{dK}{K}\right)^3 . \qquad (II.7)$$

For a net 1% resolution and symmetric conditions this says that $I_\gamma/I_+ = 9.6 \times 10^{-8}$ or about 1000 monochromatic photons for 10^{10} incident positrons.

In order to suppress photons below 20 MeV, which cause a significant scanning annoyance but yield no interesting hadronic events, one radiation length of lithium hydride was put in the beam. This beam hardener was placed in a magnetic field which swept the resulting electromagnetic particles out of the beam line to reduce the secondary bremsstrahlung emission reradiated in the beam direction. This removed nearly all the low energy photons while reducing the intensity of high energy photons by approximately a factor of three. In addition, the finite azimuthal acceptance of the bubble chamber window decreases the intensity by a similar factor. Taking all these into account, Fig. II.5 shows the predicted high energy photon intensity in the bubble chamber for a photon beam of 1% net energy resolution per 10^{10} incident positrons.

The flux used in the experiment was still lower than this since the pair production cross section of about 20 millibarns causes approximately one in fifteen photons to interact electromagnetically in one meter of liquid hydrogen. However, the number of pairs produced in each frame places an upper limit on the tolerable photon flux, since too many pairs can drastically reduce

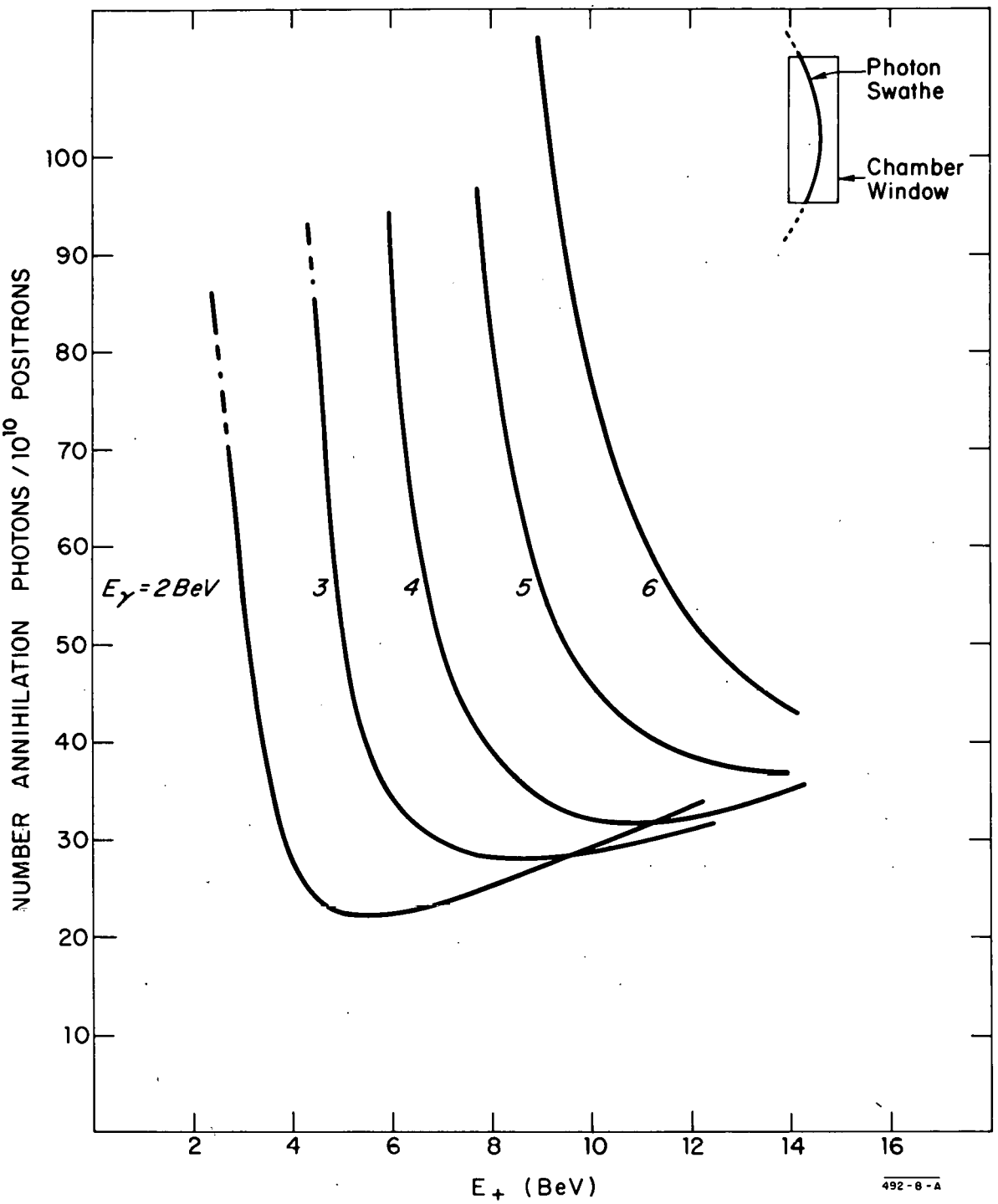

FIG. II. 5-- Predicted photon intensity in the bubble chamber per 10^{10} positrons of 1% energy resolution incident. Beam window acceptance and attenuation in 1.0 radiation length of hardener are included (see Ref. 37).

the efficiency of scanning for hadronic events. The operating flux was finally determined by the constant monitoring of test strips by physicists during the experimental bubble chamber run. The high positron currents at SLAC meant that it was possible to get an adequate flux of photons into the chamber, but this did require opening the collimators and using the event vertex position to define the annihilation energy as defined below.

The actual beam layout is shown in Fig. II. 6. A positron beam of energy E (see Table I for the parameters of the various exposures) with a momentum resolution of <0. 5% is focussed to a 3 mm spot with a beam divergence of <0. 1 milliradians at a liquid hydrogen target 15 cm long. The positron beam direction was kept to a tolerance of 0. 1 milliradians by checking the toroid position monitors P36 and 2P1 which were separated by 35 m. The positron beam was dumped into a shielding mass while the photon beam was collimated at an angle much larger than m/E which bounds the bremsstrahlung emission by C0, C1, and C2 (140 radiation lengths in total) before entering the bubble chamber. Charged particles were removed by three sweeping magnets, the first of which contained the lithium hydride beam hardener. The beam arriving at the bubble chamber was crescent shaped with approximate dimensions 6.4 cm. x 45 cm.

Three exposures were made at conditions as close as possible to the symmetric photon production geometry discussed above. For the 7. 5 GeV run the maximum positron energy of 12 GeV necessitated a slightly asymmetric setting. Table I shows the beam conditions and the size of each exposure. Figs. II. 7a, b, c show the energy spectrum of measured pairs in the three exposures. The high energy peaks are obviously present but they are significantly

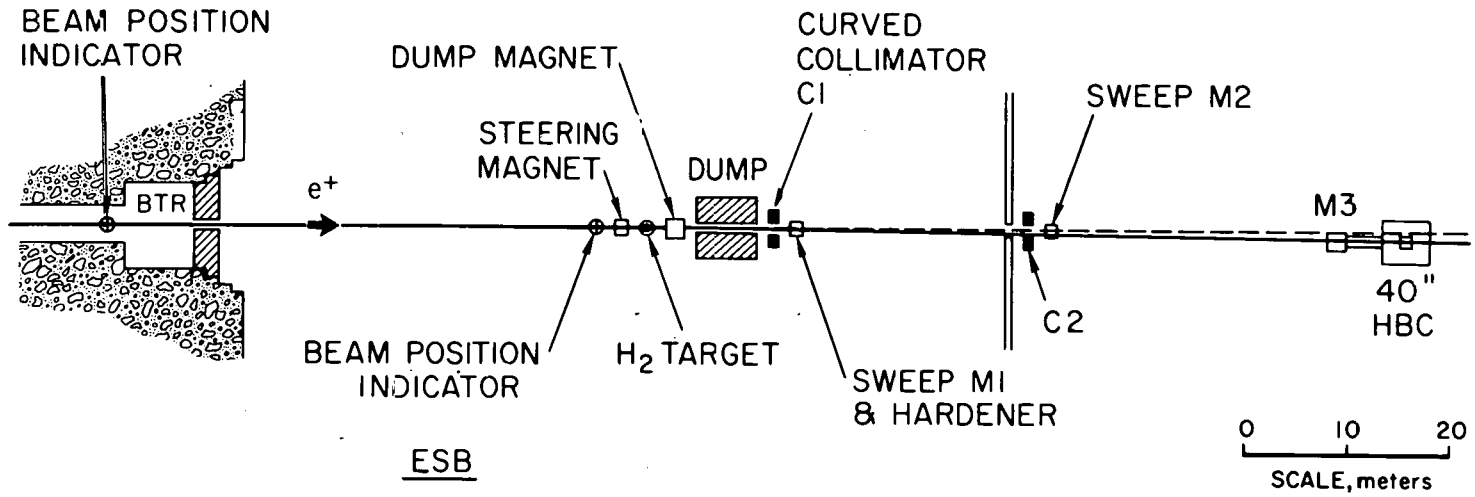

FIG. II. 6-- Layout of the positron annihilation beam in end station B.

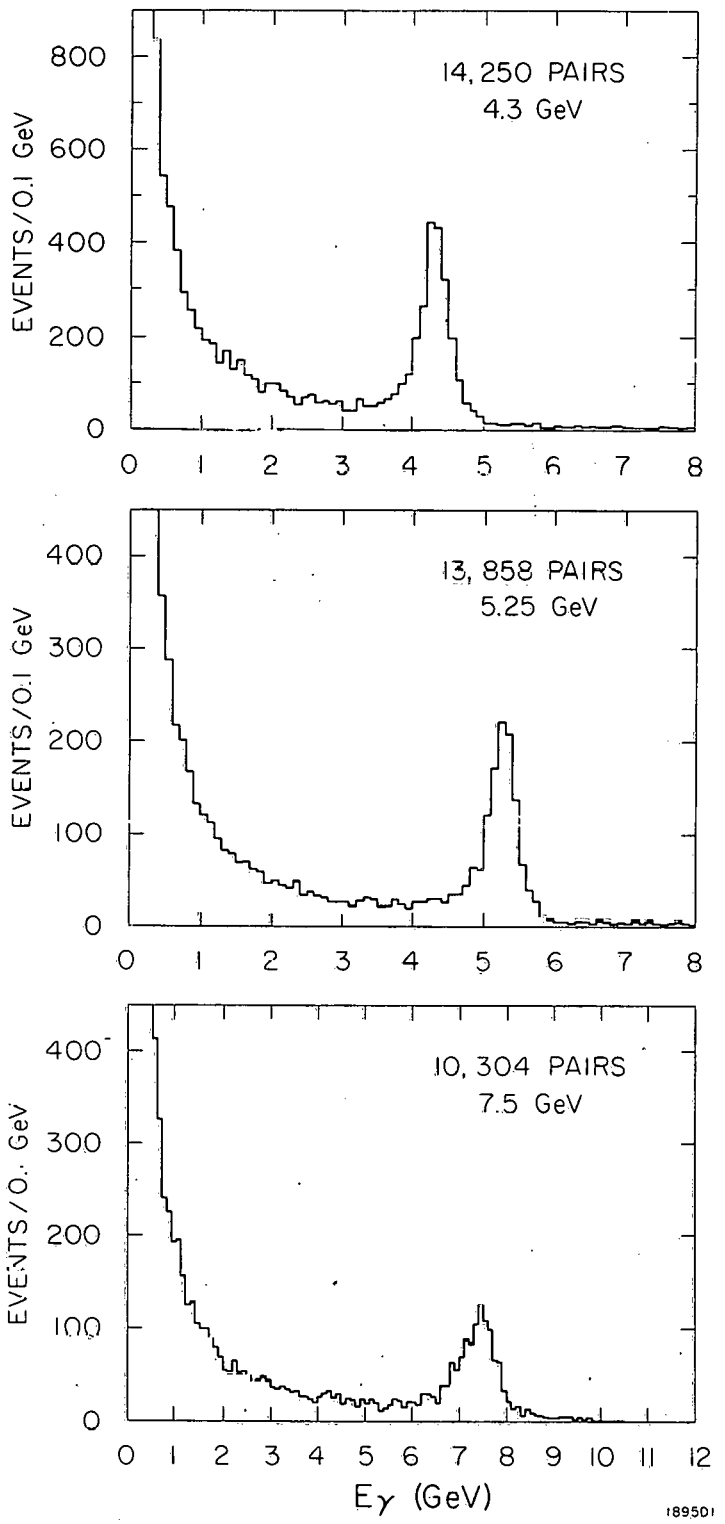

FIG. II.7-- Measured electron pair spectra at the three annihilation energies. The larger degree of spreading apparent in the annihilation peak of the 7.5 GeV data is because this exposure was made at less than optimal conditions (see Section II.2).

wider than the resolutions claimed in Table I. This is due to three factors. First, there is the ultimate resolution of the annihilation photon spectrum produced by the radiative tail of multi-photon annihilation processes, which transforms the two photon annihilation spike at K into the cusp-like annihilation peak shown in Fig. II. 8. When this and the resolution of the photon beam due to the energy and angular uncertainties discussed above are folded together, each individual event still can be assigned a monochromatic energy from the production angle determined by its vertex position in the chamber with a net resolution of about ±2%. Because of this, the collimators were opened to obtain an adequate flux of photons in the bubble chamber. This resulted in a superposition of monochromatic photons over an energy range of about 10%. These spectra therefore show a fairly large spread of photon energies, but with the energy of individual monochromatic photons known to about ±2% from the calculated angle. This is the second effect spreading the high energy peaks in Fig. II. 7; it can be eliminated by plotting the spectrum of E(fit) - E(calculated) as has been done for the data of Fig. II. 7c in Fig. II. 9. This removes the effect of the finite width of the collimator. A third discrepancy between these spectra and the true photon spectra is due to measuring tracks with undetected energy losses due to bremsstrahlung plus normal multiple scattering. This tends to spread out the ideal cusp in both directions, but primarily toward lower energies. This leads us to use the energy spectrum of 3-C events to obtain the E_γ spectrum, since hadronic tracks suffer almost no bremsstrahlung. This is illustrated for the 3-C events by the inset graphs in Fig. II. 10. The correction for these bremsstrahlung distortions of the measured pair spectrum is a very important feature for obtaining the cross sections in the experiment and will be discussed in detail in

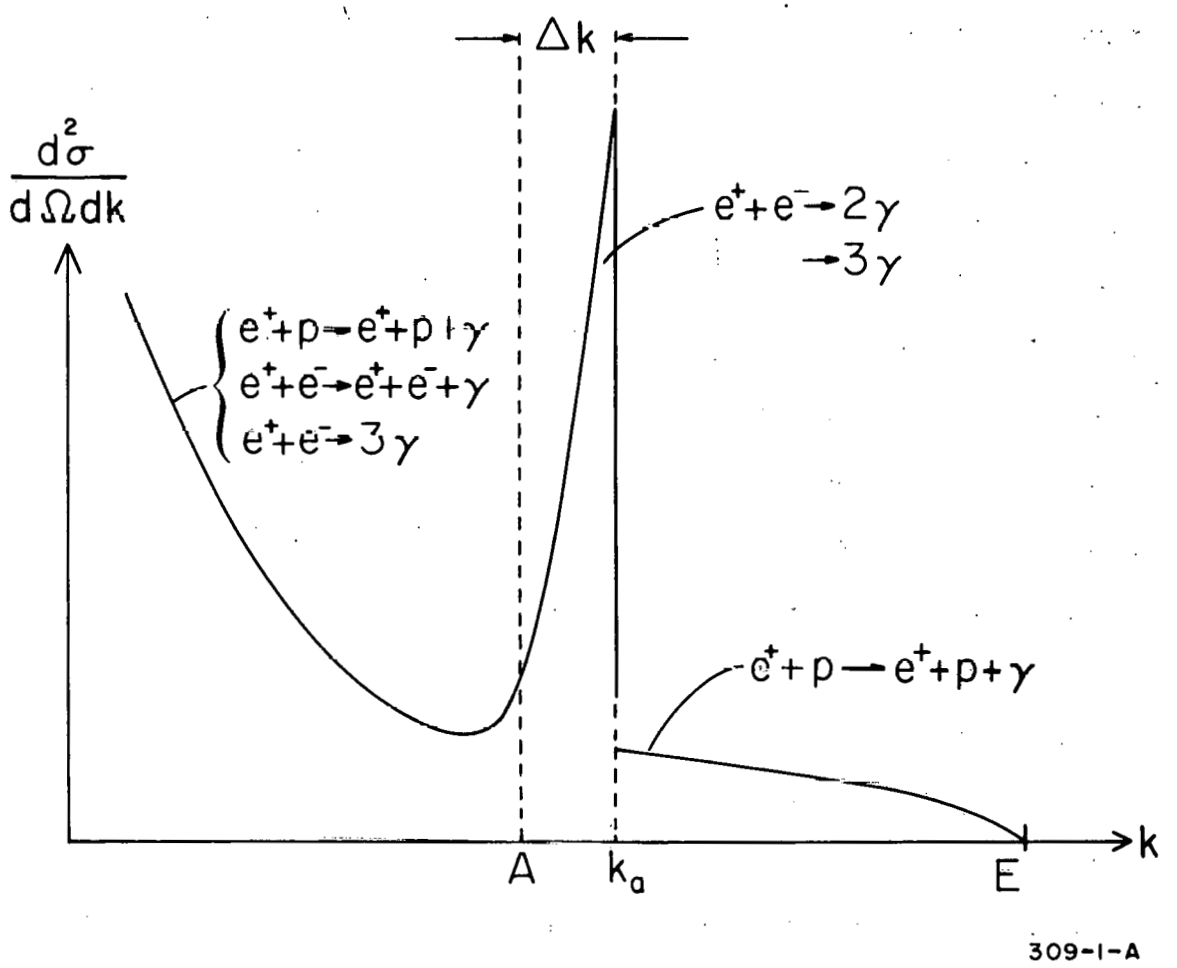

FIG. II. 8-- Theoretical spectrum for a positron-hydrogen atom collision at fixed angle. k is the photon energy, k_a is the 2 photon annihilation energy, and the upper limit to the bremmsstrahlung background is the incident positron energy, E.

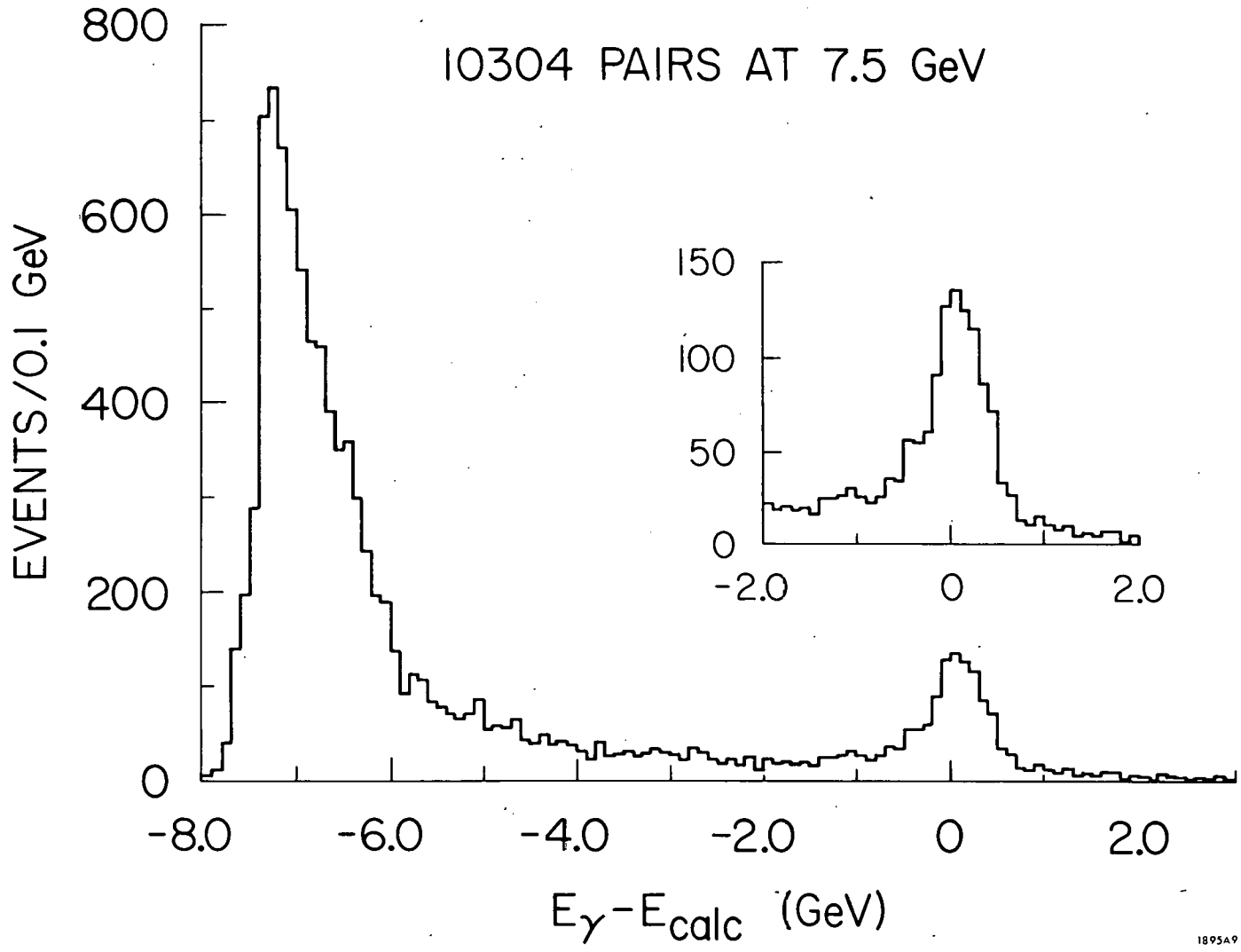

FIG. II.9-- E(gamma) - E(calculated) for 1-C pairs at 7.5 GeV. Inset graph shows an enlargement of the annihilation peak region. These measurements are not corrected for the distortions introduced by bremsstrahlung and multiple scattering.

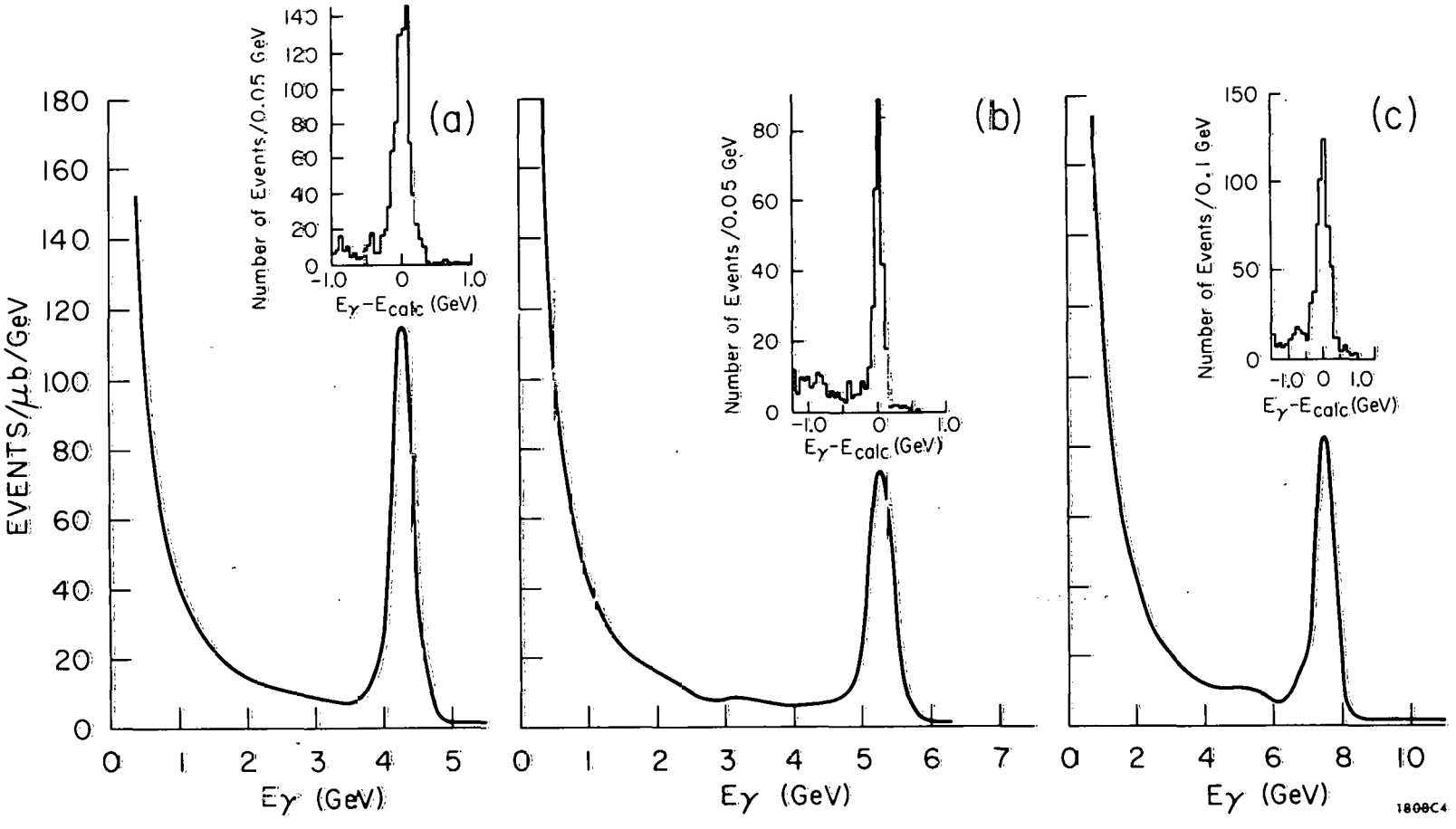

FIG. II.10--(a) Photon spectrum in the bubble chamber as deduced from measurements of the reaction $\gamma p \longrightarrow p\pi^+\pi^-$ and normalized to microbarn equivalents from e^+e^- pair production measurements for 4.3 GeV run. Positron energy 8.5 GeV, mean production angle 11.8 mr. The inset shows the distribution of energies E found for 3-C fits about that calculated from the event vertex positron in the chamber, illustrating the narrowing effect; (b) same for 5.25 GeV run; E_+=10 GeV, $\bar{\theta}$ =9.4 mr; (c) same for 7.5 GeV run; E_+=12 GeV, $\bar{\theta}$=7.15 mr.

Section III. 2. A summary of the photon spectra obtained at all three energies is given in Fig. II. 10 in addition to E(gamma) - E(calc) for 3-C events. Also note the resemblance of this spectrum to the theoretical spectrum of Fig. II. 8. The small tail of events above the monochromatic peak in Fig. II. 10 is due to e^+-p bremsstrahlung. The bremsstrahlung background was about 50% higher than expected, probably because of stray positron beam particles hitting the collimators and the large amount of inelastic e^+-p scattering producing indirect bremsstrahlung.[8]

II. 3 Determination of the Annihilation Beam Parameters

The pair measurements were not only used to determine the photon spectra, but also to determine the location of the liquid hydrogen target in the bubble chamber coordinate system (See Fig. II. 11). This, together with the coordinates of the event vertex, defined the direction of the incident beam. The x distance (along the photon beam line of the target from x=0 was surveyed very accurately to determine its value in space, and could be accurately maintained for different runs because of the fixed nature of the hydrogen target and the system of rails on which the bubble chamber housing and magnet were moved. However, for runs in between which the bubble chamber was moved for servicing, small shifts in the vertical or horizontal alignment of the fiducial marks could produce substantial changes in the values of the y and z coordinates of the target (nearly 60 meters away) as measured in the bubble chamber coordinate systems. Therefore the y and z values of the target coordinates were obtained separately for each run by projecting the beam direction obtained in 1-C pair fits back to the x distance of the target and averaging the resulting distributions.

A slightly more complicated calculation is necessary to be able to

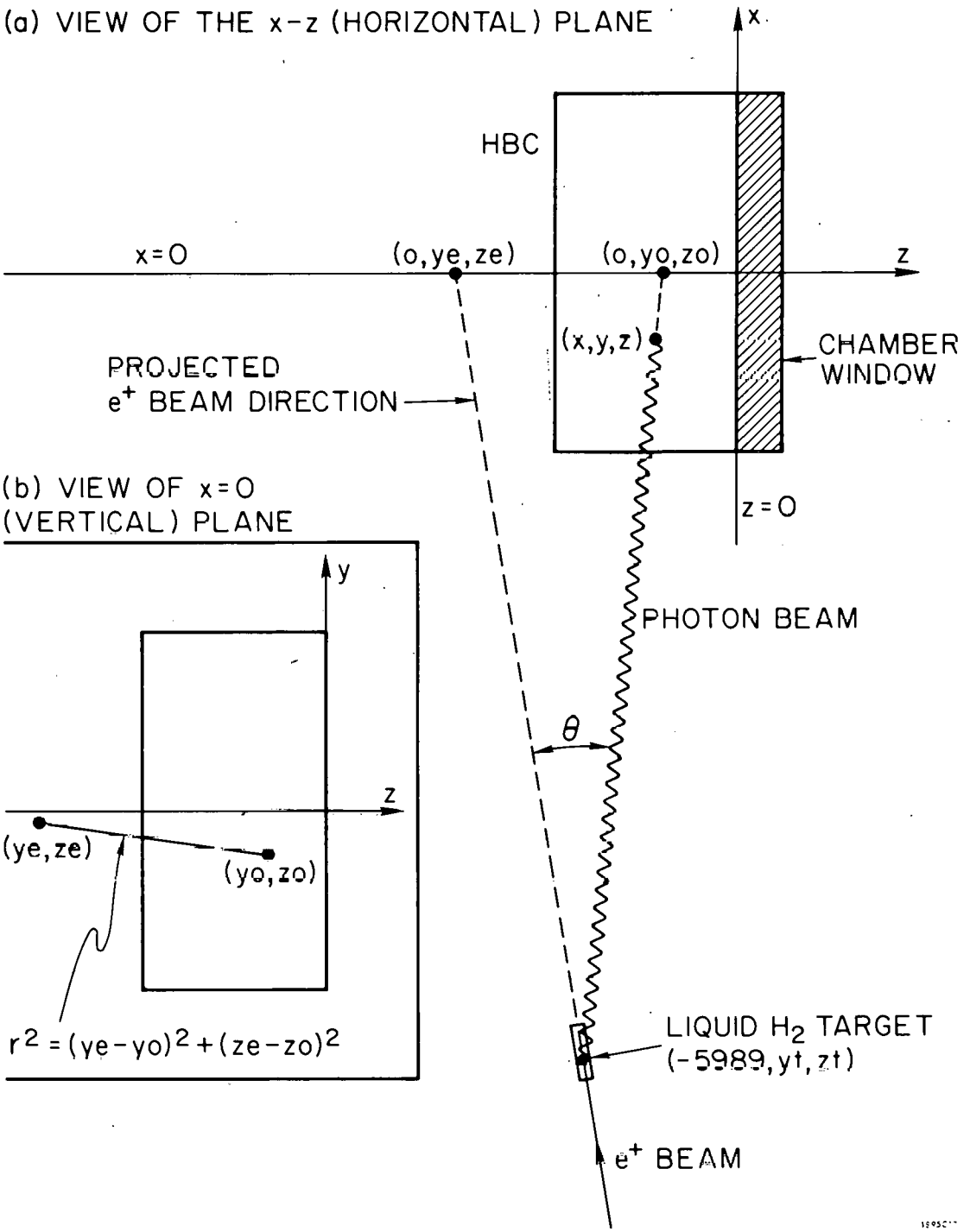

FIG. II.11-- Bubble chamber coordinate system viewed in two planes. (x,y,z) are the coordinates of event vertex, while (yo,zo) are the coordinates of the projected photon direction and (ye,ze) are the coordinates of the projected positron beam direction in the x=0 plane. The liquid hydrogen target was located at (-5989,yt,zt).

determine the angle of the incident photon with respect to the original positron beam from the vertex position. The technique is to ascertain which y and z coordinates, called ye and ze, the positron beam would have had in the plane x=0, i.e., at the bubble chamber, if it had not been deflected into the beam dump. Then the incident photon direction can also be projected from the event vertex into the x=0 plane to give yo and zo, and hence the distance between the e^+ direction and the photon direction can be calculated at a known distance from the target to give the photon production angle. The only subtle part of the process is to find the correct direction for the positron beam. This is done by adjusting the presumed coordinates ye and ze of the positron beam, so that the quantity E(fit)-E(calculated) plotted in Fig. II. 10 is centered at zero and is as narrow as possible. This is primarily a case of adjusting the value of ze, since the typical y separation |ye-yo| (See Fig. II. 11) does not exceed 20 cm, whereas the typical z separation |ze-zo| is 40-60 cm. However the proper value of ye will minimize the width of the annihiliation peak, since if ye is incorrectly set, events produced by annihilation photons of the same energy will be assigned different angles as a function of y according to the relation (see Fig. II. 12):

$$\theta(y) = r(y0)/xt \approx [r + (ye-yye)\ \ (y-(ye + yye)/2)/r]/xt\ . \qquad (II.8)$$

This means that if E(fit)-E(calculated) is plotted versus y on a two dimensional plot the center of the distributions of energy differences in different y intervals shifts as a function of y. Such di-plots have been made for each exposure in order to adjust ye toward its actual value. Similarly the values of ze have been adjusted to center E(fit)-E(calculated) at zero.

Due to the possibility of bremsstrahlung along the leptonic tracks,

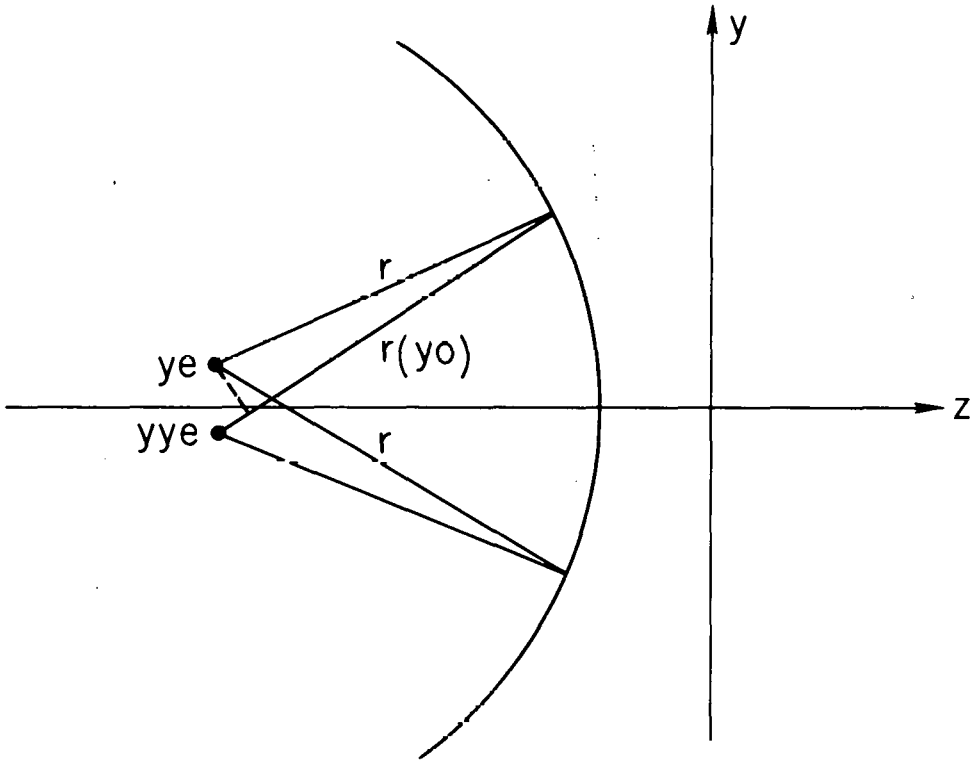

$$\theta = \frac{r(yo)}{xt} \quad \text{WHERE} \quad r(yo) \approx r + \frac{(ye - yye)\left(yo - \frac{ye + yye}{2}\right)}{r}$$

1895A15

FIG. II. 12-- Diagram illustrating how an incorrect value (yye) of the projected positron beam coordinate ye can influence the calculation of the photon beam angle (and hence the annihilation energy), making the calculated photon energy a function of the projected y vertex position instead of just the distance from the projected positron beam direction in the x=0 plane.

care was taken to select high energy pairs with long, well measured tracks for the determinations of target positions and beam projections. These results from pair measurements were then rechecked using events which gave 3-C fits so that the visible particles could be used to determine the beam direction and project back to the target. In this way consistent values have been determined for the target positions and positron beam parameters.

II.4 Scanning Procedures

The purpose of the scan was two-fold: to find all hadronic events and to determine the photon flux. A hadronic event is defined as a number of strongly interacting particles, such as pions, kaons, and protons, resulting from a photon-proton collision. Because the initial state contains one unit of positive charge, the number of charged tracks (also called "prongs" in this work) leaving the primary vertex is normally odd with one net positive unit of charge. Infrequent exceptions occur when the outgoing proton has a range of less than 1 mm (i.e., less than 80 MeV/c momentum), or when a negative prong charge-exchanges on a neighboring proton (e.g., $\pi^- p \longrightarrow \pi^o n$) before traveling a visible distance. Strange particles can often be identified by their characteristic decay. The electromagnetic background is identified by one of the following characteristics: 1) Compton electrons, resulting from elastic photon-electron scattering, are identified as single negative tracks, generally with low energy; 2) electron-positron pairs, produced off nuclei, have zero net visible charge and usually zero opening angle (the rare wide angle pairs can be confused with hadronic two prong events); and 3) triplets, where the electromagnetic pair is produced off an electron, have total visible charge of minus one.

The hadronic events were recorded only if their vertices occurred within a fiducial volume defined in view 2. This fiducial volume was limited so that a sufficient length (a minimum of 25 cm) could be measured to determine accurately the momentum of fast forward tracks. Also the scanners determined whether any of the strongly ionizing hadronic tracks stopped within the chamber without decay or annihilation, indicating a proton track. For such stopping protons, the end point of the track was measured to check on the momentum of the short stopping protons. If a secondary interaction occurred so close to the vertex on a track that an accurate momentum determination could not be made, the event was recorded as unmeasurable.

The determination of photon flux was made by counting the electron-positron pairs within the same fiducial volume defined for the events. Pairs were counted systematically throughout the experiment on enough frames so that the statistical accuracy in the flux determination would be greater than that of the events. In practice this was every 200 frames, although in some regions pairs were counted more frequently. Frames which had missing views, overlapping views, abnormally light tracks, poor contrast or blank areas were recorded as bad frames in a pre-scan and were subsequently deleted in scanning for events or in flux determination. In addition, certain regions where a combination of poor film quality and abnormally high flux made accurate scanning impossible were removed from the experiment.

Two independent scans were made for events and pair counting. The results of these were compared by computer and all discrepancies resolved in a third scan. This comparison scan was conducted only by scanners whose efficiency had been shown to be among the most reliable. The combined scan

efficiency can then be computed from

$$\epsilon = \frac{N(n_1 + n_2 - N)}{n_1 \cdot n_2} , \qquad \text{(II. 9)}$$

where n_1 and n_2 are the numbers of events found in the first and second scan respectively, and N is the net number found in the two scans. The number of events found, the scanning efficiency by event type, and the corrected numbers are presented for 3 prong and 5 prong events in the film scanned at SLAC in Table II. 1. The corrected numbers have been used to determine the cross sections. Furthermore, the efficiency of pair scanning has been examined and found to be essentially 100%. Therefore no specific correction has been applied to the flux, although the possibility of a small systematic error has been considered.

II. 5 Measuring and Kinematic Reconstruction

The events analyzed at SLAC were measured on conventional measuring machines put on-line to an ASI 6020 computer. Six to ten points were measured on each track in each of three views and four fiducial marks on the inside of the chamber window were measured in each view to serve as reference points for subsequent spatial reconstruction. The smallest unit on the film which could be digitized by the measuring stage was about 1 micron. However, the accuracy obtainable was much less due to a combination of factors, including finite bubble size, apparent bubble displacements due to turbulence or temperature gradients distorting optical path in the chamber, and some non-linearities in certain regions of the measuring stage. The latter problem was aggravated by using different measuring machines, only one of which had been used to measure the original fiducials for determining optical constants. The net result is that a more honest estimate of

TABLE II. 1

Number of events found in two independent scans of the film, scanning efficiencies by event type, and corrected number of events on the film for those portions of the 5.25 and 7.5 GeV data scanned at SLAC and used for cross section calculations. The second digit of the event type indicates the number of charged tracks seen (3 and 5 prong events), while the last digit gives ionization in formation: 0 for all tracks minimum ionizing, 1-9 otherwise. All efficiencies except for type 130 are consistently above 99%. The corrected numbers of this table have been compared to the numbers actually measured and on the SUMX tape to determine the scan-to-measure corrections of Table III. 5. Also note that those scanning efficiencies only correct for random scanning losses and not the systematic losses of low momentum transfer events with short range protons.

5.25 GeV Data

	Rolls 218-282				Rolls 732-830			
Event type	130	131-9	150	151-9	130	131-9	150	151-9
Events seen on film	346	1021	101	76	930	3352	222	270
Scanning Efficiency	0.972	0.991	0.988	0.996	0.975	0.993	0.994	0.998
Events on film	356	1030.3	102.2	76.3	953.8	3375.6	223.2	270.5

7.5 GeV Data

	Rolls 371-578				Rolls 1240-1531				Rolls 1685-1762			
Event type	130	131-9	150	151-9	130	131-9	150	151-9	130	131-9	150	151-9
Events seen on film	607	3799	205	399	1534	7168	500	636	300	1336	114	122
Scanning Efficiency	0.968	0.995	0.996	0.999	0.988	0.997	0.998	0.999	0.980	0.993	0.998	0.997
Events on film	627.1	3818	205.8	399.4	1553	7189.6	501	636.6	306.1	1345.4	114.2	122.4

the accuracy of measurements in the film plane would be in the range of 10-20 microns, corresponding to 150-300 microns in the chamber. Studies such as the one by Levy and Wolf[38] discussed below have typically obtained measuring accuracies in space in the range of 50 microns in the x-y plane and 250 microns in the z direction.

The geometrical reconstruction and hypothesis fittings were done by the programs TVPG and SQUAW.[39] The particle states fitted by SQUAW for three and five prong events are listed in Table II.2. Two types of fits were attempted for each possible final state, one with no constraint placed on the incident gamma energy and one with the incident energy calculated according to Eq. II.2. The former is designated by the mnemonic A for annihilation and the latter B for bremsstrahlung. Therefore, both 3 and 4 constraint fits are attempted to final states with no missing neutral particles and both 0 and 1 constraint fits are attempted to final states with one (or more) neutral particles. In addition, a missing mass calculation was made for each different assignment of masses to tracks, using the calculated annihilation photon energy and beam direction. The 3 and 0 constraint fits listed in Table II.2 exclude those that also made the corresponding 4 and 1 constraint fits. The relative magnitudes of these quantities give some feeling for the percentage of events produced by the monochromatic photons.

The selection of fits was done by rejecting constrained fits with kinematic chi-square greater than 30. The successful hypotheses for each measurement were then compared to the events on film by physicists to determine which fits were compatible with ionization. Also the physicists checked for incorrect event types, overlooked strange particle decays, and poor quality measurements. All events whose original event type was incorrect

TABLE II.2

Reaction hypotheses tested for 3 prong events.

Reaction	Source	Notation	No. fits at		
			4.3 GeV	5.25 GeV	7.5 GeV
(1) $\gamma p \rightarrow p\pi^+\pi^-$	Annih.	p+-A	823	519	810
	Brems.	p+-B	3917	4020	11868
(2) $\gamma p \rightarrow p\pi^+\pi^-\pi^o$	Annih.	p+-OA	832	943	1689
	Brems.	p+-OB	1571	2058	5608
(3) $\gamma p \rightarrow n\pi^+\pi^+\pi^-$	Annih.	n++-A	479	339	592
	Brems.	n++-B	1313	1384	3809
(4) $\gamma p \rightarrow p\pi^+\pi^-$ MM	Annih.	p+-MM	2403	3001	7397
(5) $\gamma p \rightarrow \pi^+\pi^+\pi^-$ MM	Annih.	++-MM	1792	1723	4401

or which were badly measured were sent for remeasurement. This check was continued by physicists at each stage of remeasurement until the number of events either poorly measured or unmeasurable was reduced to a very small percentage.

The calculated photon mass for all 3-C fits to events in the 5.25 and 7.5 GeV monochromatic peak region is given in Fig. II. 13. The width of the distribution is due to the errors of measurement, while the centering of the distribution depends on the knowledge of the central value for the magnetic field. In both aspects our measuring quality is comparable to previous photoproduction experiments,[40] especially considering the higher energies of these exposures.

The chi-square distribution is shown for these same 3-C events in Fig. II. 14. The usual phenomenon[41] encountered in bubble chamber experiments, namely that the chi-square distribution is too wide, is evident here. There are about 7-14% too many events in the high chi-square tail and the theoretical shape is off by a scale factor in the remaining events. This scale factor can be fit in either the chi-square distribution itself or the confidence level distribution. The chi-square distribution for 3 degrees of freedom can be generalized to

$$P(\chi^2) \propto \left(\frac{\chi^2}{\alpha^2}\right)^{1/2} \cdot \exp\left(\frac{-\chi^2}{2\alpha^2}\right) \qquad \text{(II. 10)}$$

in which case $\alpha = 1$ corresponds to the theoretical distribution. Bubble chamber experimenters generally find that the scale factor α^2 is in the range 1-2, which means that the errors in TVGP output are underestimated by a factor of α.

The exact causes of these deviations from the theoretical distribution

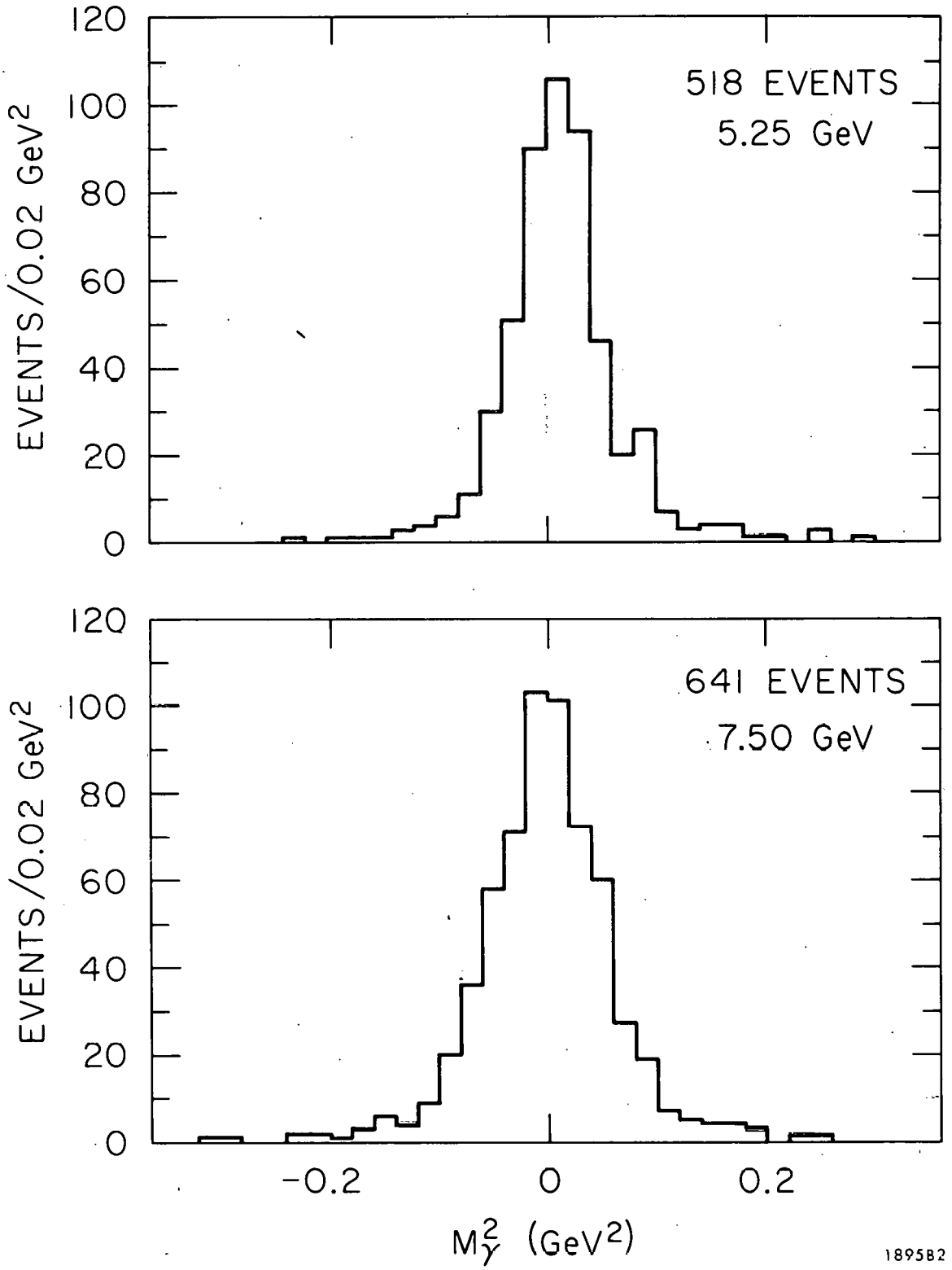

FIG. II.13-- Gamma mass squared calculated for 3-C events at the annihilation energies from the geometry values for the visible tracks.

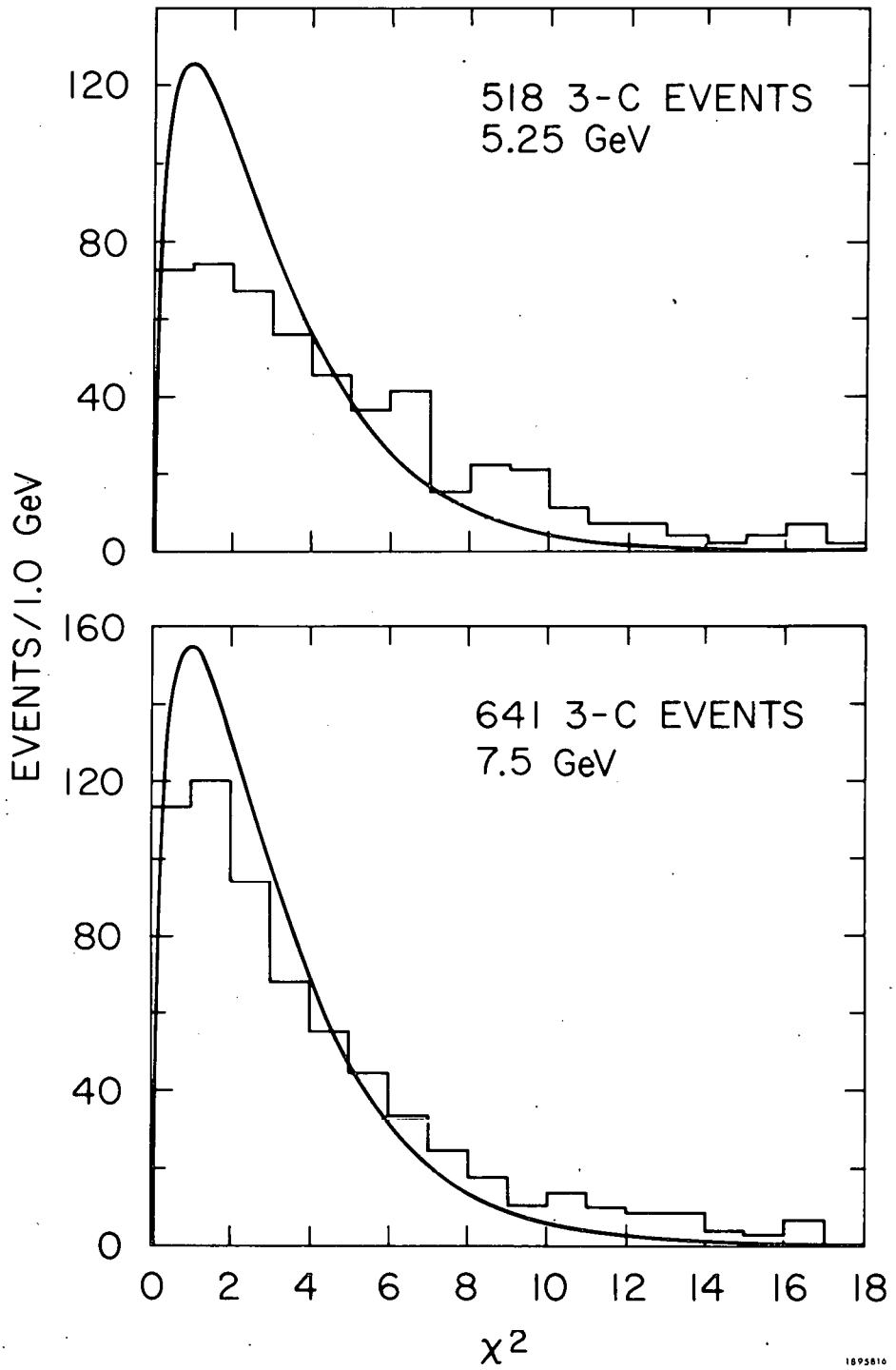

FIG. II.14-- Chi-squared distributions at 5.25 and 7.5 GeV for 3-C events.

are elusive. Poorly understood uncertainties in the optical constants, distortion corrections and liquid turbulence, as well as real non-Gaussian effects in Coulomb scattering corrections may well be responsible. We note that the chi-square distribution of the 5.25 GeV data deviates much more strongly from the expected shape than the 7.5 GeV data. Because of this deviation and the generally diffuse nature of some of the invariant mass plots studied in the 1-C channels (see Chapter V), the optical constants and distortion corrections were completely redone for the 5.25 GeV data to see if some error had been made originally. A complete reprocessing of these data revealed no significant improvement. One systematic difference which remains between the two exposures, however, is that the 5.25 GeV film was the first batch of photoproduction film measured at SLAC, and the overall quality of the measurements improved greatly by the time that the 7.5 GeV film was processed. Another possible systematic difference is the difference in chamber liquid turbulence between the two runs. The 5.25 GeV film was the initial output from a new bubble chamber and the particular stability characteristics and idiosyncracies of the chamber were perhaps not as well understood as they were after many months of operating experience. In spite of their differences, both sets of data have greatly improved chi-square distributions for scaling parameters α well within the usual range of 1-2. We find $\alpha^2 = 1.4$ for the 5.25 GeV data and $\alpha^2 = 1.2$ for the 7.5 GeV data. Since these numbers are reasonably close to 1 and since this scaling produces a quite reasonable chi-squared distribution, one concludes that the basic distortion of the errors is not due to a small set of poorly measured rolls, but rather the conspiracy of all the poorly understood features mentioned above.

As noted above, there are many sources for possible systematic distortions in a bubble chamber and its geometrical reconstruction process, among them turbulence in the chamber liquid, an incorrect or incomplete determination of optical parameters or distortion constants, and errors in the measurement and geometrical reconstruction process. It is possible to photograph charged particles in the chamber with the magnetic field off. Their paths may then be measured by conventional measuring machines and reconstructed by the usual reconstruction programs, and a search made for systematic deviations from the straight lines expected. Any such deviations would be the combined effect of one or more of the potential sources for distortion listed above.

A. Levy and G. Wolf[38] have performed such a study for the SLAC bubble chamber analysis system, consisting of the 40" chamber, the NRI measuring machines, and the TVGP geometrical reconstruction program with the TVGP optical constants determined by fiducial measurements.[42] They photographed fast muons in the chamber with the magnetic field off. Distortions due to multiple scattering were eliminated by adding together the effect of many tracks in the same region of the chamber. In this way no systematic distortions were found in either of the directions normal to the beam directions. The upper limits for such distortions were 50 microns in the visual plane (y direction) and 250 microns normal to the visual plane (z direction). From a fit to the curvature a maximum detectable momentum of P(MDM) = 1600 (+2400, -600) GeV/c was found by assuming a magnetic field of 26 kG and 100 cm. of track length.

In many instances we have checked our programs and studied the effect of our cuts on the data using the track and event simulation program

PHONY.[43] This program produces fake events, then digitizes a fixed number of points along each charged track with a Gaussian distributed error, and finally projects these into the three camera planes as if they were a real measurement. PHONY seemed to imitate nature quite well, except that the exact relationship between PHONY setting errors and TVGP setting errors was never fully understood. It was necessary to use a different setting error in PHONY than that used in TVGP in order to reproduce the physical FRMS distributions, chi-squared distributions, and missing mass squared properties. However, at least for the lower energies these errors should be Coulomb dominated and the Coulomb scattering routines worked very consistently. In all cases, the PHONY missing mass and invariant mass distributions obtained seem to be a very good representation of their counterparts obtained experimentally, so we are confident that they are a valid way of studying our losses due to cuts.

CHAPTER III

DETERMINATION OF THE CROSS SECTIONS

III. 1 General Method

Since the bubble chamber observes both hadronic events and electromagnetic pairs, the cross section for the hadronic events can be evaluated in terms of the pair-production cross section, which is known extremely accurately. By instructing the scanners to record events and pairs in exactly the same fiducial volume, it follows that the cross section for events in the energy interval (E1, E2) may be deduced from the formula

$$\sigma\,(\text{events},\ E_\gamma) = \frac{\text{Number of events } (E_\gamma, \Delta E_\gamma)}{\text{Number of pairs } (E_\gamma, \Delta E_\gamma)} \quad \sigma(\text{pair},\ E_\gamma).$$

The quantity $N(\text{pair})/\sigma(\text{pair})$ is called the microbarn equivalent for the exposure in that energy interval and once it has been determined it can be compared to any set of events to determine cross sections.

Several points should be noted regarding this equation. First, if the beam is not purely monochromatic (and our beam with its bremsstrahlung background was not), the pairs and the events considered should correspond to the same energy interval, (E1, E2), or at least be normalized to equal energy intervals. Second, if the energy interval is large, the cross section should be considered as calculated at the median energy rather than the mean, and energy dependent quantities should be averaged over the interval. Third, any effects such as the bremsstrahlung or multiple scattering of electrons and positrons, which distort the measurement of the true pair spectrum, must be corrected in order to obtain the photon spectrum. If all these effects are carefully considered, accurate microbarn equivalents can be determined.

The methods to be described here were applied to the best film of the 5.25 GeV data and that part of the 7.5 GeV film analyzed at SLAC. The main problem was to determine the cross section for $\gamma p \longrightarrow p\pi^+\pi^-$; after this was done, these cross sections were used to determine the flux for the entire exposure which could be extracted using the numbers of 3-C events found. Similar procedures were used by the Weizmann group for their 4.3 GeV data. The cross sections deduced agreed well within errors with the results of previous experiments. The 3-C cross sections calculated in this chapter are from the SLAC data only.

Several earlier experiments on photoproduction used calculations of the cross section for pair production on hydrogen that were reliable to only about 3-5%.[40] However, in 1970 T. M. Knasel[44] published numerical evaluations of theoretical formulae due to Jost, Luttinger, and Slotnick[45] which are accurate to better than 0.5% above 20 MeV. These results have been verified by recent experiments at DESY[46] to an accuracy of 1%. The cross sections of Knasel which have been used for this work are listed in Table III.1 and plotted in Fig. III.1.

III.2 Flux Determination for Cross Sections

The number of e^+e^- pairs was ascertained by counting approximately twice as many pairs as events, in order that the statistical accuracy of the flux not be a limiting factor in the cross section computations. This involved counting all pairs with energy greater than 100 MeV (by requiring the radii of curvature of the two tracks to sum to more than 14 cm). This was done on approximately eight frames per roll, yielding about 100 pairs versus an average of about 50 events. Two independent pair scans were performed, and all discrepancies were resolved in a third scan by one of the most

TABLE III. 1

Cross sections for pair production on hydrogen, according to Knasel (Ref. 44), as a function of photon energy, E_γ.

E_γ(GeV)	σ(mb)	E_γ(GeV)	σ(mb)
0.10	11.66	1.0	18.29
0.15	13.15	1.25	18.65
0.175	13.69	1.5	18.91
0.20	14.15	1.75	19.11
0.30	15.45	2.0	19.26
0.40	16.28	3.0	19.65
0.50	16.85	4.0	19.87
0.60	17.28	5.0	20.02
0.70	17.62	8.0	20.25
0.80	17.88	10.0	20.33
0.90	18.10		

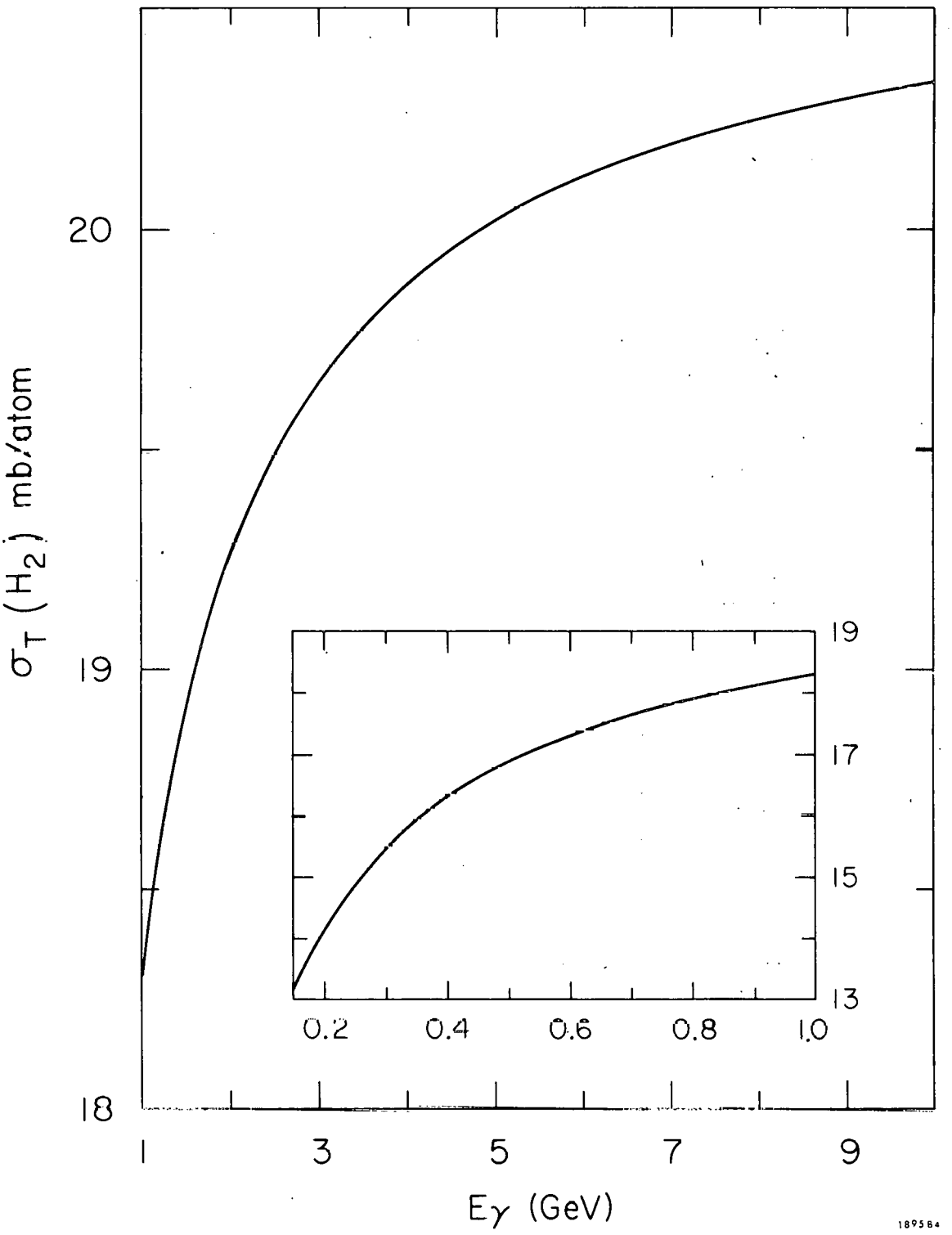

FIG. III. 1-- Pair production cross sections according to Knasel (Ref. 44).

reliable scanners. This procedure, when checked by physicists on a sample set of film, resulted in getting within 1% of perfect accuracy in the number of pairs present. Since errors could introduce false pairs as well as miss real ones, it was decided to neglect these corrections as being much less than the statistical errors on the events. The results of the pair scanning for the portions of the work done at SLAC are presented in Table III. 2. As can be seen from this table, pair scans were conducted uniformly throughout the experiment with the exception of one set of the 5.25 GeV data, which because of poor film quality and excess flux was not used for cross section measurements.

In order to know the energy distribution of photons in the annihiliation beam, about 50% of the scanned pairs were measured to determine the pair spectrum. These spectra have been presented in Fig. II. 7 for the three exposures. In each case the sample is large enough to reduce the statistical error well below that due to hadronic events. For a given exposure, to calculate the cross section for reactions in some energy interval the fraction of the total pairs produced by photons in that energy interval must be known. This is especially complicated near the annihilation peaks, since many electron pairs actually belonging to annihilation photons yield measured energies outside the peak region due to multiple scattering and bremsstrahlung on the leptonic tracks. These effects depopulate the annihilation peaks of the measured pair spectra and correspondingly enhance the regions just above and below the peaks (whereas bremsstrahlung can only reduce the measured pair energy, multiple scattering can cause errors in either direction). Because the strongly interacting particles are all much heavier than the electrons, the bremsstrahlung distortions are negligible on hadronic tracks, making the

TABLE III.2

Statistics Pair Scanning and Pair Frames for Rolls Scanned at SLAC

This is the raw data as tabulated by the program INDEX which was used to record and compare the results of scanning. Note that rolls 600-730 were the best 52 of 130 rolls which suffered from high flux and poor development. Since the criteria for acceptable film had been considerably relaxed, no pairs were scanned nor were they used for cross section determinations. The flux for rolls 1063-63 has been estimated using the pair flux from rolls 1083-1146.

5.25 GeV Data

Rolls	#Rolls	Total Frames	Bad Frames	Good Frames	Pair Frames	#Pairs	Σ Flux
218-282	49	59282	11015	48267	1654	18762	586086
600-730	52	70369	4801	65568	--	--	--
732-830	94	132226	13803	118423	1128	18842	1980603
Total	195	261877	29619	232258	2782	3704	2566689

7.5 GeV Data

Rolls	#Rolls	Total Frames	Bad Frames	Good Frames	Pair Frames	#Pairs	Σ Flux
381-578	117	169781	5664	164117	824	10394	2072337
1063-1066	4	5667	650	5017	--	--	(69200)
1083-1146	64	93833	17644	76189	670	9317	1054731
1240-1531	262	372291	5966	366325	1906	21001	4021964
1685-1762	51	74015	865	73150	378	4121	794868
Total	498	715587	30789	684798	3778	44833	8013100

3-C event spectrum shape much closer to that of the photons. Therefore an iterative procedure was used: the 3-C event spectrum weighted by the estimated 3-C cross section gave the shape of the assumed photon spectrum; then corrections obtained from PHONY generated pairs were applied for bremsstrahlung and multiple scattering to produce a distorted spectrum which should approximate the measured pair spectrum. In each energy bin the differences between the distorted spectrum and the assumed photon spectrum were obtained, and finally the corrections found were applied to the measured pair spectra of Fig. II. 7 to see how many pairs actually belong in each energy interval.

The program PHONY (see Section II. 5) was used to simulate the multiple scattering and bremsstrahlung on leptonic tracks to obtain the necessary corrections. Fig. III. 2 shows the outcomes of 3000 fake pairs generated at 5.25 and 7. 5 GeV after simulation by PHONY and reconstruction by the same programs (TVGP and SQUAW) used to process the actual measurements. About 2/3 of the pairs give energies less than their exact energy and 1/3 go above. If in fact these two curves are plotted on a scale versus E/E (production) they are seen to be very similar (Fig. III. 3). These data are very usefully presented in the cumulative form, namely the probability that a pair of energy Ep will yield a measured energy less than Em as a function of the ratio Em/Ep. These data are presented in Fig. III. 4. Because of this distortion, each energy bin of the measured pair spectrum contains: (a) those pairs due to photons with energies in that bin whose measured energy lies within the bin limits, and (b) those pairs from photons outside the bin limits but whose energies fall within because of measurement errors. This has been organized into an iterative matrix calculation which, given the

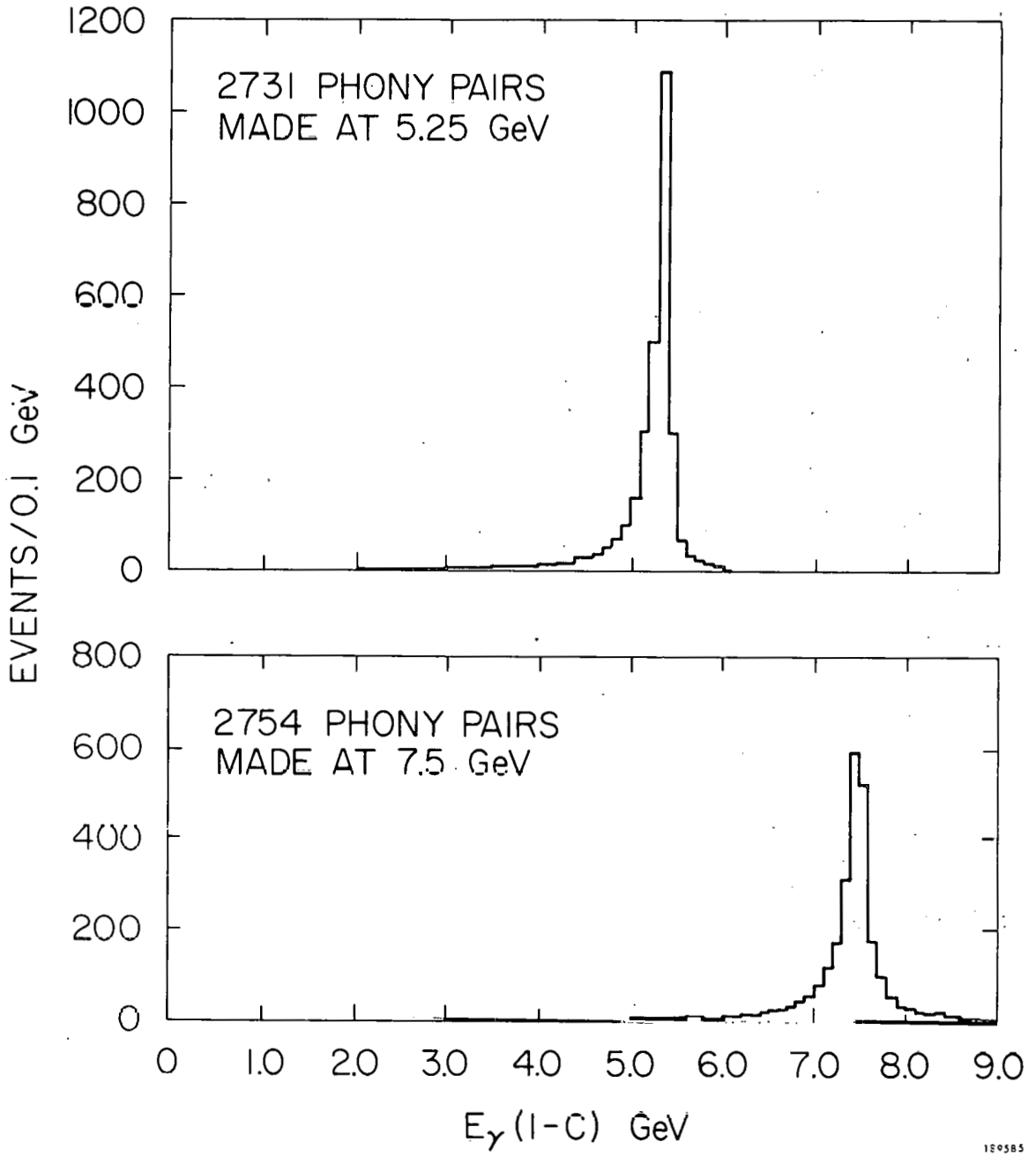

FIG. III.2-- Spectra of PHONY generated pairs at 5.25 and 7.5 GeV.

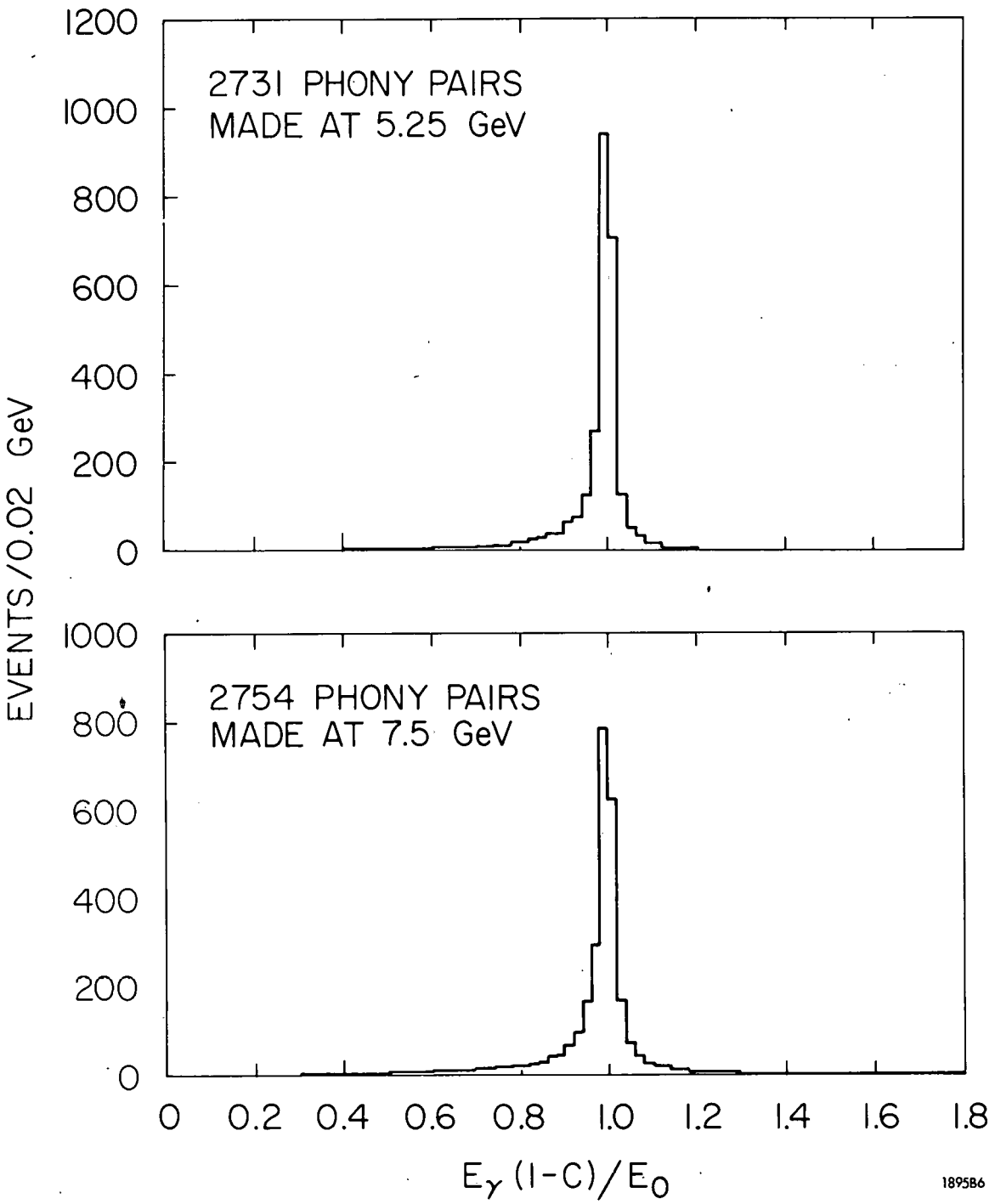

FIG. III. 3-- Spectra of PHONY generated pairs on a percentage scale.

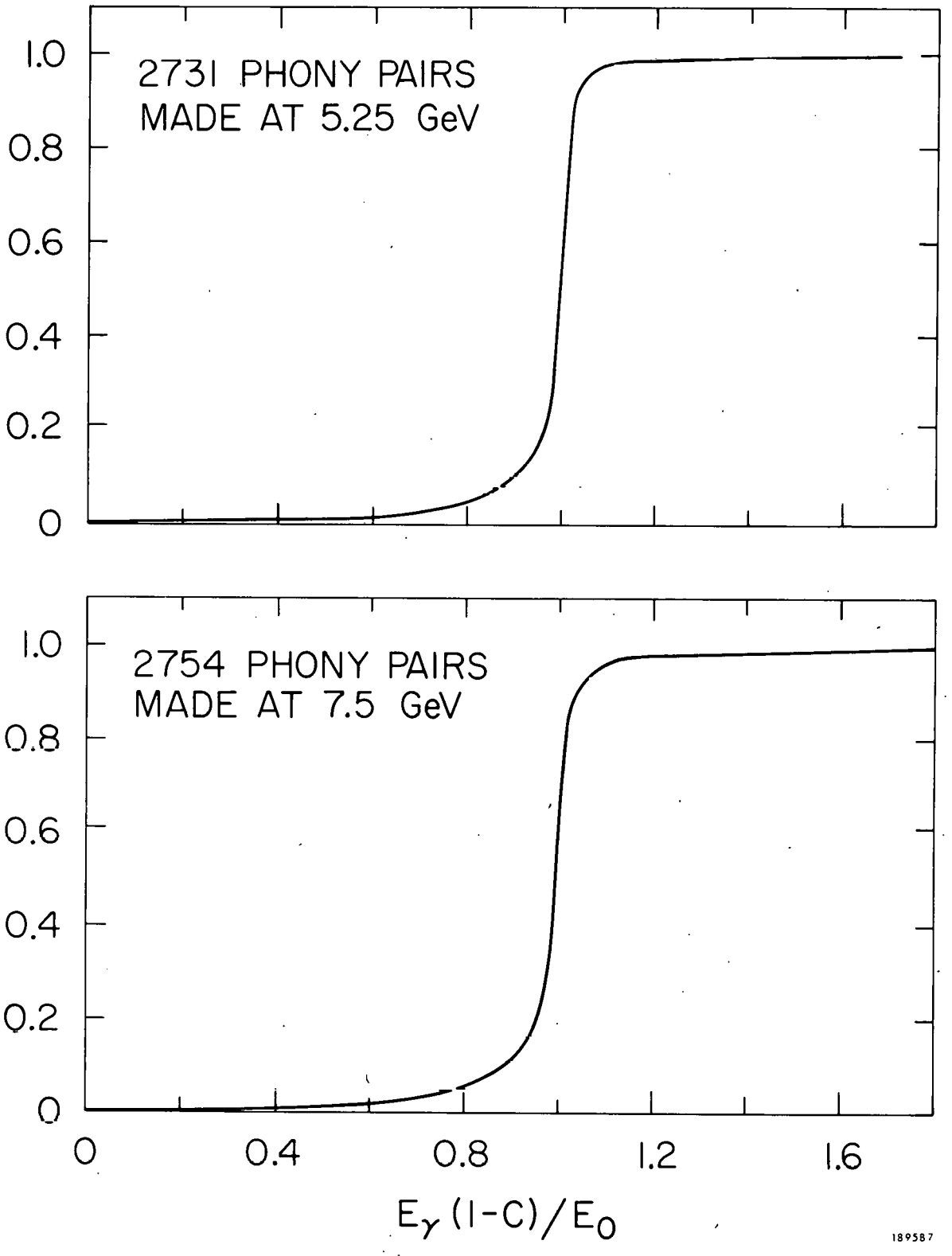

FIG. III.4-- Cumulative probability that a pair of energy E_0 will reconstruct to a pair with 1-C energy $< E_\gamma$, deduced from the PHONY spectra of the previous figure for $E_0 = 5.25$ and 7.5 GeV.

cumulative effect of bremsstrahlung on the pair measurements, transforms an original photon spectrum into the resulting spectrum of measured pair energies. From this and the original spectrum a correction factor as a function of energy and interval can be found. This correction applied to the various energy intervals of the measured pair spectra gives the actual number of pairs produced by photons in that energy interval, which is needed to compute the cross sections.

The correction factors were evaluated separately for the 5.25 and 7.5 GeV data, in each instance using both the PHONY results and the 3-C event spectrum for that energy. This was necessary since the appropriate energy intervals differed for the two exposures and the correction applied depended upon the interval under consideration. Table III.3 shows these results for the 5.25 GeV data and for those rolls of 7.5 GeV data that were analyzed by SLAC and used for cross section calculations. For maximum accuracy in the high energy cross sections, independent calculations were done over different energy ranges and found to be consistent well within the errors. These independent calculations will be presented below as illustrations of the typical flux error calculations (see Table III.4).

The important sources of error in the flux determination can be summarized by looking at the equation which defines the microbarn equivalent for a given energy interval:

$$\text{Microbarn equivalent (E1, E2)} = \frac{NP(E_1, E_2) \cdot BC \cdot NSCT \cdot NGF}{\sigma \cdot NPT \cdot NPF}$$

where NP(E1, E2) is the number of pairs in the interval (E1, E2) of the measured pair spectrum, NPT the total number of measured pairs, σ the mean pair cross section in microbarns for the interval, BC the correction for

TABLE III. 3a

5.25 GeV Flux Determination

E_γ (GeV)	# Pairs 732-830	Correction Factor	True Flux 218-282, 732-830	σ(Pair) in mb.	Events/μb 218-282, 732-830
.4-0.5	715	1.00	$1.30\ 10^5$	16.8	7.75
.5-0.6	575	1.01	1.06	17.1	6.18
.6-1.0	1434	1.01	2.64	17.8	14.82
1.0-1.2	467	1.02	0.87	18.5	4.69
1.2-1.5	515	1.02	0.96	18.8	5.09
1.5-2.0	614	1.01	1.13	19.1	5.91
2.0-2.5	438	1.00	0.80	19.35	4.12
2.5-3.0	320	0.95	0.55	19.6	2.81
3.0-3.5	281	0.94	0.48	19.75	2.44
3.5-4.0	237	0.88	0.38	19.85	1.91
4.0-4.5	285	0.68	0.35	19.9	1.77
4.5-6.0	2485	1.11	5.02	20.0	25.11
6.0-7.0	85	0.83	0.13	20.2	0.636
7.0-8.0	56	0.85	0.09	20.3	0.427
8.0-10.0	64	1.12	0.13	20.4	0.640
6.0-10.0	--	--	--	--	1.703

Total 1-C measured pairs on rolls 732-830, 14096.

Total flux, rolls 218-282, 732-830, 2.567×10^6.

TABLE III. 3b

7.5 GeV Flux Determination

E_γ(GeV)	Measured Pairs 381-578	1240-1530	1685-1762	Total	Correction Factor	σ(Pair) in mb.	Events/μb 381-578	1240-1530	1685-1762	Total
0.4-0.5	273	532	112	917	1.0	16.8	6.79	12.86	2.68	22.33
0.5-0.6	212	413	78	703	1.0	17.1	5.18	9.81	1.83	16.82
0.6-1.0	555	984	195	1734	1.01	17.8	13.17	22.68	4.45	40.30
1.0-1.2	167	351	59	577	1.01	18.5	3.81	7.78	1.30	12.89
1.2-1.5	163	358	65	586	1.01	18.8	3.66	7.81	1.40	12.87
1.5-2.0	218	444	78	740	1.01	19.1	4.82	9.54	1.66	16.02
2.0-2.5	164	230	55	499	1.01	19.35	3.58	5.94	1.14	10.66
2.5-3.0	108	231	50	389	1.01	19.6	2.33	4.83	1.04	8.20
3.0-3.5	88	176	39	303	0.99	19.75	1.84	3.58	0.79	6.21
3.5-4.0	65	131	27	223	0.97	19.85	1.33	2.60	0.53	4.28
4.0-4.5	63	148	26	237	0.95	19.9	1.26	2.87	0.50	4.63
4.5-5.0	47	107	25	179	0.93	20.0	0.92	2.03	0.47	3.57
5.0-5.5	61	88	20	169	0.91	20.05	1.16	1.63	0.37	3.16
5.5-6.0	40	104	20	164	0.83	20.1	0.69	1.75	0.33	2.77
6.0-6.5	52	126	35	213	0.55	20.15	0.59	1.40	0.39	2.38
6.5-7.0	100	215	40	355	0.68	20.2	1.41	2.94	0.54	4.89
7.0-8.0	386	844	133	1363	1.314	20.25	10.45	22.19	3.46	36.1
8.0-10.0	87	138	32	257	0.62	20.3	1.11	1.70	0.39	3.2
10.2-12.0	19	37	19	75	1.00	20.4	0.39	0.73	0.37	1.5
Total 1-C measured pairs	4957	9902	1976							
Total pair flux from scanners	2072337	4021964	794868							
Scanned/ measured	418.06	406.18	402.26							

TABLE III.4

5 GeV 3-C Cross Section Calculation (E_γ=4.0-6.0 GeV)

Experimental Data	Values	Errors
Pairs with E_γ=4.0-6.0 GeV (1-C Fits)	2770	1.9%
6% correction for bremsstrahlung losses	170	0.5%
Pairs created by photons with E_γ=4.0-6.0 GeV	2940	2.0%
Total number of 1-C fits to measured pairs	14096	1.0%
Fraction of all pairs with E_γ=4.0-6.0 GeV	$\frac{2940}{14096}$ =0.209	2.2%
Scanned pair flux (rolls 218-282)	0.586×10^6	
Scanned pair flux (rolls 732-830)	1.981×10^6	
Total flux in 218-282 + 732-830	$2.567\times10^6 = \Phi$	1.0%
Number of pairs with E_γ=4.0-6.0 GeV	$0.209\,\Phi = 5.35\times10^5$	2.5%
Pair Cross Section E_γ=4.0-6.0 GeV	$\bar{\sigma}$ =20 mb	1%
Microbarn Equivalent (218-282 + 732-830)	26.8 events/μb	2.7%
3-C events (E_γ=4.0-6.0 GeV)	418	4.9%
8% scan to measure correction (Table III.5)	34	1.4%
3-C events on film with E_γ=4.0-6.0 GeV	452	5.1%
$\sigma_{visible}$ (3-C, 3 prong, E_γ=4.0-6.0 GeV)= $\frac{452}{26.8}$ =	16.9 μb	5.7%
13% Forward loss correction	2.2 μb	1.5%
σ_{total} ($\gamma p \longrightarrow p\pi^+\pi^+$, E_γ=4.0-6.0 GeV)	19.1±1.15 μb	6.0%

bremsstrahlung distortions to the actual pair spectrum (as discussed above), NSCT the total number of pairs counted in scanning, NGF the total number of good frames in the experiment and NPF the number of frames on which pairs were counted. These last two numbers are exact and hence have no error, but all the other factors contribute either systematic or statistical errors to the microbarn equivalent. Both NPT and NSCT are large numbers and do not depend on the energy interval being considered; they are a source of statistical error and possibly a small systematic error for pair counting. The pair cross section is known to <0.5%. The number NP(E1,E2) is the smallest number and therefore contributes the largest statistical error; also it is by definition interval-dependent.

The most difficult error to estimate is that associated with the bremsstrahlung correction BC. The statistical part of this error is ultimately based on 3000 Monte Carlo pairs at one energy. For each bin of the spectrum, this error is taken to be the square root of the net number of pairs which must be added to or subtracted from the observed pairs NP(E1,E2) to obtain the corrected number. The percentage error is then $(|BC-1|/NP(E1,E2))^{1/2}$. For $|BC-1| < 1$, this is clearly smaller than $(NP(E1,E2))^{-1/2}$, the percentage error in NP. This shows that the error in the bremsstrahlung correction is least when the intervals are adjusted so that the corrections are small (e.g. intervals which are wide enough around the center of the annihilation peak to encompass most of those displaced from the peak by measuring errors). Since the error in the microbarn equivalent is dominated by the statistical error in the number of measured pairs in the interval under consideration, the statistical error in the correction is unimportant if $|BC-1| << 1$. However, it is incorporated in any case by multiplying the

statistical percentage error in the number of measured pairs in the interval under consideration by the factor $(1 + |1 - BC|)^{1/2}$.

This procedure can fruitfully be illustrated for the two intervals which were used to determine the cross sections in the region of the annihilation peaks: 4.0-6.0 GeV for the 5.25 data and 6.8-8.2 GeV for the 7.5 GeV data. A sample calculation is presented in Table III.4.

III.3 3-C Channel Cross Section

In order to obtain cross sections for various reaction channels, corrections must be introduced for events that were missed in the double scan, events that were not measurable owing to scatters or short fast tracks, and a small fraction of events which failed all measurements or were lost and not considered worth retrieving. The number of events found in the scans and the number successfully measured are shown in Table III.5. Combining these into one number, the "scan to measure" correction, the results obtained are also listed in Table III.5 for three and five-prong events at both SLAC energies. This boost was applied equally to all of the various physical hypotheses of Table II.2, assuming that losses other than short protons are independent of the event configuration. The numbers which make up this correction are large enough that the statistical error in the correction is quite small.

In addition to this "scan to measure" correction, for 3-C events there is a significant loss in the $p\pi^+\pi^-$ channel of events with small t(p,p) and therefore very short protons, which can make the event look like an e^+e^- pair to the scanner. This forward loss correction is also quite significant

TABLE III. 5

Scan-to-measure corrections for events used to determine 3-C cross sections.

These corrections do not include energy-dependent effects like the forward losses which must be corrected separately, but do account for all random losses in the processes of scanning and bookkeeping, including losses for unmeasurable events and events never remeasured. The events "on SUMX" have been counted directly from our SUMX tapes, while the events "on film" are corrected for scanning losses as in Table II. 1.

5.25 GeV Data

	Three Prong Events		Five Prong Events	
Rolls	On Film	On SUMX	On Film	On SUMX
218-282	1386.3	1289	178.5	147
732-830	4329.4	3993	493.7	426
Sum of above	5715.7	5282	672.2	573
Correction Factor	1.082		1.173	

7.5 GeV Data

	Three Prong Events		Five Prong Events	
Rolls	On Film	On SUMX	On Film	On SUMX
381-578	4445.1	4212	605.2	545
1240-1531	8742.6	8143	1137.6	1019
1685-1762	1651.5	1571	236.6	217
Sum of above	14839.2	13926	1979.4	1781
Correction Factor	1.065		1.111	

for the channel $p\omega$ but less so for other events in the channel $p\pi^+\pi^-\pi^o$ where the proton seems to be less peripherally produced and of course in the channel $\pi^+\pi^+\pi^-n$ which generally has 3 clearly visible tracks. Therefore the forward loss corrections must be studied for each reaction separately. The study of forward losses in the channel $p\rho^o$ will be discussed in section IV. 1.

Since, as discussed above, the 3-C event energy spectra are not distorted like the measured pair spectra, the number of 3-C events in any energy interval can be obtained directly from a histogram. These numbers are then boosted by the scan to measure correction to give the number of visible events on film and divided by the microbarn equivalent to give the visible 3-C cross section. Forward loss corrections using a linear exponential extrapolation are then applied where applicable to give the results shown in Table III. 6. It is clear from the number of events in each energy interval that the uncertainty in the cross sections is dominated by the statistics of the hadronic events. Table III. 7 shows the combined results from the 5.25 and 7.5 GeV exposures and Fig. III. 5 shows these SLAC results compared with other experimental determinations of the cross section for three-constraint, three-prong events.[9,10,16]

In order to have maximum accuracy in the cross sections for events produced by high energy annihilation photons, independent calculations were made in wider intervals than those in Table III. 7 so that they are less sensitive to the calculated correction function (i.e., the intervals being larger "catch" more of the pairs whose energies are mismeasured). This check

TABLE III. 6a

5.25 GeV 3-C, 3 Prong Cross Section Calculation

E_γ (GeV)	Events/μb	3-C Events on SUMX	3-C Events on film	σ_ν(3-C)	Forward loss correction	σ(3-C)
0.4-0.5	7.75	69	74.5	9.6 μb		9.6 μb
0.5-0.6	6.18	249	268.9	43.5 μb		43.5 μb
0.6-1.0	14.82	1024	1105.9	74.6 μb		74.6 μb
1.0-1.2	4.69	299	322.9	68.9 μb		68.9 μb
1.2-1.5	5.09	259	279.7	55.0 μb		55.0 μb
1.5-2.0	5.91	261	281.9	47.7 μb		47.7 μb
2.0-2.5	4.12	139	150.1	36.4 μb		36.4 μb
2.5-3.0	2.81	80	86.4	30.7 μb		30.7 μb
3.0-3.5	2.44	62	67.0	27.5 μb	6%	29.2 μb
3.5-4.0	1.91	49	52.9	27.6 μb	8%	29.8 μb
4.0-4.5	1.77	36	38.9	22.0 μb	10%	24.2 μb
4.5-6.0	25.11	382	4.2.6	16.4 μb	13%	18.5 μb
6.0-10.0	1.70	19	20.5	12.0 μb	14%	13.7 μb

TABLE III. 6b

7.5 GeV 3-C, 3 Prong Cross Section Calculation

E_γ (GeV)	Events/μb	3-C Events on SUMX	3-C Events on film	σ_ν (3-C)	Forward Loss correction	σ (3-C)
0.4-0.5	22.33	181	192.8	8.6 μb		8.6 μb
0.5-0.6	16.82	777	827.5	49.2 μb		49.2 μb
0.6-1.0	40.30	2962	3154.5	78.3 μb		78.3 μb
1.0-1.2	12.89	855	910.6	40.6 μb		70.6 μb
1.2-1.5	12.87	744	792.4	61.6 μb		61.6 μb
1.5-2.0	16.02	754	803.0	50.2 μb		50.2 μb
2.0-2.5	10.66	367	390.9	36.7 μb		36.7 μb
2.5-3.0	8.20	244	259.9	31.7 μb		31.7 μb
3.0-3.5	6.21	142	151.2	24.3 μb	6.5%	25.9 μb
3.5-4.0	4.28	88	93.7	21.8 μb	7%	23.4 μb
4.0-4.5	4.63	83	88.4	19.1 μb	8%	20.6 μb
4.5-5.0	3.57	67	71.4	20.0 μb	9%	21.8 μb
5.0-5.5	3.16	56	59.6	18.9 μb	10%	20.8 μb
5.5-6.0	2.77	45	47.9	17.3 μb	11%	19.2 μb
6.0-6.5	2.38	29	30.9	12.3 μb	12%	13.8 μb
6.5-7.0	4.89	64	68.2	13.9 μb	13%	15.7 μb
7.0-8.0	36.10	469	499.5	13.8 μb	13.4%	15.7 μb
8.0-10.0	3.20	38	40.5	12.7 μb	14%	14.4 μb

TABLE III. 7

Cross sections for the 3C fit reactions $\gamma p \rightarrow p\pi^+\pi^-$ and $\gamma p \rightarrow p\pi^+\pi^+\pi^-\pi^-$ found in this experiment, averaged in the energy intervals shown.

E_γ(GeV)	$\sigma(\gamma p \rightarrow p\pi^+\pi^-)(\mu b)$	E_γ(GeV)	$\sigma(\gamma p \rightarrow p\pi^+\pi^+\pi^-\pi^-)(\mu b)$
0.4-0.5	9.0 ± 1.0		
0.5-0.6	47.6 ± 3.0		
0.6-1.0	77.2 ± 3.5		
1.0-1.2	70.2 ± 4.0		
1.2-1.5	60.0 ± 3.5	1.2-1.5	0.035 ± 0.04
1.5-2.0	49.5 ± 3.0	1.5-2.0	0.8 ± 0.2
2.0-2.5	36.5 ± 2.0	2.0-2.5	1.9 ± 0.3
2.5-3.0	31.2 ± 2.2	2.5-3.0	3.1 ± 0.5
3.0-3.5	26.8 ± 2.0	3.0-4.0	5.5 ± 0.7
3.5-4.0	25.3 ± 2.5	4.0-5.0	4.4 ± 0.7
4.0-4.5	20.7 ± 2.0	5.0-5.5	4.9 ± 0.7
4.5-6.0	19.0 ± 1.0	5.5-6.0	6.0 ± 1.0
6.0-7.0	15.8 ± 2.0	6.0-7.0	4.6 ± 0.9
7.0-8.0	16.0 ± 1.2	7.0-8.0	4.6 ± 0.4
8.0-10.0	14.5 ± 2.5	8.0-10.0	5.4 ± 1.0

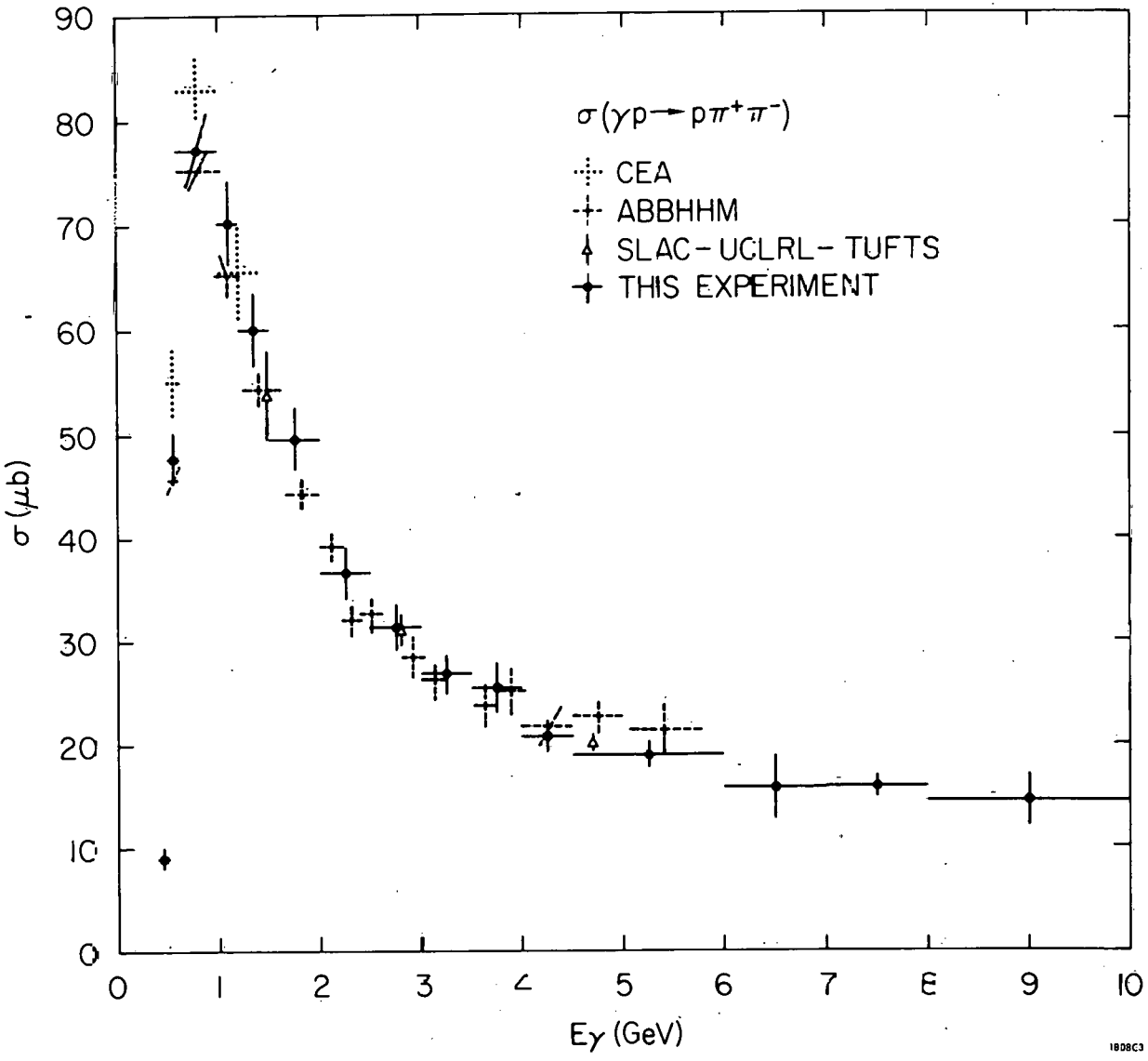

FIG. III. 5-- Cross sections for the reaction $\gamma p \longrightarrow p\pi^+\pi^-$, as a function of energy E_γ, found in this experiment, and compared with other determinations. Points marked CEA are from Ref. 9; ABBHHM, Ref. 10; SLAC-UCLRL-TUFTS, Ref. 16.

produced quite consistent results:

$$\sigma(3\text{-C, 3-prong}) = 19.1 \pm 1.2 \text{ microbarns} \qquad E_\gamma = 4.0 - 6.0 \text{ GeV}$$

$$\sigma(3\text{-C, 3-prong}) = 15.7 \pm 1.0 \text{ microbarns} \qquad E_\gamma = 6.8 - 8.2 \text{ GeV}$$

which are the values used to normalize other cross sections in the rest of this study.

III.4 Calculation of Cross Sections for 1-C Channels

Constrained fits can be made to events of the reactions

$$\gamma p \longrightarrow p\pi^+\pi^-\pi^o \qquad \text{(III. 1)}$$

$$\gamma p \longrightarrow \pi^+\pi^+\pi^- n \qquad \text{(III. 2)}$$

if these are produced by annihilation photons, since the location of the vertex determines the incident photon energy to about ±1.5%. This precision was tested by comparing the confidence levels of 3-C and 4-C fits for the same events, which gave a fairly uniform scatter plot. Three of the four energy-momentum constraints are used to determine the three neutral particle variables. The remaining constraint can act as a filter to isolate these events from diverse backgrounds. This is the standard procedure for bubble chamber experiments with charged beams, where the incident energy is well known.

In our case there are a number of backgrounds which are troublesome. As in the charged case, there are the multi-neutral reactions

$$\gamma p \longrightarrow p\pi^+\pi^-\pi^o\pi^o \cdots \qquad \text{(III. 3)}$$

$$\gamma p \longrightarrow \pi^+\pi^+\pi^-\pi^o n \cdots \qquad \text{(III. 4)}$$

where the dots represent possible additional neutral particles. Furthermore, reactions (1) to (4) produced by bremsstrahlung photons may fit the 1-C hypotheses under consideration due to poor measurement or unfavorable kinematics. Therefore let the notation (1A) denote reaction (1) from annihilation photons (i.e., photons within the energy cuts used in the previous section), (1B) denote the same reaction from bremsstrahlung photons, and likewise for reactions (2) - (4). Then, for example, the events of reaction (1A) can be contaminated by the events from (1B) and events of (3A) and (3B). Moreover, if one of the pions in reaction (2) or (4) is fast enough so that it can not be distinguished from a proton, it may simulate reaction (1). Similarly, reaction (2) may be contaminated by fits from events of (1) or (3) with fast protons.

The independent determination of the gamma energy allows the missing mass of the fit to be used as a criterion to isolate relatively pure samples of reactions (1A) and (2A) from the various backgrounds discussed above. Therefore a missing mass approach has been adopted to determine the true number of events to be assigned to these reactions. Assume a very narrow annihilation peak and perfect measurements. The calculated missing mass, m, is defined by

$$m^2 = (K_A + m_p - E_{vis})^2 - (\vec{k}_A - \vec{p}_{vis})^2 \qquad \text{(III, 5)}$$

where k_A and $\vec{k}_A$ are the energy and momentum of an annihilation photon, m_p the proton mass, and E_{vis} and $\vec{p}_{vis}$ are the sum of energy and momentum for the charged, or visible, tracks. Then if the hypothesis is correct, m^2, will peak sharply at the mass squared of the missing particle, while for events from the background m^2 will be more uniformly distributed. In practice, the

distinction is less precise, since the annihilation peak is not a perfect spike and the spread in measurements is non-negligible (see Fig. II. 7).

For a number of reasons it is more useful to study distributions of missing mass squared rather than missing mass.[47] Missing mass squared is more closely related to the measured quantities, which are presumed to have an approximately normal distribution. Also experimental histograms of missing mass squared do appear to be normally distributed. Furthermore, in studying reactions involving a single pi-zero, the missing mass distribution is distorted because the pion mass is so close to zero. The neutron mass is far enough from zero not to suffer this distortion, but has been treated in exactly the same way as the pi-zero for consistency.

To understand the effectiveness of missing mass squared as a discriminatory tool in the case that the particle can not be identified by ionization, it is necessary to examine photoproduction kinematics. In the laboratory system, let k_t be the true energy of the photon producing an event, k the value assumed in the missing mass fit and let E_o, P_o, m_o and theta be the energy, momentum, mass and production angle with respect to the beam of the actual neutral system of particles. In the bubble chamber the momentum of an ambiguous track is measured essentially correctly, but the energy assigned depends on the assumed mass. Let f=(assumed energy minus true energy) $\simeq (m_f^2 - m_t^2)/2p$, where m_f is the mass assigned to an ambiguous track of momentum p (p greater than 1.4 GeV, which is the approximate cut-off for good ionization discrimination) while m_t is the true mass. The calculated neutral mass m_c is then given by

$$m_c^2 = m_0^2 + 2(k_A - k_t)(E_0 - P_0 \cos\theta) - 2f(E_0 - k_A + k_t - f/2) \qquad \text{(III. 6)}$$

If the ambiguous track is assigned its correct mass, then f = 0 and it is clear that for true photon energy k_t less than the expected annihilation energy, m_c^2 is always greater than the true missing mass. However, a fast forward neutral system will make the missing mass insensitive to assumed photon energy. For example, low energy $p\pi^+\pi^-$ events with 3-C fits will very often also give a fit to reaction (1A) by adding a fast forward neutral pion whose energy is just the difference between calculated annihilation energy and the correct photon energy. The only multineutral events which will be assigned an annihilation single neutral hypothesis when f = 0 are from the electron-proton bremsstrahlung photons with true energy greater than k_A, and as may be seen from the spectra of Fig. II.10, will make negligible contamination. For ionization-ambiguous events, it turns out that those with a true neutron in the final state (f > 0) generally gave low enough E_0 and high enough m_0 to make the overlap with the $p\pi^+\pi^-\pi^o$ hypothesis small. Those with a true fast proton from reaction (1) or (3), annihilation or bremsstrahlung, however, represent a considerable overlap with reaction (2A) and must be treated more carefully.

The separation of a pure sample of four-body, single neutral, high energy events for the three annihilation experiments was done using missing mass squared plots. After applying the ionization criteria, the missing mass squared of the neutral system was calculated from the annihilation photon energy and the measured momenta of the visible particles by Eq. (III.5). Fig. III.6 shows the missing mass squared distributions for fits of the type $\gamma p \longrightarrow p\pi^+\pi^-MM$ and $\gamma p \longrightarrow \pi^+\pi^+\pi^-MM$. These distributions clearly peak at $MM^2 = m_\pi^2$ and $MM^2 = m_n^2$. In order to obtain the cross sections for reactions (1) and (2) in the monochromatic peak regions, it is necessary to

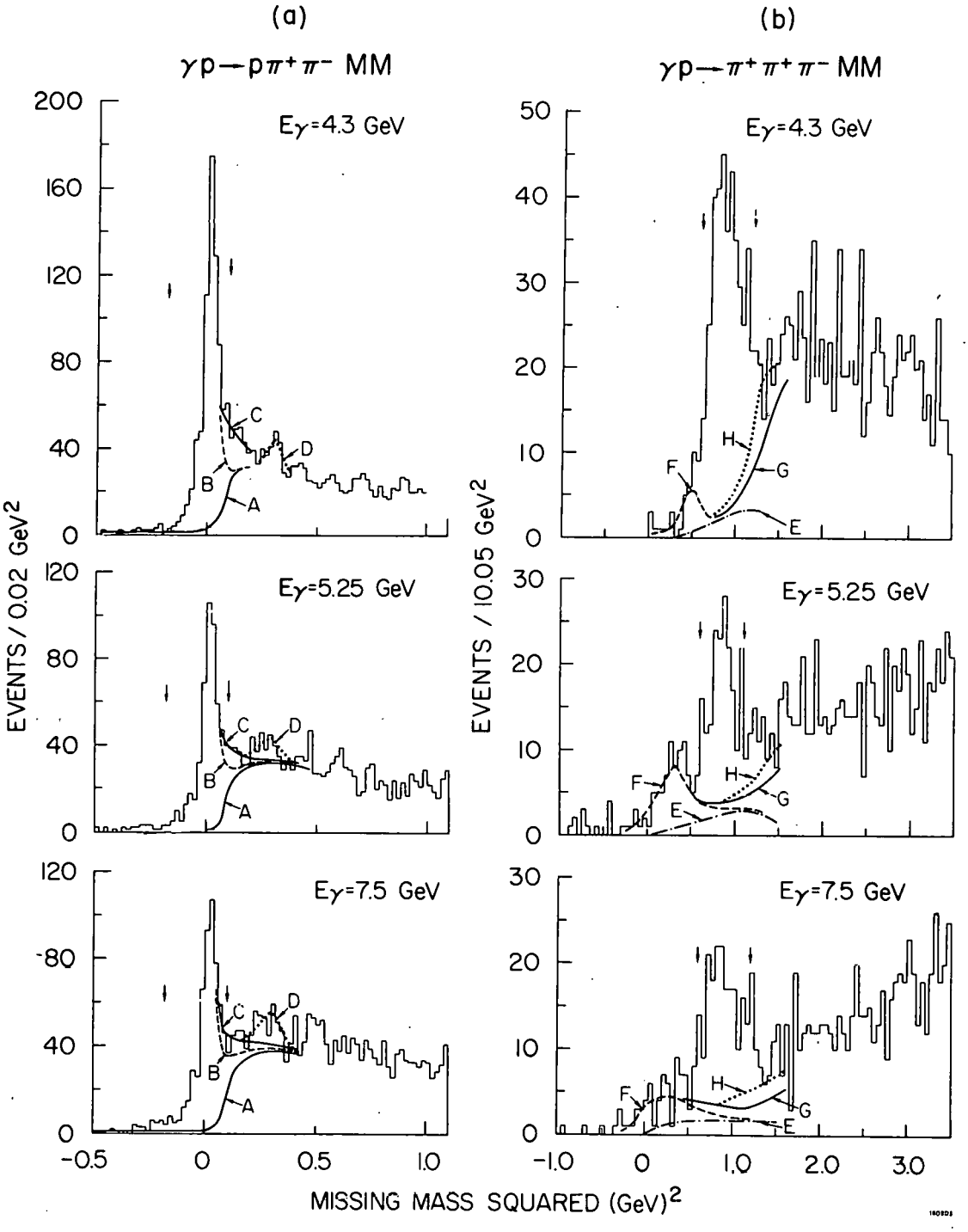

FIG. III. 6-- (a) Missing mass squared, as defined in text, for all events consistent by ionization with the reaction $\gamma p \longrightarrow p\pi^+\pi^-$ plus neutrals at three photon energy settings; (b) same for events consistent by ionization with $\gamma p \longrightarrow \pi^+\pi^+\pi^-$ plus neutrals. Events with fast proton appear in both (a) and (b). The dotted lines show the various background estimates as explained in the text and Ref. 7.

determine the shape and magnitude of the background contributions to the missing mass plots. Exactly parallel methods were used for the pi-zero and the neutron channels. These methods will be described here in general terms before discussing the specific channels.

The backgrounds in the region of the single neutral peaks fall into three main classes: (i) contamination of the high energy regions by events from nearby bremsstrahlung photons, (ii) contamination by misidentified events, i.e., fits to $\pi^+\pi^+\pi^-n$ by ambiguous events of $p\pi^+\pi^-\pi^o$ and vice versa, and (iii) contamination of the four-body reactions by multineutral events. All of these backgrounds were largely excluded by making cuts in the missing mass spectra. The cuts used were $(-0.18,\ 0.10)\,GeV^2$ for the pi-zero and $(0.6,\ 1.2)\,GeV^2$ for the neutron distributions. The choice of these cuts is discussed below. Then PHONY calculations were used to estimate the number of true events which had been excluded by this cut. Events of reactions (1) and (2) were generated by PHONY with the energy distributions of the 3-C event spectra at 4.3, 5.25, and 7.5 GeV. Each of these events was labelled according to the energy used in generation as being a mono or brems event, depending on whether the generation energy was within or outside the standard energy cuts used for these exposures. The discrimination of the missing mass cuts could then be separately determined for brems and mono events at each energy.

The PHONY missing mass squared distributions appear in Fig. III.7. Those events produced with energies inside the mono energy bands show very well defined signals at the appropriate missing mass values for their neutral particle, whereas the brems events give very distorted missing mass spectra, most of which fall outside the cuts used. It is evident that most of the mono

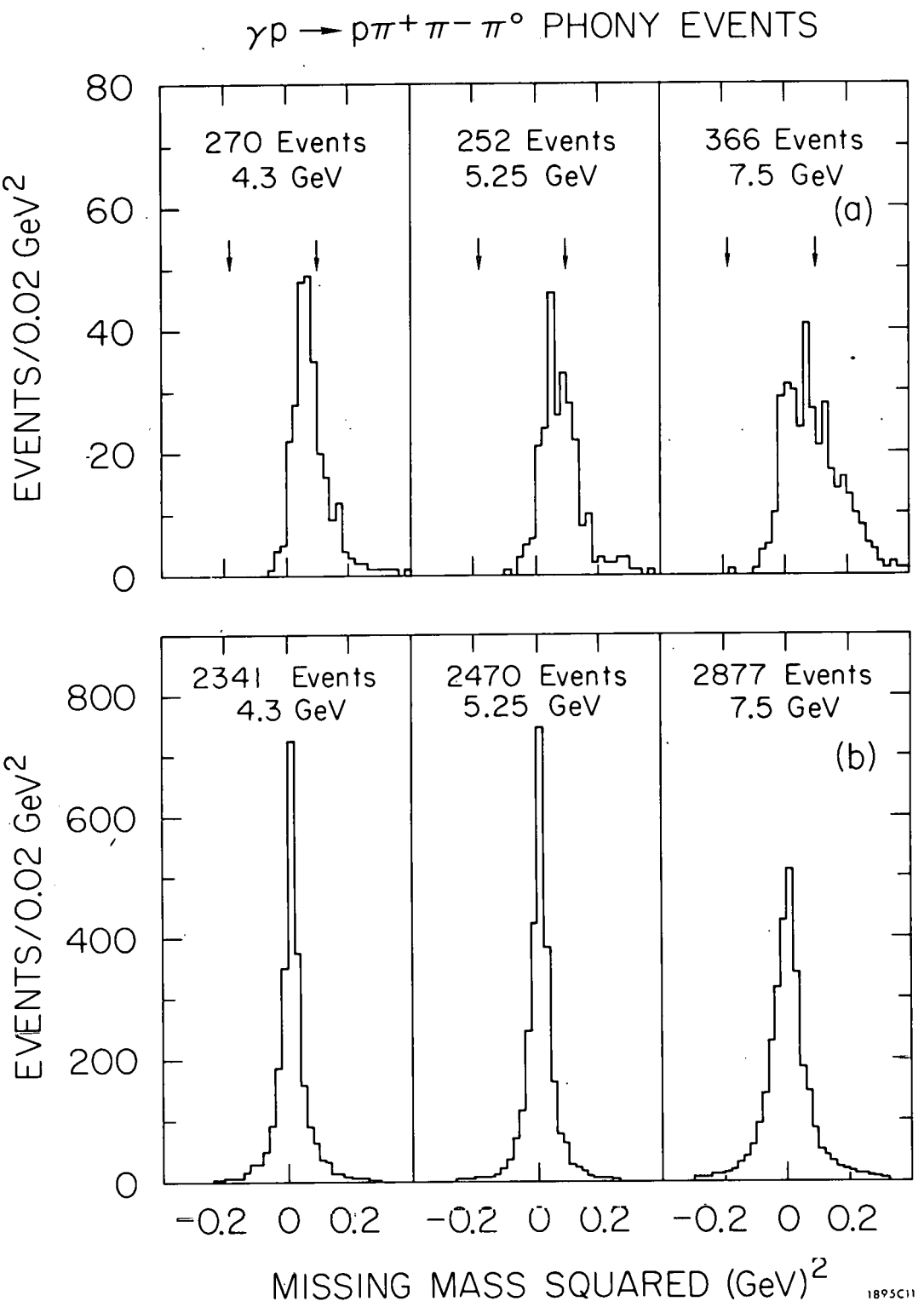

FIG. III.7-- Missing mass squared distributions for PHONY events of the reaction $\gamma p \longrightarrow p\pi^+\pi^-\pi^0$. (a) 1-C fits to events with photon energies in the bremsstrahlung region for each exposure. (b) 1-C fits to events with photon energies in the annihilation regions. The arrows in (a) show the cut used to define good π^0 events.

events will survive the cuts whereas most of the brems events will fail. The exact numbers can be used to generate ratios f(mono) and f(brems) giving the percentages of mono and brems events which survive the missing mass cuts. These can then be combined for any exposure to relate the true number of mono events to events actually observed inside the cuts. The necessary equations are

$$N^{obs}(\text{mono}) = f(\text{mono})\ N^{true}(\text{mono})$$

$$N^{obs}(\text{brems in mono}) = f(\text{brems in mono})\ N^{true}(\text{brems})$$

$$N^{true}(\text{brems}) = X\ N^{true}(\text{mono})$$

where X is a factor which combines the relative number of photons attributed to the brems and mono regions with the different average cross sections in these regions for the reaction being studied. Although X is not perfectly known, it can be adequately approximated using first guesses (uncorrected) at the cross sections and by defining the brems region to extend far enough in energy below the mono region that it is very unlikely for any fits to come from farther away into the mono region. Then these equations can be combined to give a relation between those events--brems or mono--actually observed within the missing mass cut and the number of true mono events--in and out of the cut, namely

$$N^{obs} = N^{obs}(\text{mono}) + N^{obs}(\text{brems})$$

$$= (f(\text{mono}) + X\ f(\text{brems}))\ N^{true}(\text{mono})$$

This equation has been used to correct those events within the missing mass cuts above backgrounds (ii) and (iii) into the total number of events produced

in the mono region. This number divided by the proper microbarn equivalent from section III. 2 then yields the cross section.

Backgrounds of type (ii) in the neutron channel from events with fast protons were estimated by recalculating the missing mass squared of constrained fits to $p\pi^+\pi^-\pi^o$ with good MM^2 and ambiguous protons as $\pi^+\pi^+\pi^-MM$. Such events which also gave a neutron fit explained the characteristic bump in the neutron missing mass plots just below the true neutron mass. Very little of the opposite contamination (i.e., true neutron events simulating $p\pi^+\pi^-\pi^o$) was found.

The type (iii) backgrounds were estimated by using the actual five-body events, namely 3-C fits to $p\pi^+\pi^+\pi^-\pi^-$. It was assumed that a $\pi^+\pi^-$ pair is kinematically equivalent to a $\pi^o\pi^o$ pair insofar as the missing mass squared distribution is concerned (ρ^o production is not important when averaged over all $\pi^+\pi^-$ combinations) and that $p\pi^-$ combination likewise approximates $n\pi^o$. Then by omitting in turn each $\pi^+\pi^-$ pair from $p\pi^+\pi^+\pi^-\pi^-$, it is possible to simulate four different events of the type $p\pi^+\pi^-MM$. Similarly $p\pi^+\pi^+\pi^-\pi^-$ can be recalculated as two different events $\pi^+\pi^+\pi^-MM$ by pairing each negative pion with the proton for omission. In this way simulations to the backgrounds from $p\pi^+\pi^-\pi^o\pi^o$ and $\pi^+\pi^+\pi^-\pi^o n$ have been obtained.

Backgrounds to the Pi-Zero Channel

Fig. III. 6a shows the missing mass squared calculated for all three prong events failing a 3-C fit but making a 0-C fit to reaction (1) consistent with ionization. The data for each energy appear to peak very close to $m^2_{\pi^o}$, to fall off smoothly to the left, and to encounter rapidly increasing background as one moves beyond the two pion threshold. Superimposing on the data the

symmetric curve centered at $m^2_{\pi^o}$, as predicted by a PHONY calculation (see Fig. III. 7), determines the point above which the background events contribute more than the good single pion events. The limits of -0.18 and +0.10 GeV^2 are suggested; -0.18 GeV^2 is about the point where the flat background under the π^o peak intersects the Gaussian tail of the true π^o events and 0.10 GeV^2 is the point where the height of all 0-constraint events is about twice the height of the tail of the symmetric π^o peak, using the left side of the peak to define the shape. Whatever cut is chosen, the PHONY simulations discussed above determine a correction for the exclusion of true events.

The primary sources of background to this reaction are from reactions (1B) and (3 A & B). The effect of (1B) has been simulated by PHONY while the effects of (3 A & B) have been simulated from actual five prong events by studying the missing mass distributions which result when two charged pions are neglected. The missing mass squared distributions resulting from 3-constraint five-prong events calculated using only the proton and two pions are shown in Fig. III. 8. This is the shape that has been used for the multi-neutral backgrounds to reactions (1A). Using the requirements of symmetry of the true signal, the dominance of the background shape by multi-pion events, and the presence of some η^o production near a missing mass squared of 0.3 GeV^2, estimated from the number of $\eta^o \longrightarrow \pi^+\pi^-\pi^o$ seen in five-prong events, one can draw the backgrounds as shown in Fig. III. 6a. For the purpose of background subtraction we have not included the events of reaction (1B) since they can be corrected separately via PHONY in a more quantitative way. Their distribution as given by PHONY, however, has been important for establishing the level of multi pi-zero background. In this way the background within the limits of the cut described above is seen to be about 35 events at both energies.

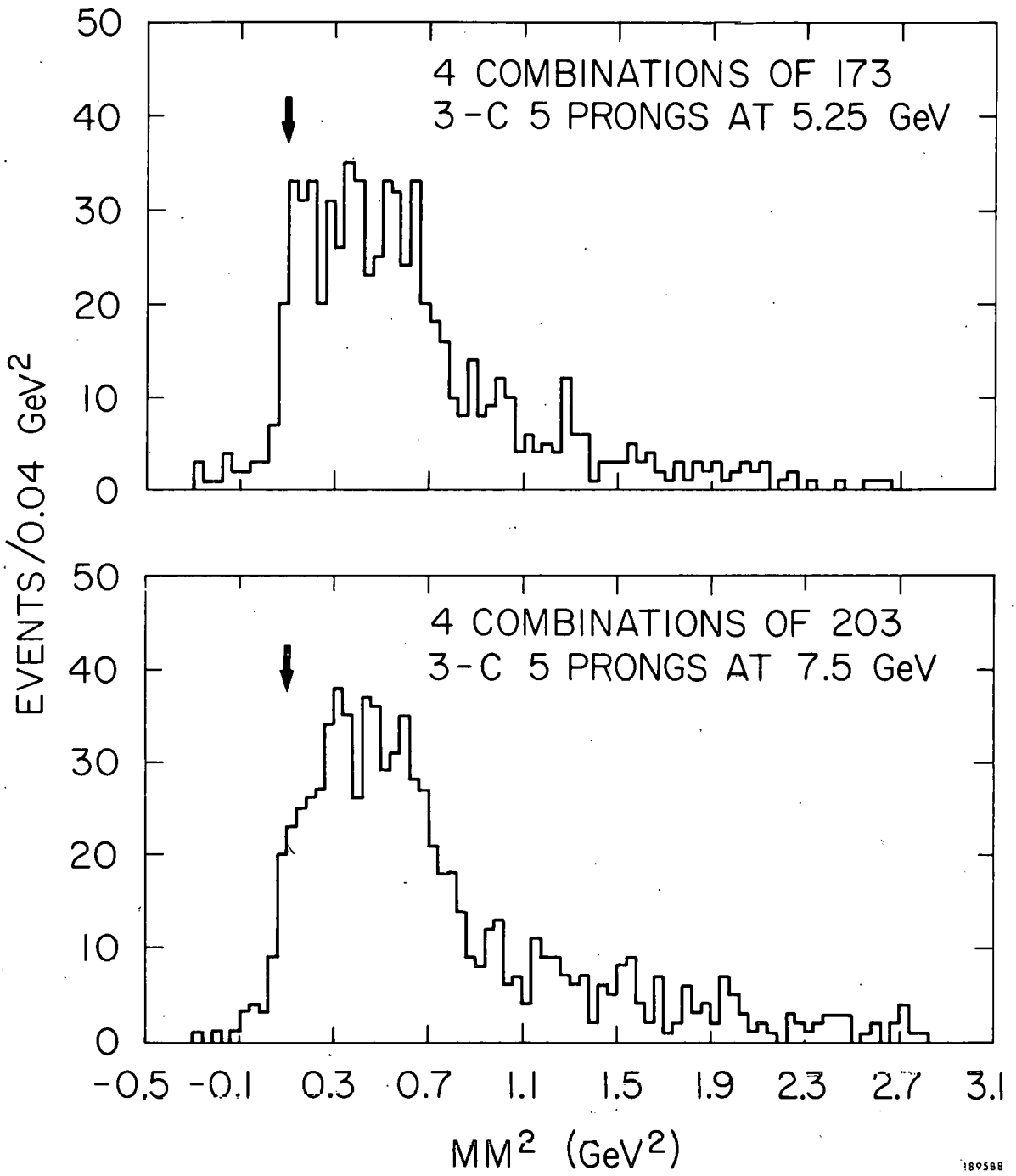

FIG. III. 8--Missing mass of 5 body events treated as 3 prongs to simulate the behavior of $\gamma p \longrightarrow p\pi^+\pi^-\pi^0\pi^0$ events. The arrows show the cut used to exclude multi-π^0 events.

Backgrounds to the Neutron Channel

Fig. III. 6b shows the missing mass squared for all three prongs making a 0-C fit to reaction (2). As can be seen, the sources of background considered were very diverse. One type, from reactions with fast protons, included misidentified events of $p\pi^+\pi^-\pi^o$ and $p\pi^+\pi^-\pi^o\pi^o$ which fit the hypothesis $\pi^+\pi^+\pi^-n$. These were studied using actual fits to ambiguous events in the channels $p\pi^+\pi^-\pi^o$ and $p\pi^+\pi^+\pi^-\pi^-$. Another type, from multineutral neutron events, included $\pi^+\pi^+\pi^-n\pi^o$. To transform from $p\pi^+\pi^+\pi^-\pi^-$ 3-C events to other 5-body charge states, the isospin weights of Shapiro[48] were used. The sum of these three backgrounds gives the solid line in Fig. III. 6b. The broken line above the solid background shows estimated bremsstrahlung levels, but as in the pi-zero case, these are not corrected from the graph, but in the quantitative way discussed above using PHONY. The net background within the limits of the cut of events not of the type $\pi^+\pi^+\pi^-n$ is therefore estimated to be 51 events for the 5.25 GeV data and 42 events for the 7.5 GeV data.

In Table III. 8 the net yields of 0-C fits within the cuts at each energy are given, along with the microbarn equivalents for those samples and the resulting cross sections for reaction (1A) and (2A) at the three energies. In making the calculation for the proton channel, the events in the omega region of the invariant mass spectrum were removed, a separate cross section calculation made for those events (see section IV. 2), and the omega cross section (without the 10% correction for neutral decay modes) was added to the cross section for non-omega events. This allowed the use of separate PHONY corrections and forward loss corrections for omega and non-omega events, which was necessary since omega production is much more

TABLE III. 8

Cross sections found for the reactions $\gamma p \rightarrow p\pi^+\pi^-\pi^o$ and $\gamma p \rightarrow n\pi^+\pi^+\pi^-$ at the annihilation peak energies, averaged over a photon energy interval approximately 1 GeV.

E_γ	$\gamma p \rightarrow p\pi^+\pi^-\pi^o$	$\gamma p \rightarrow n\pi^+\pi^+\pi^-$
4.3 GeV	18.2 ± 2.0 μb	7.5 ± 1.5 μb
5.25 GeV	13.5 ± 1.5 μb	4.6 ± 1.5 μb
7.5 GeV	11.8 ± 1.2 μb	4.0 ± 1.3 μb

Raw SLAC data $\gamma p \rightarrow \pi^+\pi^-\pi^o p$

	Unique 0-C Events in Cut Non-Omega	Omega	Background in Cut (non-ω)	Correction for Excluded Events	Non-ω Forward Loss Correction
5.25 GeV	394	67	10	0.916	1.5%
7.5 GeV	408	78	8	1.019	1.5%

Raw SLAC data $\gamma p \rightarrow \pi^+\pi^+\pi^- n$

	0-C Fits in Cut	Estimated Background from Other Reaction	Net True Events in Cut	Correction for Cuts and Brems	Estimated True $\gamma p \rightarrow \pi^+\pi^+\pi^- n$
5.25 GeV	208	54	154	1.032	159
7.5 GeV	196	42	154	1.131	175

peripheral than the rest of this channel. The events within the omega mass cut (0.68 GeV<m(3π)<0.88 GeV) were assumed to be unique, whereas the events of the channel $p\pi^+\pi^-\pi^o$ sometimes gave two fits (one with each positive track as the proton) which introduced some double-counting. This double counting has been corrected for by assigning weight 1/2 in preparing Table III.8. Recent results from the SLAC backscattered laser beam fit quite well with our data as shown in Fig. III.9.

The main sources of error here are the flux determination for the microbarn equivalent, the statistical error associated with the size of the sample, and the systematic errors associated with the PHONY corrections and background subtractions. The errors in the photon flux have been discussed extensively in section III.2 and the statistical error is the square root of the number of events in the sample. Also for the PHONY correction the error calculation is relatively straight forward, multiplying the percentage error in the number of events, $N^{-1/2}$, by a factor $(1 + |D|)^{1/2}$ where D is the percentage change in N resulting from the PHONY correction. This is analogous to the way the error due to the bremsstrahlung correction is incorporated into the flux error calculation in section III.2.

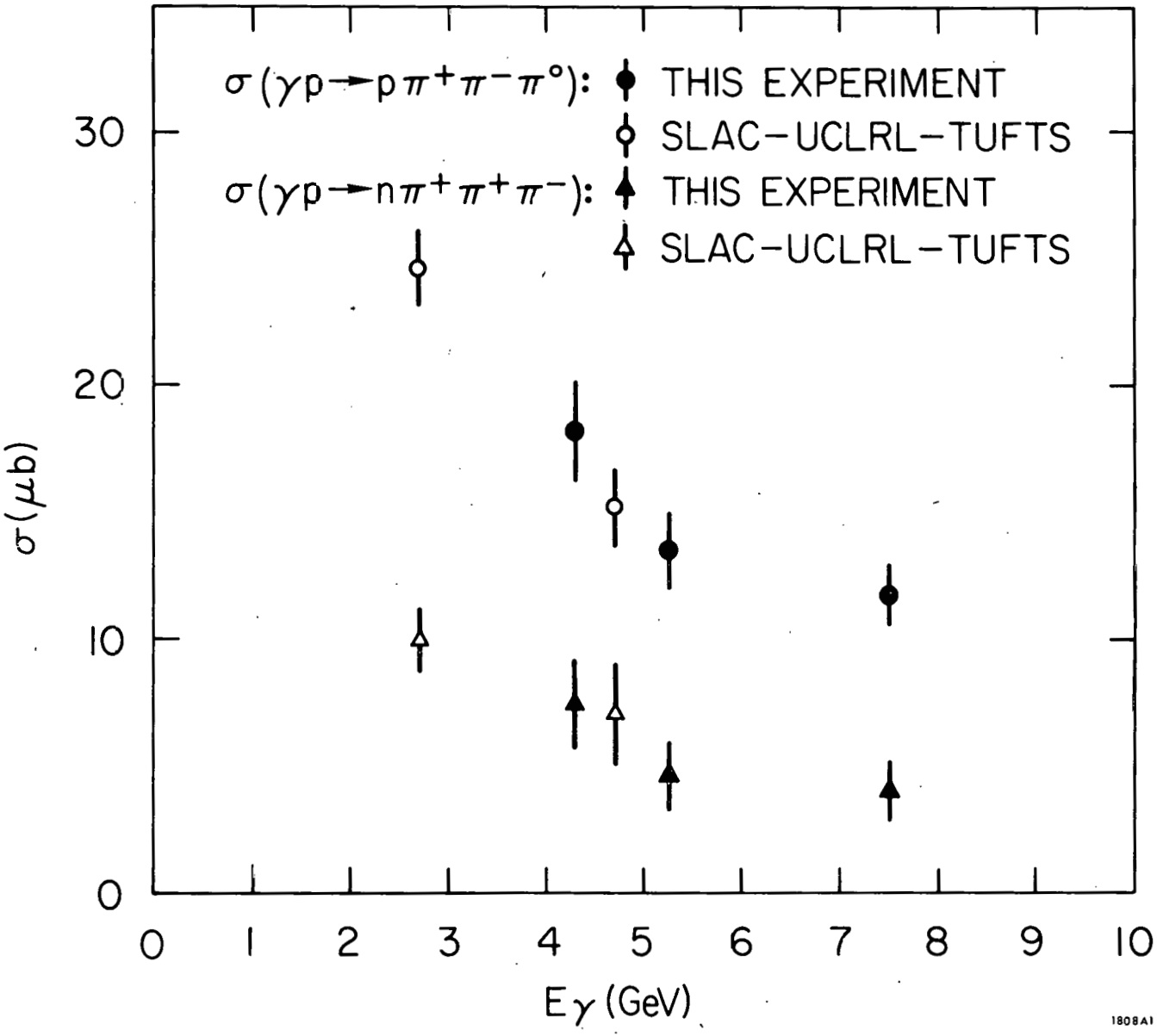

FIG. III.9-- Cross sections for 4-body reaction channels with a single neutral in the final state. For SLAC-UCLRL-Tufts points, see Ref. 31.

CHAPTER IV

PHOTOPRODUCTION OF NEUTRAL VECTOR MESONS

This chapter begins the presentation of the experimental data obtained in this experiment concerning specific reactions. Most attempts to understand the data in photoproduction are influenced by the vector dominance model (VDM).[14] VDM is currently the most comprehensive theoretical approach for explaining the photoproduction of hadrons. This approach is based on the SU(3) behavior of the photon as the U_0^0 member of the vector (1^-) meson octet expressed as:[40]

$$\gamma \rightarrow \frac{\sqrt{3}}{2}\rho^0 + \frac{1}{2}\left(\omega \sin\theta_V + \phi \cos\theta_V\right) , \qquad \text{(IV. 1)}$$

where θ_V is the mixing angle which correctly combines the SU(3) 1^- octet and singlet. If it is assumed that vector meson-proton scattering is the same for all mesons, this relation may be interpreted as giving the relative amplitudes for diffractive photoproduction of the neutral vector mesons rho, omega and phi. Note that the photon has both isovector (rho) and isoscalar (omega and phi) components.

Experimentally, the channel $p\pi^+\pi^-$ is increasingly dominated by neutral rho production as the incident photon energy increases.[11] Furthermore the omega meson stands out clearly above the background in the channel $p\pi^+\pi^-\pi^0$, even in the bremsstrahlung regions where only unconstrained fits are possible. This prominence of the omega meson in an otherwise very complicated channel is due primarily to its extremely narrow width. Therefore in this chapter the photoproduction reactions $\gamma p \rightarrow \rho^0 p$ and $\gamma p \rightarrow \omega p$ are studied and compared in light of vector dominance predictions. Unfortunately, since

this experiment did not study the photoproduction of strange particles, it is not possible to make the relevant comparisons of the phi meson to other vector mesons. Because the neutral rho meson is so dominant in the channel and because the small amount of nucleon resonances seen is almost entirely accounted for by certain models (e.g., the Söding interference model) introduced to explain the skewing of the $\pi^+\pi^-$ mass distribution, the entire examination of the 3-body channel is presented together. This includes a search for higher mass vector mesons as predicted by the Veneziano model.[15] Such mesons, if they were found, would then also have to appear in Eq. (IV.1).

The channel $p\pi^+\pi^-\pi^o$ is quite different, being neither so free of background as the 3-body channel (where all particles are measured) nor so dominated by a single reaction. Therefore omega production is singled out for presentation here due to its importance as a quasi-elastic, diffractively produced neutral vector meson. All other aspects of the 4-body final states, including inelastic ρ^o production (i.e., rhos produced off particle states other than protons), associated rho-delta production, charged A_2 production and charged rho meson production, are presented together in the final chapter.

IV.1 The Channel $\gamma p \longrightarrow p\pi^+\pi^-$

This reaction has been investigated in previous track chamber and counter experiments,[9-12] which showed that the reaction

$$\gamma p \longrightarrow \rho^o p \qquad \text{(IV.2)}$$

dominates the channel, has a roughly constant cross section with a sharply forward-peaked production angular distribution and is consistent with a natural parity t-channel exchange mechanism.[16,50] These observations have led to the interpretation of this reaction as a diffractive process. For squared

four-momentum transfer to the proton, $|t|$, less than 0.4 GeV^2 it appears[10,16] that s-channel helicity is conserved (i.e., no spin-flip at the γ-ρ vertex in the overall CMS). In addition a small contribution proportional to E_γ^{-2} from the reaction[9,10,29,51]

$$\gamma p \longrightarrow \pi^- \Delta^{++} \qquad \text{(IV.3)}$$

is observed. Evidence has been sought, but not found, for resonances other than ρ^o in the $\pi^+\pi^-$ mass system.[52] This section confirms these features in our data and shows that ρ^o production increasingly dominates the channel as incident energy increases.

A. ρ^o Production.

In Figs. IV.1-2 the invariant mass of the $\pi^+\pi^-$ system is shown for six photon energy ranges. The previously observed skewing of the dipion invariant mass distribution with respect to the usual Breit-Wigner shape becomes especially dramatic in the 7.5 GeV data (Fig. IV.2), there being almost no sign of a high mass tail to the distribution. In Fig. IV.2(b,c) the change of shape for the 7.5 GeV data with t is illustrated by plotting the mass distribution near the rho mass for $0 < |t| < 0.12$ GeV^2 and $0.12 < |t| < 0.40$ GeV^2. At large $|t|$ the mass distribution seems to approach a relativistic Breit-Wigner form (i.e., Eq. (IV.5a) below with a fixed Γ) as is shown by the solid curve, but at small $|t|$ the high mass tail is significantly below even the s-wave Breit-Wigner prediction.[53] This distortion means that a full analysis depends upon the production model adopted. The approaches used here generally follow those taken by the SLAC-Berkeley-Tufts (SBT) collaboration in their studies of ρ^o photoproduction.[16,30,32]

To present the raw data independent of models we begin with a purely phenomenological approach. It is assumed that the double differential cross

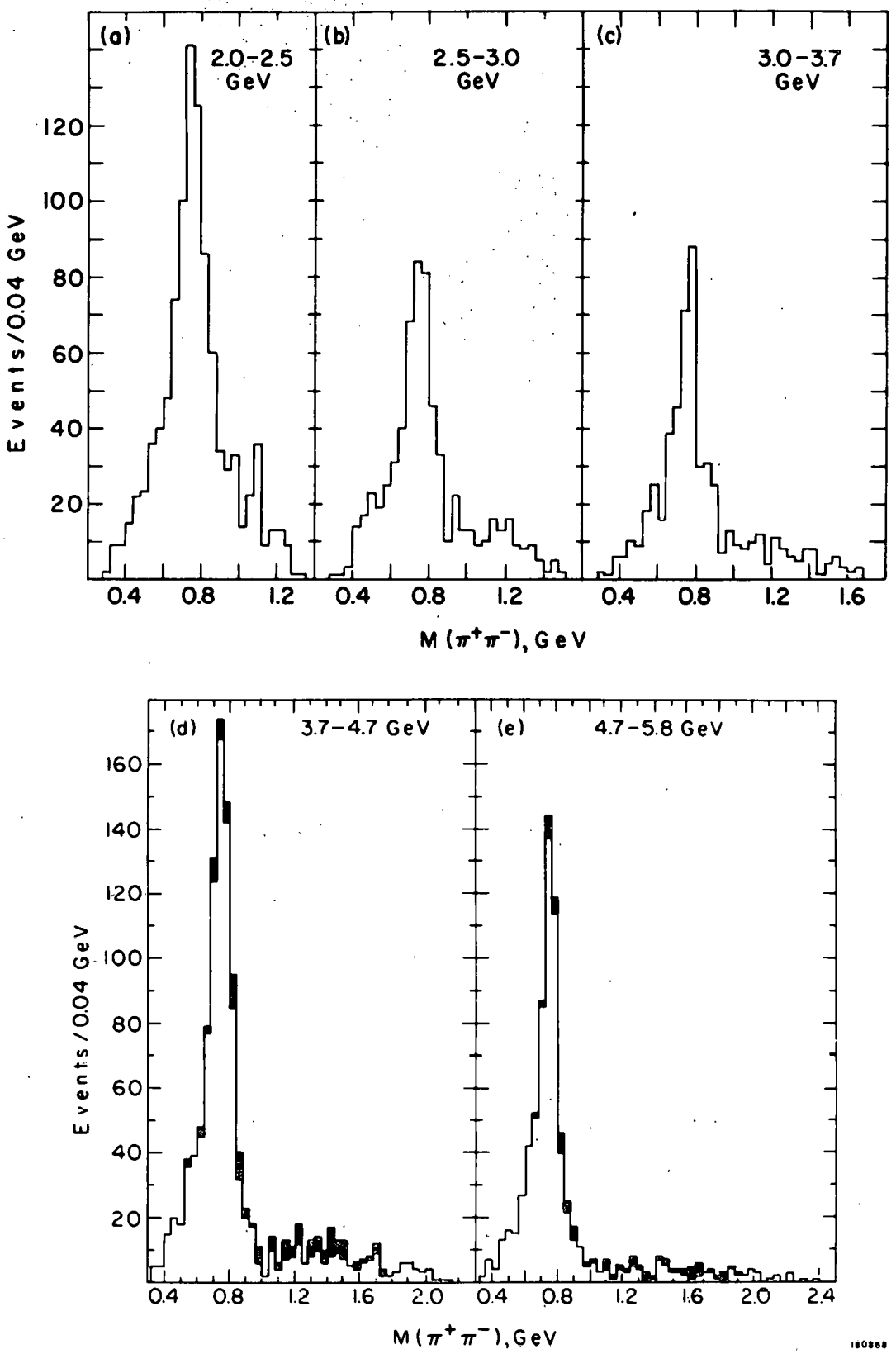

FIG. IV.1-- Dipion mass distributions for $\gamma p \longrightarrow p\pi^+\pi^-$ in the first 5 energy intervals as labelled. The darkened areas of (d) and (e) represent events with $p\pi^+$ mass in the $\Delta^{++}(1236)$ region ($1.12 < M(p\pi^+) < 1.35$ GeV and $|t(p,p\pi^-)| < 0.8$ GeV^2).

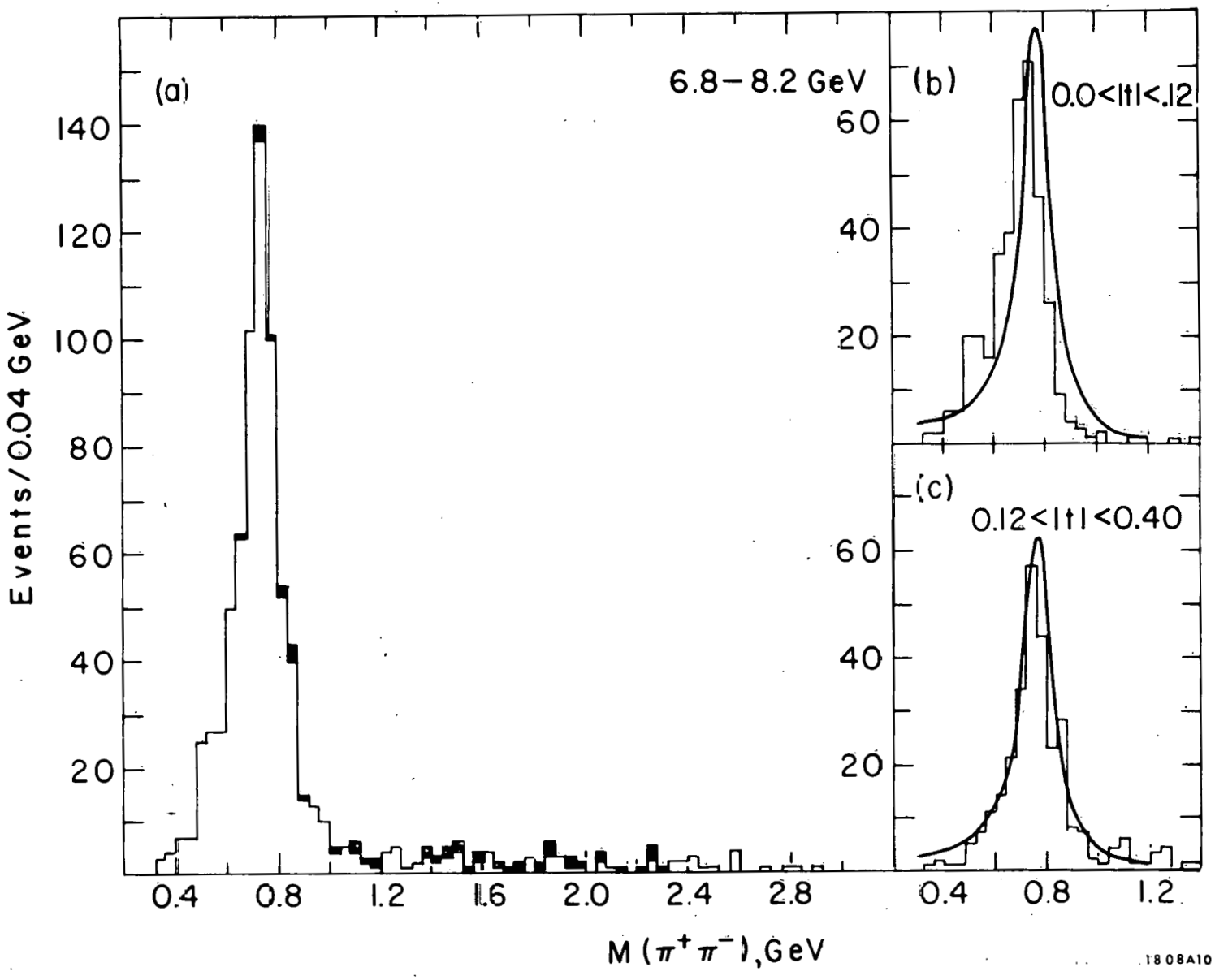

FIG. IV.2-- Dipion mass distributions for $\gamma p \longrightarrow p\pi^+\pi^-$ in the photon energy range 6.8-8.2 GeV. (a) All 4-C fits (darkened areas represent events with Δ^{++}, as in previous figure); (b) same distribution for fits with $0 < |t| < 0.12$ GeV^2; (c) same for $0.12 < |t| < 0.40$ GeV^2. The curves in (b) and (c) represent the same relativistic Breit-Wigner resonance, Eq. (IV.5a), with $m_\rho = 0.765$ GeV and a fixed width $\Gamma_\rho = 0.140$ GeV.

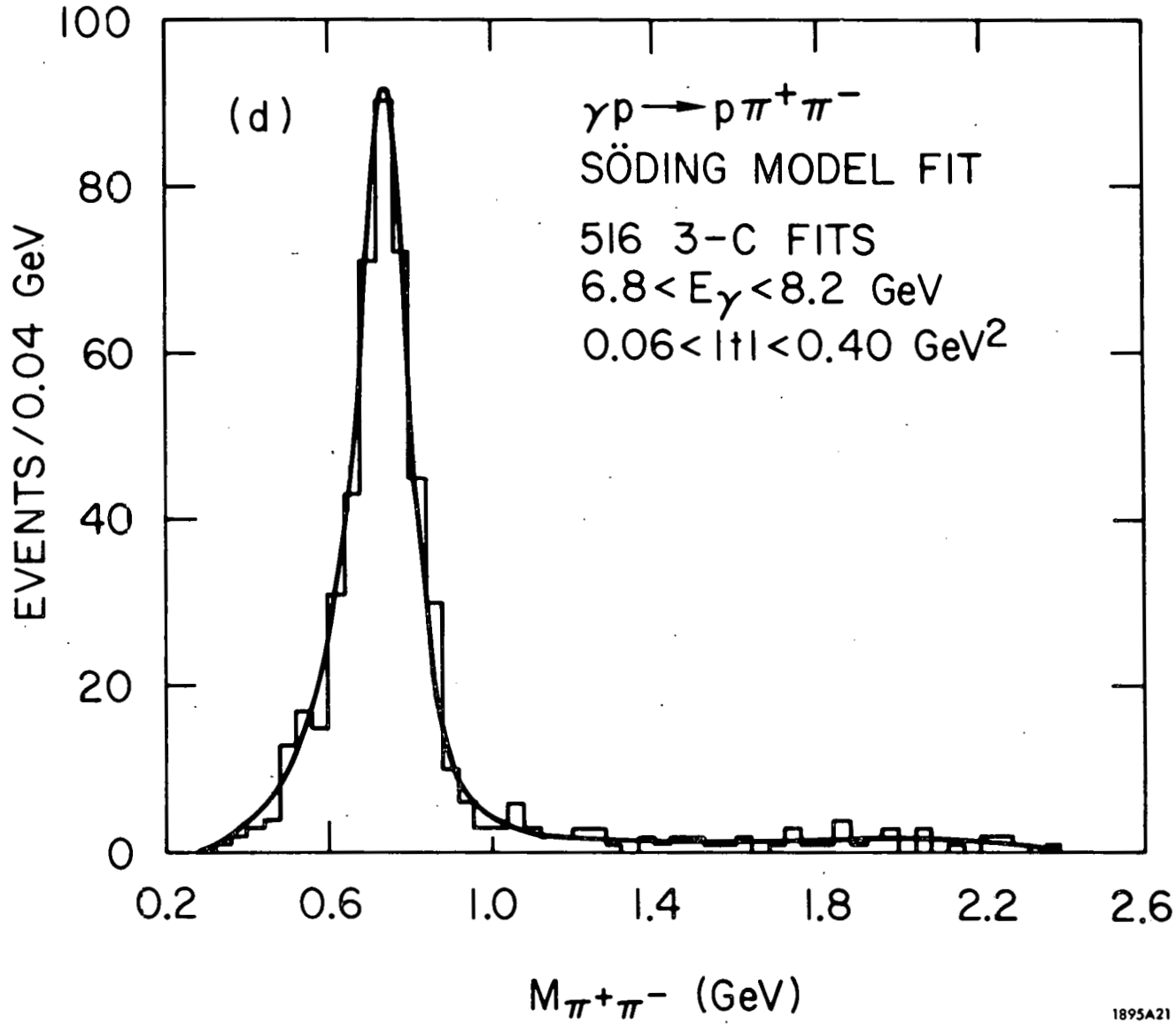

FIG. IV.2 (cont'd.)

(d) Söding model fit curve superimposed on 3-C event data for $0.06 < |t| < 0.40$ GeV^2. This fit gave χ^2 of 12.6/18. A fit to the same data using the phenomenological model in this t range was indistinguishable from the Söding fit curve.

FIG. IV.2 (cont'd.)

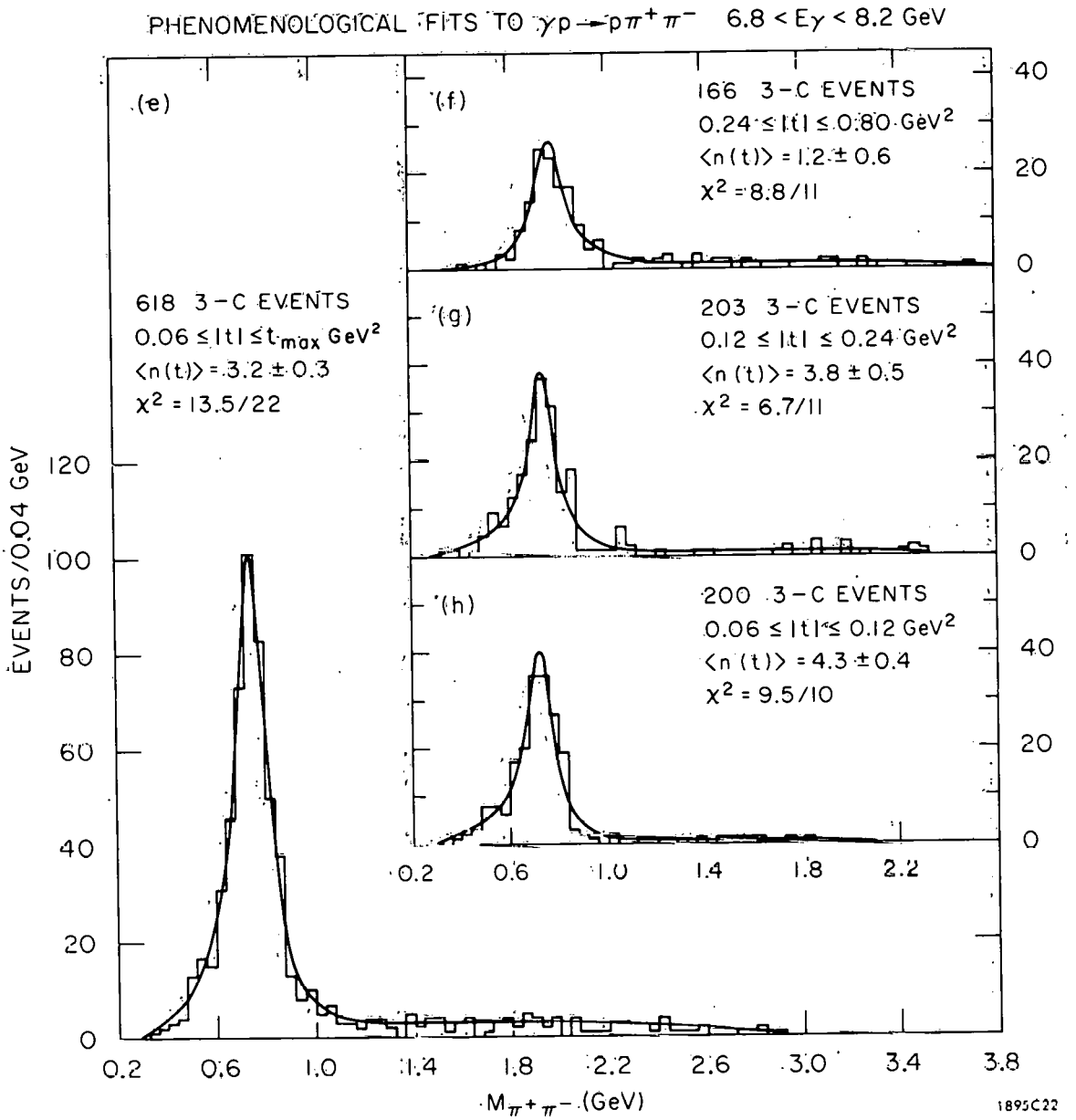

(e) Phenomenological model fit curve superimposed on 3-C event data with $6.8 < E_\gamma < 8.2$ GeV for $0.06\ \text{GeV}^2 < |t| < t_{max}$. (f-h) Phenomenological model fits in three different t intervals, each a subset of the data in (e). The variation of the exponent n(t) is illustrated by these fits.

section for dipion production with $|t| < 0.4$ GeV^2 may be described by the form

$$\frac{d^2\sigma}{dtdm} = Ae^{Bt} , \qquad \text{(IV.4)}$$

with A and B functions of m, the dipion invariant mass. Fig. IV.3 shows the t distributions for events with m in the rho region, ($0.60<m<0.85$ GeV), which show that Eq. (IV.4) represents this region well. A loss in scanning of events at small t is evident here. A and B have been determined for fixed intervals in m for events with $0.06< |t| <0.4$ GeV^2 using the "average-t" method as explained below. The resulting forward cross sections and slopes are shown in Fig. IV.4. The variation of slope with mass becomes more marked at the highest energies but is consistent with the same value in a symmetric interval about the rho mass ($0.715<m<0.815$ GeV), namely $B=7.0\pm0.4$ GeV^{-2} for photon energies in the range from 4 to 8 GeV. This agrees well with the results of the SLAC-Berkeley-Tufts collaboration which found $B=6.6\pm0.5$ GeV^{-2} at a photon energy of 4.7 GeV.

To make a more detailed analysis of ρ^o photoproduction, it is necessary to use specific production models. The production models suggested in the literature fall into two classes: i) the interference model of Söding[17] and ii) the kinematic skewing or phenomenological models, such as the one originally suggested by Ross and Stodolsky.[54] The first class also includes other interference models differing from that of Söding in the details of the interfering background;[17] the second includes any modifications of the kinematic factor, such as the models of Kramer and Uretsky or Mannheim and Maor,[55] or the variable exponent used with the Ross-Stodolsky factor in Ref. 16. By fitting the data with such models, very accurate determinations of

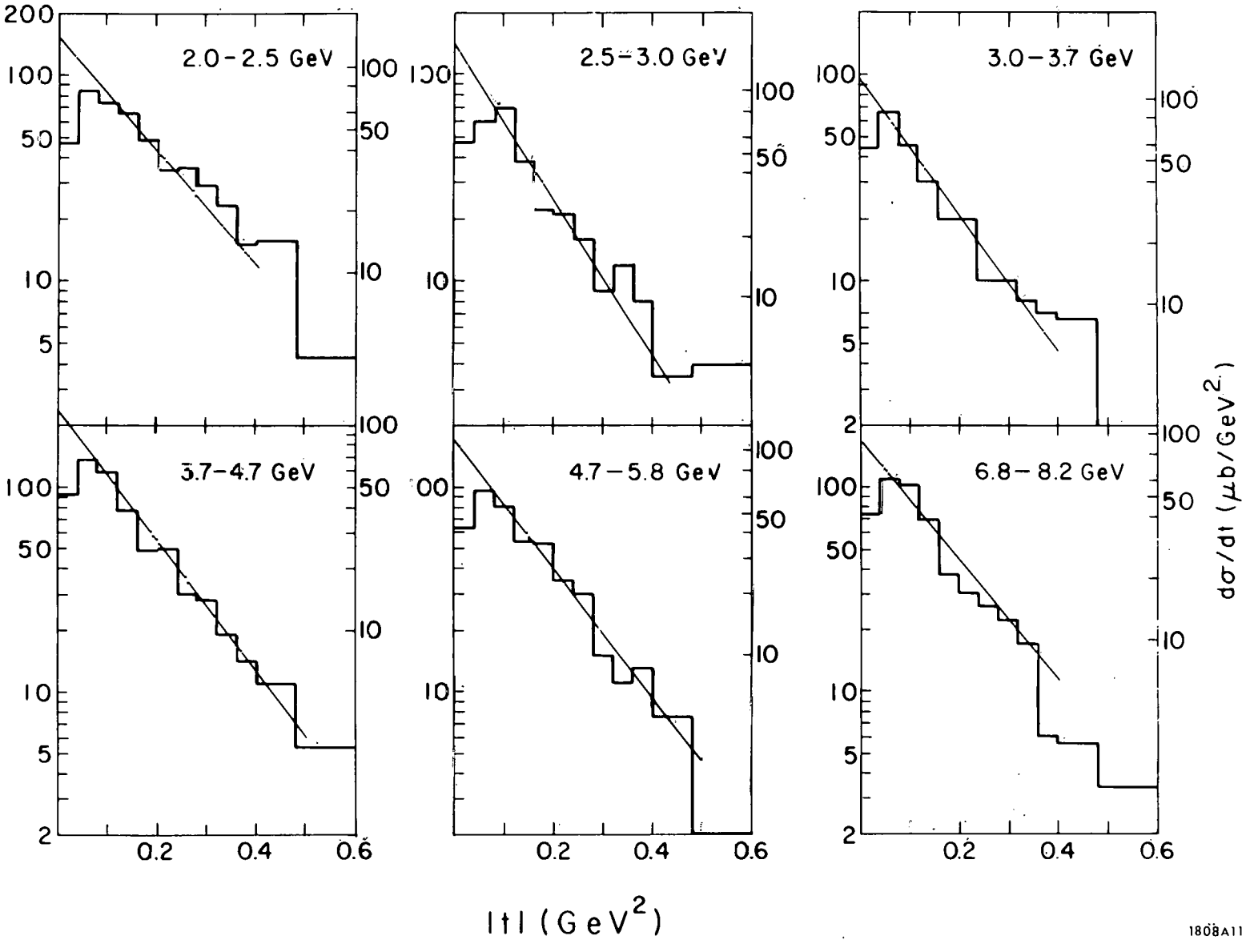

FIG. IV.3-- | t | distributions for events in the ρ^0 region (0.60 m 0.85 GeV) for various E_γ intervals. The right-hand side scale and the curves represent $d\sigma/dt$ for the phenomenological fit (Table IV.2).

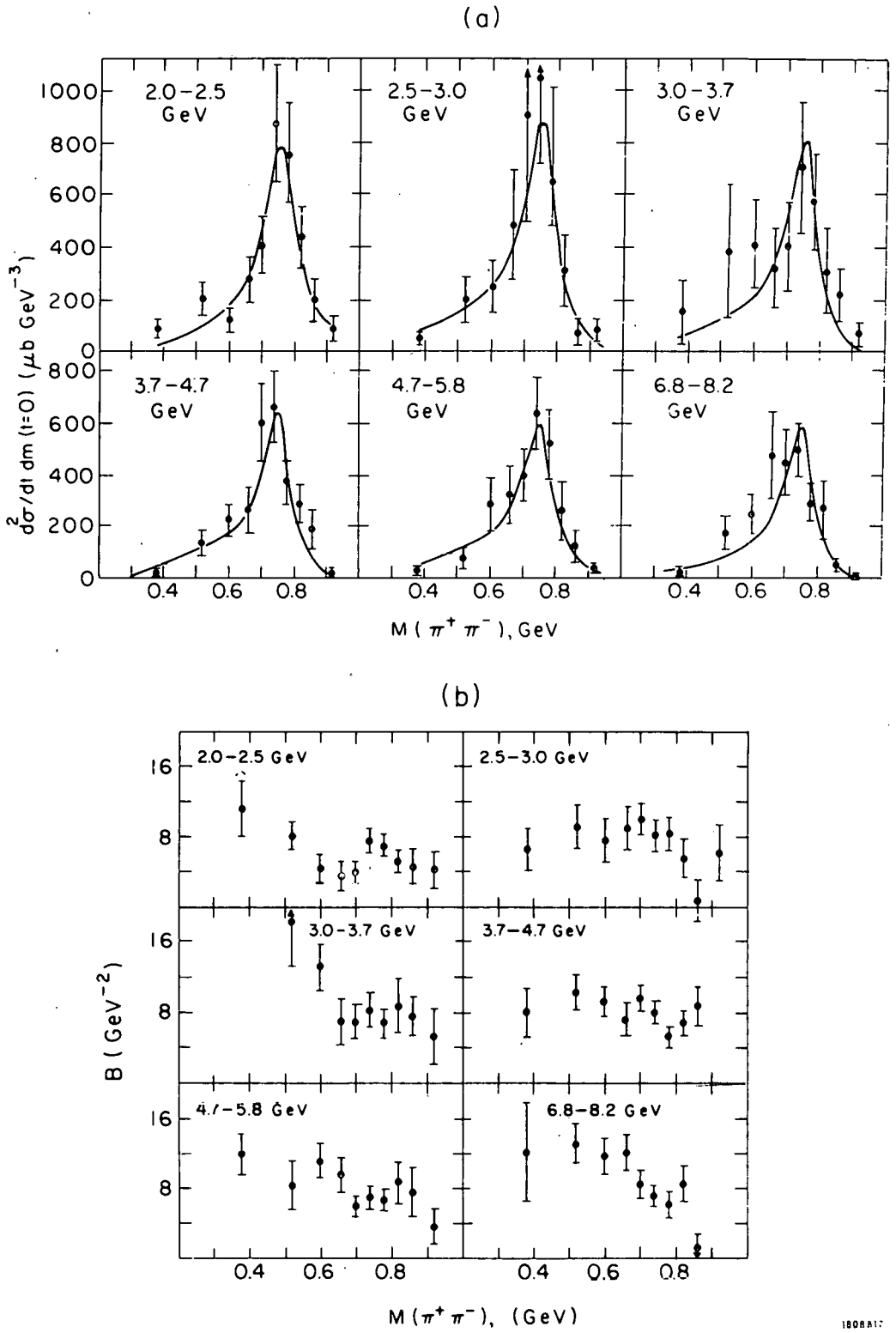

FIG. IV.4-- (a) Double differential cross section $d^2\sigma/dtdm$ (t=0). The curves are the phenomenological shapes described in text (Eq. IV.5) with $\Gamma_\rho = 0.125$ GeV, $m_\rho = 0.765$ GeV). The exponent n=6 was used at all energies except $E_\gamma = 2.0$-2.5 GeV, where n=4 has been used. (b) The slope B for the interval $0.06 < |t| < 0.40$ GeV^2 as a function of the dipion mass.

the quantities A(m) and B(m) can be made if the models provide a good interpolation of the data points. A particular example of each class has been used to provide functional forms describing the dipion production data. These have been fitted to obtain ρ^0 cross sections and values for the mass and width of the rho. Applied to the same data, these values differ by small amounts which may be regarded as a measure of the theoretical uncertainty inherent in the choice of models. The results of these two fitting procedures are shown in Table IV. 1. A third set of cross sections has been derived from the intensity of dipion pair production near the rho mass by determining $A(m_\rho)$ from the raw experimental dipion mass spectrum in order to be as model independent as possible. Therefore three sets of photoproduction cross sections have been determined. These are 1) Söding fit values, 2) kinematic skewing (phenomenological) values, and 3) "standard" values. The true ρ^0 cross sections presumably lie somewhere within the range of these values. In the Söding and the standard methods the cross sections quoted may be interpreted as for an "undistorted" rho, which should be most relevant for making VDM comparisons. Detailed descriptions of these three fitting procedures follow.

1. Söding Fits. It has been shown in Ref. 16 that the Söding interference model explains most of the characteristics of ρ^0 production at 2.8 and 4.7 GeV, including the shape of the dipion mass distribution and its t dependence. In this model the major rho amplitude is from a diffractively produced ρ^0 (Fig. IV.5a) as in VDM. The distorted ρ^0 shape is due to the interference of the diffractive amplitude with a p wave non-resonant $\pi^+\pi^-$ background due to the Drell diagrams[56] (Figs. IV. 5b, IV. 5c). The Drell amplitude is assumed to have a nearly constant phase, interfering

TABLE IV.1

Raw and corrected events and cross sections for the channel $\gamma p \rightarrow p\pi^+\pi^-$. Fitted masses, widths and total cross sections for ρ^o produced in $\gamma p \rightarrow \rho^o p$ as obtained by the phenomenological and Söding fits made in the interval $0.06 < |t| < 0.4$ GeV^2. Cross sections are corrected for other t values assuming a linear exponential.

E_γ(GeV)	Channel Events and Cross Sections			Phenomenological Fits			Söding Fits		
	uncorrected	corrected	$\sigma(p\pi^+\pi^-)$ (μb)	m_p(MeV)	Γ_0(MeV)	$\sigma_\rho(\mu b)$	m_ρ(MeV)	Γ_0(MeV)	$\sigma_\rho(\mu b)$
2.0-2.5	1001	1001	36.5±2.0	769±6	144±14	22.1±1.4	764±7	143±12	19.1±1.7
2.5-3.0	642	642	31.2±2.2	772±6	136±15	21.4±1.6	765±8	146±15	18.5±1.9
3.0-3.7	552	588	26.3±2.0	772±7	141±18	18.7±1.6	773±8	140±15	15.7±1.7
3.7-4.7	775	852	21.5±1.2	769±6	134±10	16.2±1.7	774±5	142±10	14.7±1.7
4.7-5.8	536	606	19.0±1.2	759±4	110±10	15.4±1.4	754±5	122±12	16.6±1.7
6.8-8.2	809	917	16.0±10	758±5	151±11	13.7±1.3	771±6	147±10	14.3±1.3

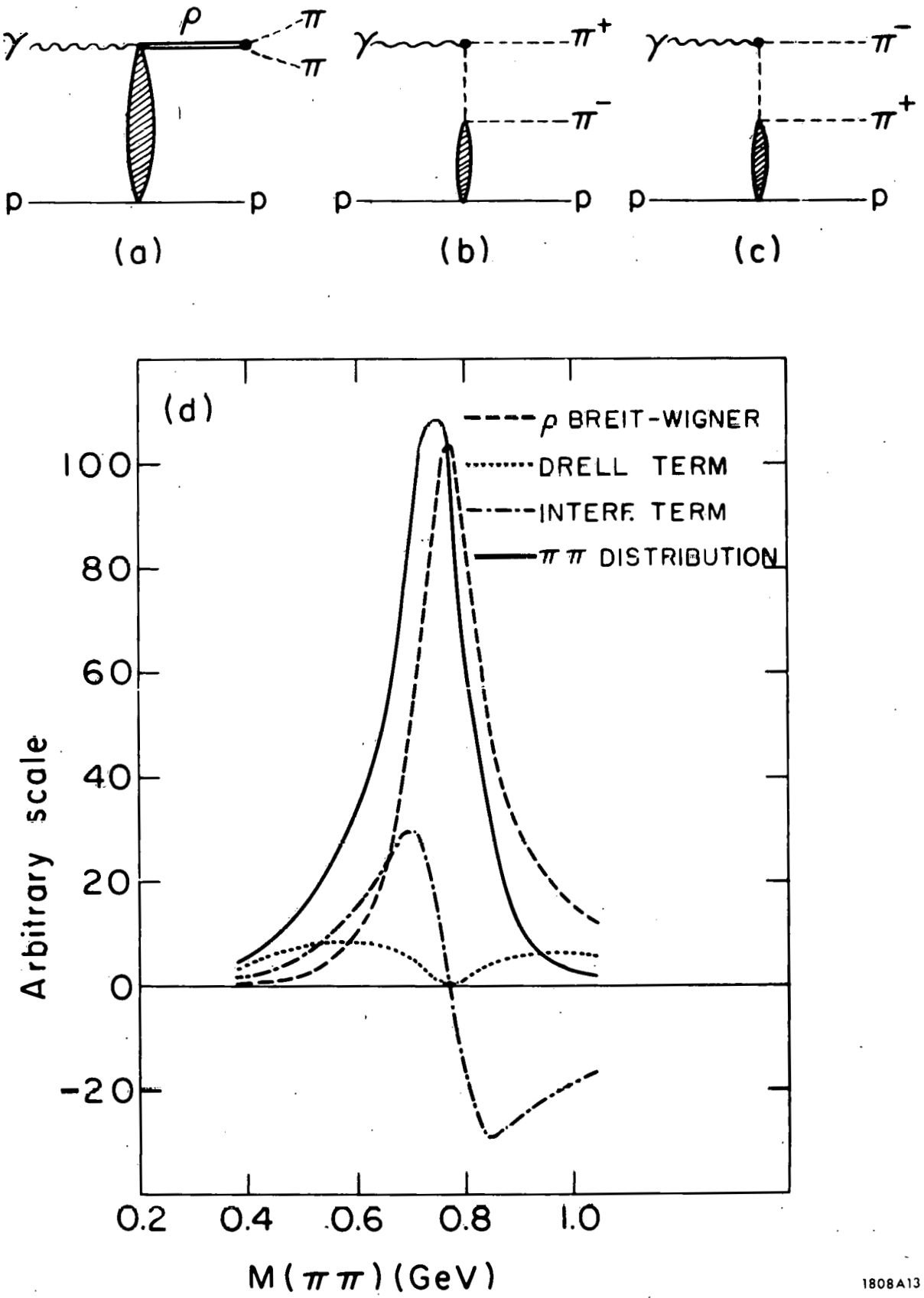

FIG. IV.5-- (a-c) The contributing diagrams in the Söding model. (d) The contributions of the Drell, interference and p-wave Breit-Wigner terms to the $\gamma p \longrightarrow p\pi^+\pi^-$ cross sections at 7.5 GeV. The distributions are normalized to the number of Drell, interference and ρ^0 events obtained with the Söding fit.

FIG. IV.5 (cont'd.)

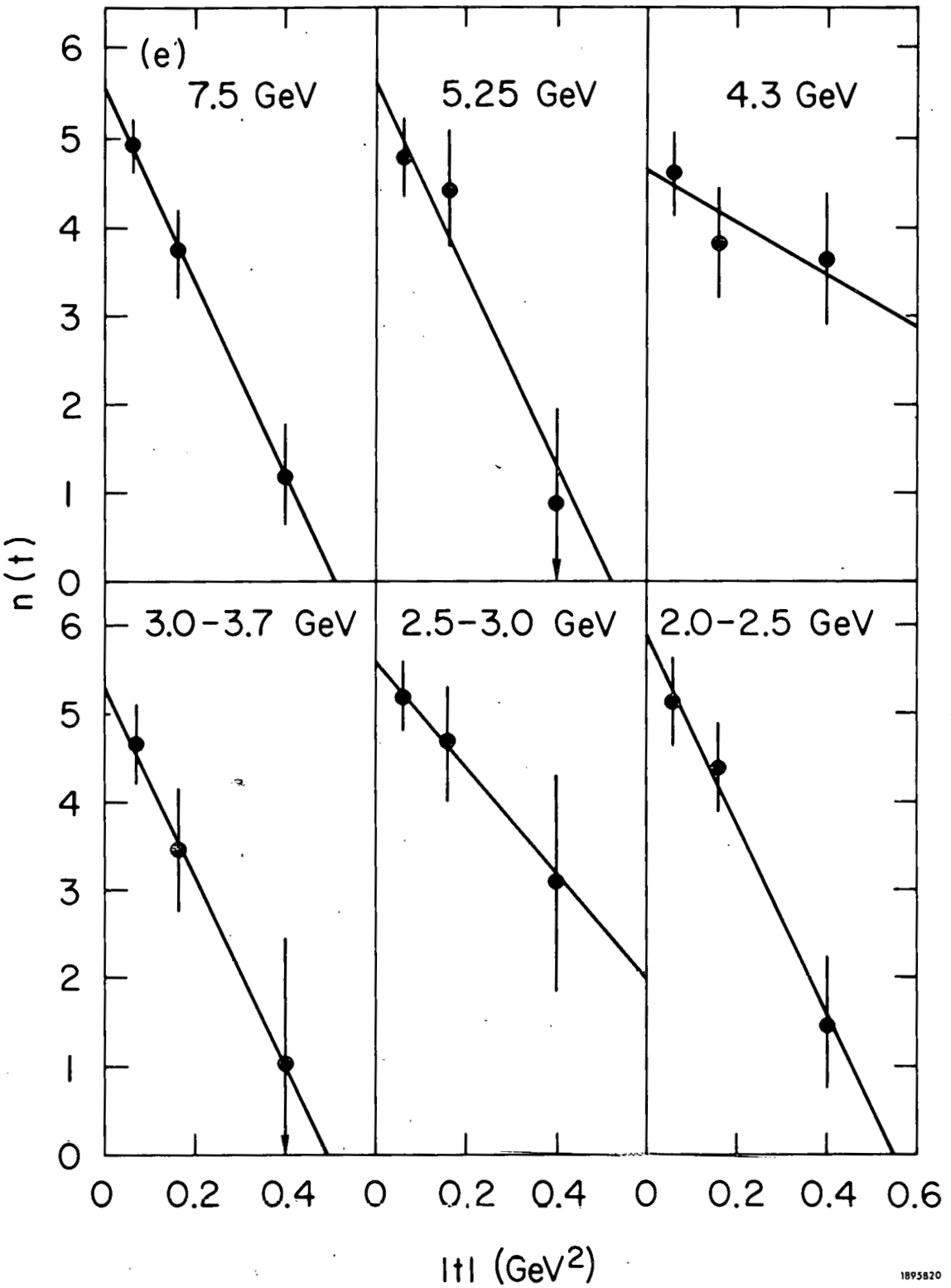

(e) The variation of the phenomenological exponent n(t) with t for all 6 energy intervals. The lines are best fits of the data to straight lines. The data has been fit in the t intervals 0-0.12, 0.12-0.24, and 0.24-0.80 GeV^2 (e.g., see Figs., IV.2f-h).

constructively below the central mass of the ρ^o and destructively above it to produce the observed mass skewing. For the quantitative evaluation of cross-sections we followed closely the procedure used in Ref. 16. If M_1, M_2, and M_3 are the matrix elements for the diagrams in Figs. IV.5a, IV.5b, and IV.5c, then the cross-sections for diffractive ρ^o production, the "Drell-term" and the interference term are proportional to $|M_1|^2$, $|M_2+M_3|^2$, and $2\mathrm{Re}|M_1^*(M_2+M_3)|$ respectively. In the calculations the explicit formulae given by Söding for M_1, M_2, and M_3 as well as his computer program [17] were used with the following changes (See footnote 13 in Ref. 16). First, the t dependence of diffractive ρ^o production has been approximated by $M_1 \propto \exp(Bt/2)$. Second, the amplitudes $T_\pm(s,t)$ which describe the πN interaction at the lower vertex were evaluated from the πN phase-shift data for $M(p\pi)<1.74$ GeV. The virtuality of the interacting pion was accounted for by multiplying the amplitudes $T_\pm(s,t)$ by a Ferrari-Selleri type form factor.[57] Third, double counting was avoided by multiplying the Drell matrix element by the factor $e^{i\delta}\cos\delta$, where δ is the p-wave phase shift associated with the ρ^o in elastic $\pi\pi$ scattering,[58] which corrects for the rescattering of the dipion system to form a ρ^o indistinguishable from that produced directly. To evaluate the rho cross-sections, events of reaction (IV.2) were fitted to an incoherent sum of three distributions given by: (a) the diagrams IV.5(a-c), (b) the reaction $\gamma p \longrightarrow \pi^- \Delta^{++}$, and (c) Lorentz-invariant phase space. The rho mass, width and slope were free parameters determined by the fitting program. Practically no phase space was required by the fit and most of the $\pi^- \Delta^{++}$ events were accounted for by the Drell term without a need for additional $\gamma p \longrightarrow \pi^- \Delta^{++}$ events. The cross-section for $\gamma p \longrightarrow \rho^o p$ was determined by integrating $|M_1|^2$ over the available mass range while the

$|M_2+M_3|^2$ and interference terms were regarded as background. Typical calculated results, shown in Fig. IV.5d, illustrate the relative importance of the diffractive ρ^o term, the Drell term, and the interference term in the resulting dipion mass distribution at 7.5 GeV. The comparison between the raw data and the Söding fit shown in Fig. IV.2d shows that this method gives an excellent representation of the experimental results.

The parameters m_ρ, Γ_ρ, and B of the Söding model were determined from a fit in the t region $|t_1| = 0.06 < |t| < |t_2| = 0.4$ GeV^2. The cross section for ρ^o events in this t range, $\sigma_\rho(t_1, t_2)$, was then increased by the ratio of $|M_1|^2$ integrated over the entire physical region of phase space to $|M_1|^2$ integrated over the restricted portion of the physical region where $0.06 < |t| < 0.4$ GeV^2 in order to obtain the total ρ^o cross section. Using the slope determined for $0.06 < |t| < 0.4$ GeV^2 in the integral over the entire physical region for dipion production is equivalent to the usual forward loss correction.

The forward ρ^o cross section was also computed from $\sigma_\rho(t_1, t_2)$ by an extrapolation to t=0 using:

$$\frac{d\sigma}{dt}^{Söd}(t=0) = \frac{B^{Söd}\sigma_\rho(t_1, t_2)}{\exp(B^{Söd}t_1) - \exp(B^{Söd}t_2)} .$$

This method avoids the effects of scanning losses at small t and the distortion by the kinematic boundary at t_{min}, the minimum momentum transfer. The resulting fit parameters and cross sections are given in Tables IV.1 and IV.2.

TABLE IV.2

Forward cross sections and slopes for the ρ^0 as obtained by the three methods, and double forward differential cross sections for $m_{\pi\pi}$ = .715 - .815 GeV. Slopes B were determined in the range $0.06 \leq |t| \leq 0.4$ GeV^2.

E_γ(GeV)	$\frac{d\sigma}{dt}(t=0)$ (μb · GeV^{-2})			B (GeV^{-2})			$\langle\frac{d^2\sigma}{dtdm}(t=0)\rangle$ $m_{\pi\pi}$ = .715 -.815 GeV (μb GeV^{-3})†
	Phenom.	Soding	Standard†	Phenom.	Söding	Standard†	
2.0 - 2.5	138 ± 20	143 ± 14	180 ± 20	5.9 ± .7	5.4 ± .5	6.7 ± .9	770 ± 90
2.5 - 3.0	179 ± 27	170 ± 17	184 ± 25	7.7 ± .9	6.4 ± .6	7.5 ± 1.1	780 ± 110
3.0 - 3.7	159 ± 26	160 ± 16	152 ± 22	8.2 ± 1.0	7.1 ± .7	7.5 ± 1.2	650 ± 100
3.7 - 4.7	130 ± 13	100 ± 10	105 ± 10	7.5 ± .6	6.5 ± .5	6.8 ± .7	450 ± 45
4.7 - 5.8	123 ± 14	132 ± 13	117 ± 12	7.6 ± .6	7.7 ± .6	6.7 ± .8	500 ± 55
6.8 - 8.2	124 ± 11	102 ± 10	90 ± 10	7.5 ± .6	7.1 ± .6	7.0 ± .8	380 ± 40

†No incoherent background correction.

2. Phenomenological Fits. In this method, the shape of the neutral rho was parametrized by:[16]

$$P(m) = \left(\frac{m_\rho}{m}\right)^{n(t)} f(m)L(m) \ , \qquad \text{(IV.5)}$$

where[59]

$$f(m) = \frac{\Gamma(m)}{(m_\rho^2 - m^2)^2 + m_\rho^2\Gamma^2(m)} \qquad \text{(IV.5a)}$$

and

$$\Gamma(m) = \left(\frac{q}{q_\rho}\right)^3 \frac{2q_\rho^2}{q_\rho^2 + q^2} \ , \ \Gamma_\rho \ . \qquad \text{(IV.5b)}$$

L(m) is a Lorentz-invariant two-body phase space factor, q and q_ρ are the π momenta in the dipion rest frame for dipion masses of m and m_ρ respectively. Eq. (IV.5) is essentially the Ross-Stodolsky form where the constant exponent is replaced by a t-dependent exponent n(t), which represents a departure from the procedure used in our preliminary reports.[2,3] This modification, introduced in Ref. 16, describes the experimental data well. When fitted over the full range of t, $< n(t) > \simeq 4$ at all energies. However, when the fit is repeated for distinct t intervals, n(t) is found to be a function of t, decreasing from about 5.5 at t=0 to about 0 at large t values ($|t| > 0.5$ GeV^2), in agreement with the results of Ref. 16. Fig. IV.5e shows how the distorted shape changes strongly as a function of t at all energies. It is interesting to note that the exponential skewing factor, n(t), exhibits similar behavior at all energies, suggesting that the true mass skewing mechanism is a relatively energy-independent effect. In the Ross-Stodolsky model, the low $\pi\pi$-mass enhancement is presumed to originate from genuine

ρ^0 events. Although this interpretation would explain the ρ^0 decay angular distribution, which has a $\sin^2\theta_H$ distribution in the dipion center of mass for all $m<1.0$ GeV, in the Söding interference interpretation such an angular distribution is also provided by the Drell term. The parametrization fits can be used to provide a smooth interpolation between raw data points, as can be seen for the 7.5 GeV data in Figs. IV.2(e-h).

As in the Söding fits, contributions from the reaction $\gamma p \longrightarrow \pi^- \Delta^{++}$ and from Lorentz-invariant phase-space have also been allowed. The fractions of ρ^0, $\pi^- \Delta^{++}$ and phase space were fitted together with the mass, width and $<n(t)>$. The rho slope and forward cross sections were derived by repeating the fit in t-intervals and fitting the resulting ρ^0 cross sections to the exponential form (IV.4) in the range $0.06<|t|<0.4$ GeV^2. This fit to the differential cross section was also used to correct the total phenomenological ρ^0 cross section for $|t_{min}|<|t|<0.06$ GeV^2. Tables IV.1 and IV.2 list the values found.

Both of the above models suffer from theoretical deficiencies. The phenomenological model, as is implied by the name, has been empirically developed to fit the data with almost no theoretical basis. Although the diffraction dissociation model of Ross and Stodolsky[54] originally suggested using the kinematic factor $(m_\rho/m)^4$ only for small four-momentum transfers, the high statistics of the SBT collaboration[16] showed that to fit the data well the exponent must be a function of t, which has no theoretical underpinning. The moment analysis of Ref. 16 does show evidence for an interference term which changes sign at the rho mass, which supports the physical picture of a diffractive rho interfering with a Drell background (see Figs. IV.5a-c). The Söding model, however, has other problems, despite the fact that it gives an

excellent fit to all aspects of the experimental data. There is uncertainty in how the exchanged pion should be corrected for its off mass shell behavior. We used the Ferrari-Selleri form factor mentioned above, but Benecke and Durr[57] have suggested another form factor. The latter, however, gives fitted rho widths which were consistently about 20 MeV larger than the Ferrari-Selleri, and which were on the average larger than widths expected for the rho meson. Fortunately, the cross sections and fitted rho masses vary less, but still this ambiguity underscores our lack of knowledge of the correct form factor to use. Also some theoreticians question the use of any form factors in photoproduction.[57] Furthermore, as has been pointed out by Yennie[60] and even by Söding himself, other diagrams besides the Drell diagram must be considered for gauge invariance. Yennie argues that these other contributions could be significant, but realizing that in any case a great deal of the non-diffractive background must vanish at the rho mass, he suggests a very accurate experimental determination of the shape of the dipion mass distribution near the rho mass and especially at m_ρ itself. These observations form the basis for the so called standard method.

3. "Standard" Method. A common feature of the two classes of models discussed above is that, apart from a small incoherent background, the value of A in equation (IV.4) at $m=m_\rho$ is just that given by the peak of a Breit-Wigner resonance shape describing an undistorted rho meson. In the interference model, the interference term goes through zero at $m=m_\rho$ and even the "Drell" intensity vanishes because of the rescattering corrections introduced. For the kinematic explanations of the skewed distribution, the skewing factor in all cases becomes unity by definition at the rho mass.

Hence, by interpolating the data shown in Fig. IV.4 to $m=m_\rho$ one could find the total forward cross section by multiplying $A(m_\rho)$ (corrected for incoherent background) by a factor F which depends only on the ρ^o meson width, Γ_ρ, assumed and on the exact form chosen to describe a p-wave resonance. Since the undistorted ρ^o is assumed to have the form (IV.5a) above, F is then given by $F = \int f(m) dm^2/(2m_\rho f(m_\rho))$. However, this method is not a fit and provides no estimate of incoherent background; therefore it will only be reliable for data at the higher energies where such background is found to be small by the previous fitting procedures.

This method is standard in the sense that it presents the raw data from the double differential cross section (IV.4) in a form as closely analogous to the ρ^o cross sections usually quoted as possible. Because the number obtained in this way is directly proportional to the height of the best fit to the raw data at the value adopted for the rho mass, all experiments can be easily compared when analyzed by this method. Also it illustrates explicitly the dependence of the cross sections obtained on the choices made for the mass and width, which can be substantial because of the steep slope of the dipion mass distribution in the region of the rho mass. These uncertainties are above and beyond the usual experimental errors. Since VDM allows a comparison of photoproduction and Compton scattering (see Section IV.3), the zero width limit of the Breit-Wigner form has been taken in which $F=\pi\Gamma_\rho/2$, with Γ_ρ=130 MeV and m_ρ=765 MeV as suggested by D. R. Yennie.[60] The "standard" forward cross section then becomes

$$\frac{d\sigma}{dt}(\rho)\Big|_{t=0} = \frac{\pi\Gamma_\rho}{2}\frac{d^2\sigma}{dtdm}\ (m=m_\rho,\ t=0) = \frac{\pi\Gamma_\rho A(m_\rho)}{2} \qquad \text{(IV.6)}$$

which merely expresses $A(m_\rho)$ in a more recognizable way. It is, as mentioned above, useful for comparing experiments; in particular, the counter results of McClellan et. al.[12] have been obtained by this method.

This standard method requires an interpolation function if an accurate determination of the height of the data at the rho mass is desired. Since the production models discussed above have been shown to reproduce the raw data with high accuracy,[10,16] one possible procedure is to obtain the best fit to the raw data with the model, use this to find $d^2\sigma/dtdm$ at $m=m_\rho$ and $t=0$, and then multiply by F as given above. Although a good interpolation can be made to the forward cross section data, the fit curves are very steep in the region of the rho mass (see Fig. IV.2d,e), so a small error in the rho mass can cause a significant change in $A(m_\rho)$. While these sensitivities cannot be avoided, it is possible to calculate $A(m_\rho)$ in a more direct way from the data. Numerical calculations have shown that for the interval (715, 815) MeV, symmetric about the value of the rho mass used (765 MeV), the form (IV.5) has the same area to 2% precision for any n between 0 and 6. This means that the number of events in this symmetric interval under an undistorted Breit-Wigner shape ((IV.5) with n=0) is essentially the same as under the distorted shape. By numerical integration using $m_\rho = 765$ and $\Gamma_\rho = 130$ MeV, the expected value of the double differential cross section in this 100 MeV interval has been related to the height of this cross section at the rho mass:

$$\frac{d\sigma_\rho}{dt} = \frac{\pi\Gamma_\rho}{2} \frac{d^2\sigma_\rho}{dtdm}(m=m_\rho) = \frac{\pi\Gamma_\rho}{2} 1.15 \int_{m=715}^{m=815} \frac{d^2\sigma}{dtdm} dm \quad \text{(IV.7)}$$

In particular, this latter method for finding the amplitude $A(m_\rho)$ has been used for the data of Table IV.2 and IV.3.

Finally, since in the Söding model, the interference term causing the skewed rho mass shape roughly cancels in a mass interval of 100 MeV centered at the ρ^o mass (with other backgrounds of about 10%) and the same turns out to be true of the phenomenological form for all values of n(t), it is possible to relate the raw numbers of events in this mass range to the ρ^o differential cross section at all t values using Eq. (IV.7). In Table IV.3 the numbers of events found in the interval 0.715-0.815 GeV is given for the three annihilation energy settings, omitting the forward t bin where scanning losses occur. The values of $d\sigma/dt$ are obtained as explained above, by increasing the mean of $d^2\sigma/dtdm$ for the mass interval by 1.15 to obtain the value at the rho mass, and them multiplying by $\pi \Gamma_\rho/2$, with Γ_ρ taken as 130 MeV. These values determine the standard forward cross sections and slopes as discussed below.

The slopes, the forward differential cross section $d\sigma/dt(t=0)$ and the forward double differential cross section $d^2\sigma/dtdm(t=0)$ derived by the standard method for the central part of the rho ($0.715 < m < 0.815$ GeV) are given in Table IV.2. The slopes were derived from the measured average-t which, for an exponential distribution Ae^{Bt} is given by:

$$<|t|> = \frac{(|t_1| + 1/B)e^{-B|t_1|} - (|t_2| + 1/B)e^{-B|t_2|}}{e^{-B|t_1|} - e^{-B|t_2|}} \qquad \text{(IV.8)}$$

where $<t>$ was determined for events with $|t_1| < |t| < |t_2|$. It can be shown that this procedure is identical to the maximum likelihood solution for the slope. The slope B for events in a certain dipion mass interval was thus determined by a numerical solution of (IV.8) where $<t>$ is the average

TABLE IV.3

Event distribution for the reaction $\gamma p \rightarrow p\pi^+\pi^-$ in the mass range $M(\pi^+\pi^-) = 0.715 - 0.815$ GeV. The corresponding cross sections are from the "Standard" method described in the text.

$t(GeV)^2$	4.3 GeV		5.25 GeV		7.5 GeV	
	Events	$\frac{d\sigma}{dt}$ ($\mu b/GeV^2$)	Events	$\frac{d\sigma}{dt}$ ($\mu b/GeV^2$)	Events	$\frac{d\sigma}{dt}$ ($\mu b/GeV^2$)
.06-.10	71	65 ± 7	52	69 ± 9	44	45 ± 6
.10-.15	60	44 ± 5	48	51 ± 7	55	44 ± 6
.15-.20	42	31 ± 4	40	43 ± 6	31	25 ± 4
.20-.30	53	19 ± 2.5	38	20 ± 3	40	16 ± 2
.30-.40	31	11 ± 2	21	11 ± 2	19	7.7 ± 1.7
.40-.80	32	2.9 ± 0.5	25	3.3 ± 0.6	18	1.8 ± 0.4

four-momentum transfer squared for that mass interval. The error on B is given by $\Delta B=(\partial B/\partial t)\Delta\langle t\rangle$ where $\partial B/\partial t$ is derived from (IV.8) and $\Delta\langle t\rangle$ is the error on the average four momentum transfer squared. For the standard approach, $d\sigma/dt(t=0)$ was taken as $d^2\sigma/dtdm\,(t=0, m=m_\rho)\,\pi\Gamma_\rho/2$, with Γ_ρ=130 MeV as above. Finally, the extrapolated values for $d^2\sigma/dtdm$ at $(t=0, m=m_\rho)$ are also given in the last column of Table IV.2. These results were obtained by assuming that the data of Table IV.3 have the ideal shape given by (IV.4) and making a simple exponential extrapolation based on that form and the number of events with $0.715<m<0.815$ GeV and $0.00<|t|<0.4$ GeV^2.

The results obtained by the three methods are summarized in Tables IV.1, 2, 3 and Fig. IV.6. The fitted ρ^o parameters and cross sections are given in Table IV.1 for all six energy intervals. The first three columns give the observed and corrected number of events as well as the total channel cross section at each energy. The fit results using the Söding and the phenomenological models are also given. Inspection of Table IV.1 indicates that there is substantial agreement between these two fitting procedures. The rho mass is around 765-770 MeV and the fitted width about 135-140 MeV. The cross section seems to drop by about 30% between 2 and 8 GeV.

In Fig. IV.6 the forward differential cross sections and slopes derived from the central part of the ρ^o as determined by the three methods discussed above are plotted (Figs. IV.6a-c) as well as the total ρ^o cross sections (Fig. IV.6d). The errors in Figs. IV.6b-d are the phenomenological errors which are similar to those of the other approaches. From Fig. IV.6 and Tables IV.1 and IV.2 it appears that all three approaches yield similar results within errors. The dipion slope at the rho region is consistent with a

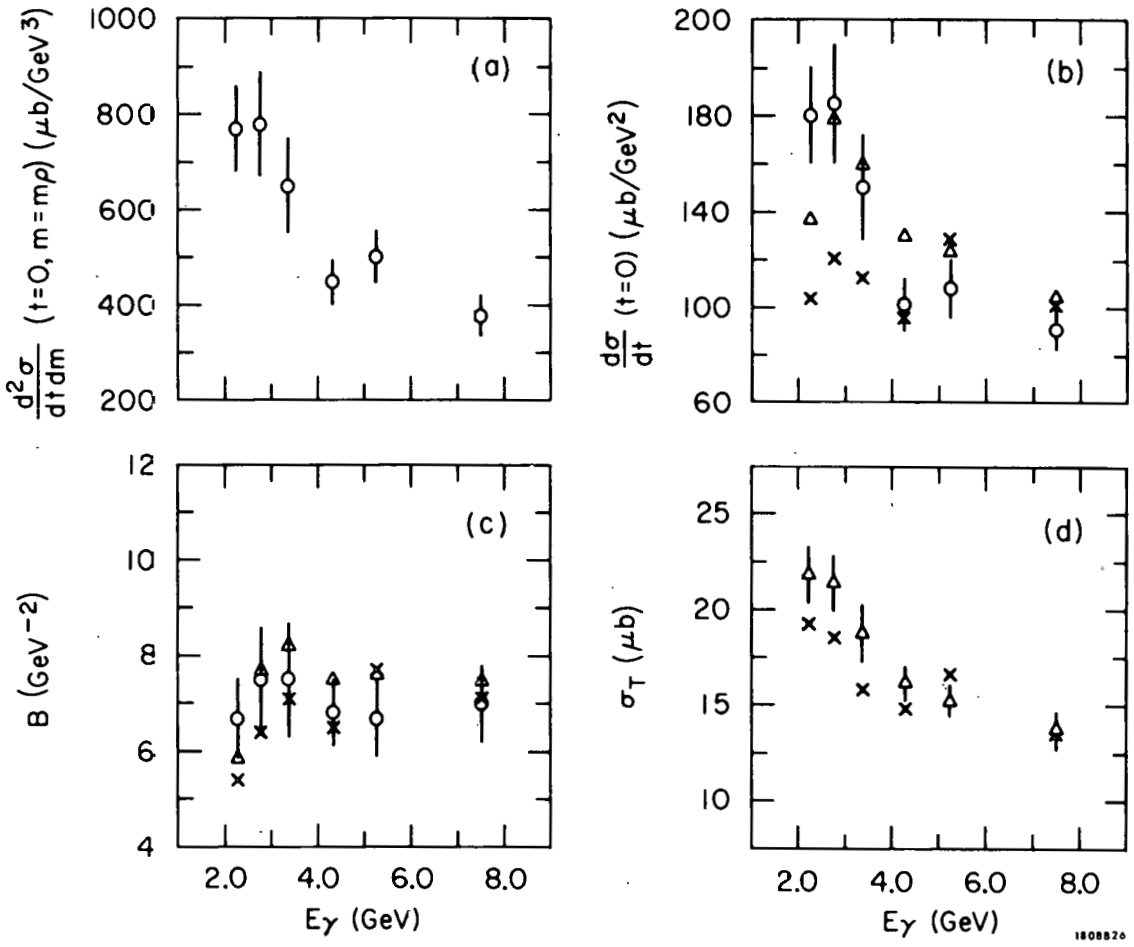

FIG. IV.6--(a) Average double differential forward cross sections near the ρ^o mass ($0.715 < m(\pi^+\pi^-) < 0.815$ GeV). (b) Forward differential cross sections (see text); (c) Slopes (see text); (d) Total ρ^o cross sections. The results for the phenomenological, Soding and standard methods are designated by triangles, crosses, and circles respectively. The errors in (a-c) are those obtained by the standard method, in (d) from the phenomenological fits.

constant slope of about 7 GeV^{-2} for $4 < E_\gamma < 8$ GeV, and similar slopes are obtained from the Söding and phenomenological fits. In this energy interval there is a slow drop of the forward cross section with energy, consistent with that observed by Alvensleben et.al.[12] However, the magnitude of our forward cross sections are significantly lower than those obtained in the counter experiments. It is important to point out here that the reaction $\gamma p \longrightarrow \rho^o p$ in the bubble chamber is essentially free of possible backgrounds from channels other than $p\pi^+\pi^-$. As will be shown in Section V.3 there is a considerable amount of $\rho^{''}$ production in the 4-body final states which might be hard to eliminate with other techniques. Also, our average slope B (Fig. IV.6c) is smaller than that observed in most counter experiments and closer to the Compton scattering slopes.[22] In this regard it must be admitted that due to the scanning losses for short range protons this experiment is not sensitive to any structure at very small t values, but our results agree well with counter measurements in the t range where both techniques are unbiased.

The results from the phenomenological model can be compared to those of other bubble chamber experiments.[10,16] Total and forward cross sections as well as the slope of the differential cross section agree at corresponding energies. The Söding model is applied here in a way slightly different from the SBT collaboration in Ref. 16. The total cross sections were fitted by equivalent methods and indeed they agree. The slope $B^{Söd}$ in the present work was fitted directly in the ρ^o matrix element, while the SBT collaboration determined it from a fit to the differential ρ^o cross sections. Thus the kinematic cut off at large $m(\pi^+\pi^-)$ and small t brings about the smaller slopes found by the SBT ($B^{Söd}$=5.9±0.3 GeV for their E=4.7 GeV data). Since the Söding model describes the data very well, our procedure

for deriving the forward Söding cross section is essentially equivalent to the standard method, using a ρ^0 width which would fit the observed dipion mass distribution. However, the Söding model fits subtract the incoherent background which is of increasing importance as E_γ decreases. Fig. IV.6b indeed shows that the values of the forward cross sections from the standard method are higher at low E_γ.

Using the method of moments, the spin-one density matrix elements have been evaluated for the dipion system in the mass interval (0.6, 0.85) GeV. As has been observed previously,[10,16] the helicity system[61] provides the simplest description of the distribution because the helicity of the photon appears to be conserved. In Fig. IV.7 the three measurable elements ρ_{00}, $\mathrm{Re}\rho_{10}$ and ρ_{1-1} in the helicity system are displayed. Backgrounds from Δ^{++} reflections and phase space were subtracted by analyzing with and without cuts and interpolating the results. For most points, and in particular the small t regions, these corrections were negligible. It is evident that the γ-ρ helicity conservation hypothesis of no spin-flip in the s-channel helicity system is valid for $|t|$ up to 0.4 GeV^2, and the data from the 7.5 GeV exposure indicate that the hypothesis may be good up to $|t| = 1.0\ \mathrm{GeV}^2$ (see Ref. 62).

B. Nucleon Resonances

In addition to the ρ^0 production discussed above, Δ^{++} production via reaction (IV.3) is observed at all energies. Fig. IV.8a shows the $M(p\pi^+)$ spectrum for the 7.5 GeV data where Δ^{++} production is obvious. Only those events with $m(\pi^+\pi^-)>1$ GeV are plotted. In black are those events for which $|t(p,p\pi^+)| < |t(p,p\pi^-)|$. If the nucleon isobar is produced by a peripheral mechanism, one would expect the smaller of these t values to be associated with it, as is clearly true for the $\Delta^{++}(1236)$. Fig. IV.8b shows the same

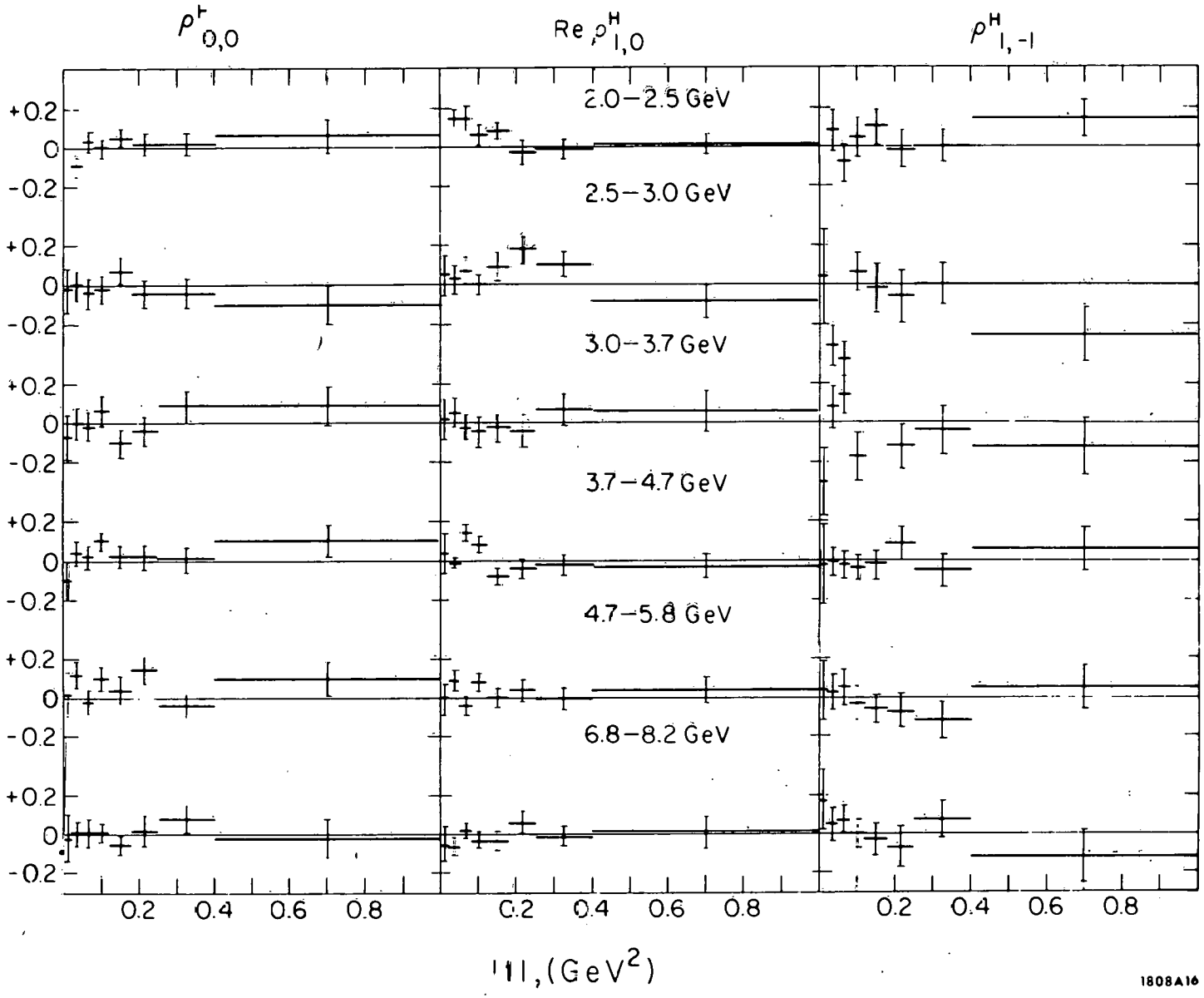

FIG. IV. 7--Spin one density matrix elements in the helicity frame for the dipion system in the ρ^0 region ($0.60 < m < 0.85$ GeV) with background subtraction.

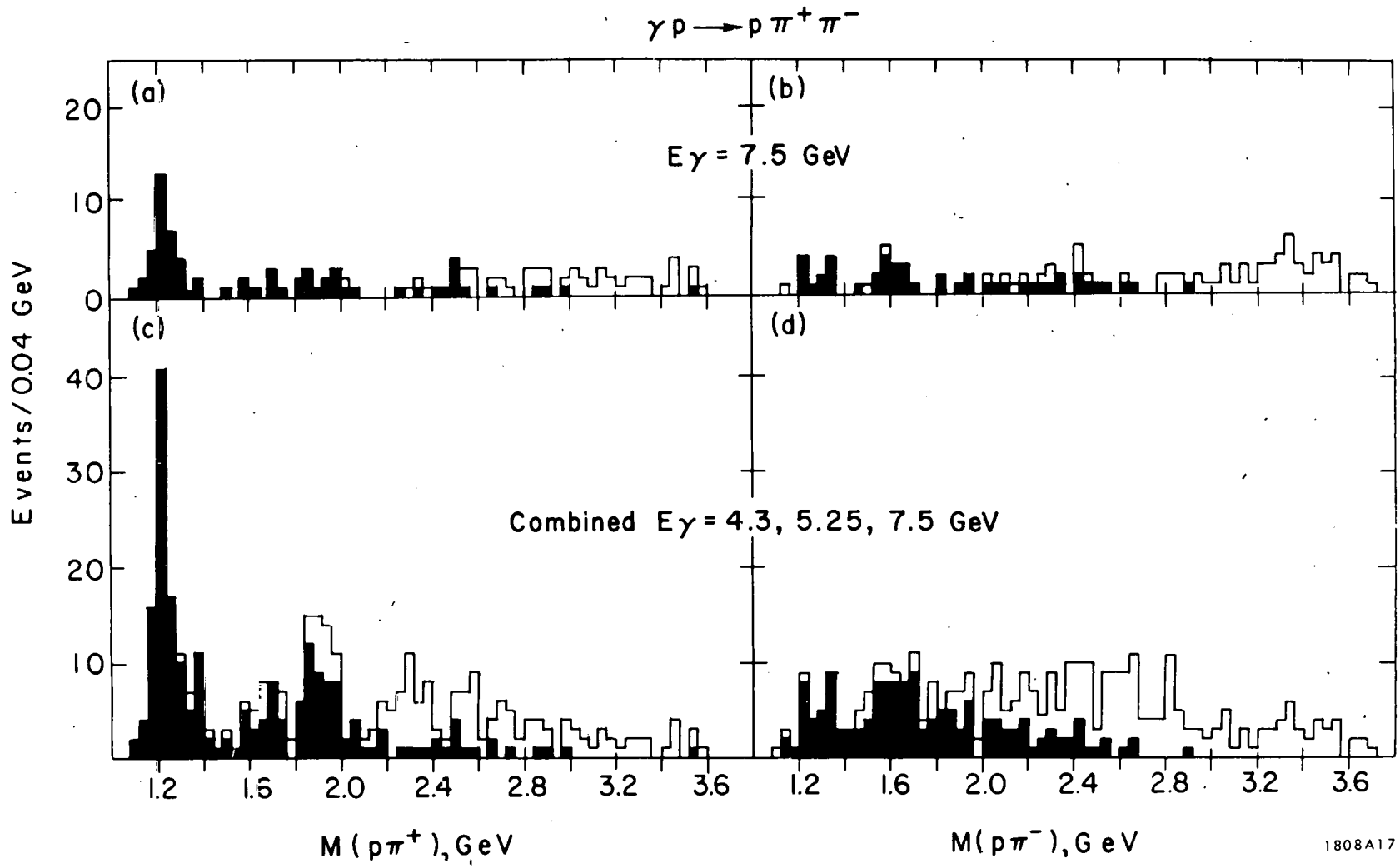

FIG. IV.8--(a) $M(p\pi^+)$ and (b) $M(p\pi^-)$ distributions for $\gamma p \longrightarrow p\pi^+\pi^-$ events with $m(\pi^+\pi^-)>1$ GeV(E=7.5 GeV). The shaded areas correspond to events with $|t(p,p\pi^+)| < |t(p,p\pi^-)|$ in (a) and to $|t(p,p\pi^-)|<|t(p,p\pi^+)|$ in (b). (c) and (d) are the same distributions as in (a) and (b) for the combined data of the 4.3, 5.25 and 7.5 GeV exposures.

thing with π^+ replaced by π^-. In Figs. IV.8c and d the combined data for the 4.3, 5.25, and 7.5 GeV regions is shown for $M(p\pi^+)$ and $M(p\pi^-)$ respectively, using only those events with $m(\pi^+\pi^-)>1$ GeV. The solidly blocked events are those with the lesser momentum transfer. Although not statistically compelling, the accumulation of events in the 1.9 GeV region for $p\pi^+$ and the 1.6 GeV region for $p\pi^-$ indicates that a substantial fraction of the events with $m(\pi^+\pi^-)>1$ GeV are probably accounted for by N^* production (e.g., by the Drell process).

In Fig. IV.9 the cross sections for $\gamma p \longrightarrow \pi^- \Delta^{++}$ at the six energies as determined from the phenomenological fits using a relativistic p-wave delta shape[59] of the form given by (IV.5a) are plotted. The energy dependence of the delta cross section is well described by $\sigma(\gamma p \longrightarrow \pi^- \Delta^{++}) \propto E_\gamma^{-a}$ with a slope $a=1.74\pm0.16$, which is close to the slope for quasi-two-body hadron collisions produced by non-strange meson exchange.[63] The use of a delta shape other than (IV.5a) may reduce the magnitude of the cross section, but will not change the slope.[29]

One would expect $\rho^J_{11}=.5$ ($\rho^J_{33}=.0$) in the Jackson system for the delta decay if delta production proceeded by pure one pion exchange (OPE). It is, however, difficult to draw decisive conclusions about the Δ^{++} production mechanism from the density matrix elements because of the small statistics involved and the reflections from the ρ^0 events. For the 7.5 GeV data, where the reflections are minimal (see Fig. IV.2), the matrix element for events with $|t(p,p\pi^+)| < 0.4$ GeV^2 is $\rho^J_{11}=0.21\pm0.10$ which probably indicates a mechanism other than pure OPE.

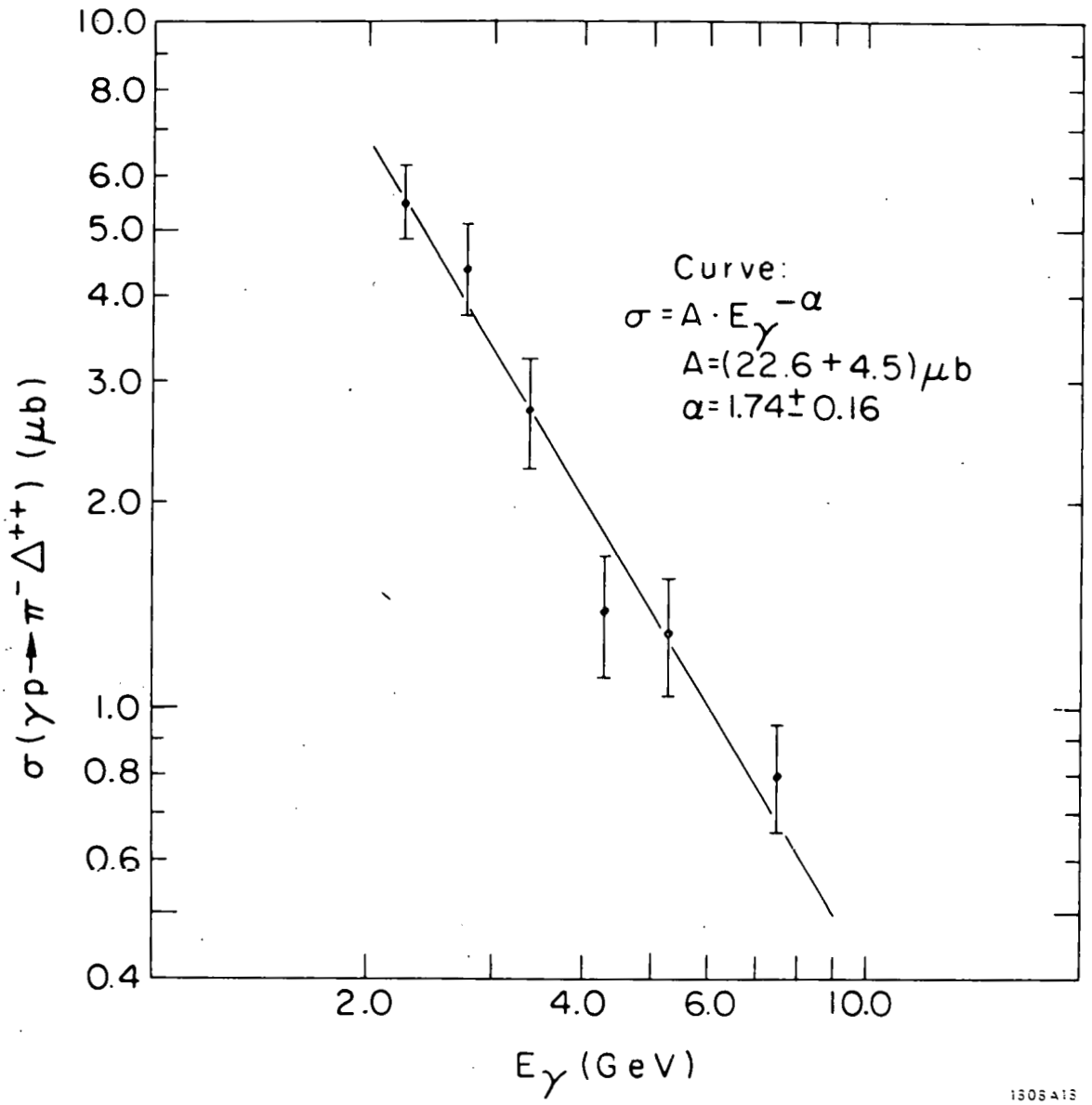

FIG. IV.9-- Cross sections for $\gamma p \longrightarrow \Delta^{++}\pi^-$ as obtained with a fit to a relativistic p-wave Breit-Wigner for the delta. The solid line represents the best fit to the form $A\ E_\gamma^{-a}$.

C. Higher Mass Vector Meson Production (ρ')

Vector mesons with square of their mass forming a series with interval about 1 GeV are predicted by the Veneziano model,[15] with uncertain decay width, but presumably allowed to decay to two pions. Also, some discrepancies between VDM and experimental data could be reconciled by the existence of higher mass vector mesons (see section IV.3). No evidence for such states is to be found in the spectra of Fig. IV.1-2. For the 7.5 GeV data the number of events with $m(\pi^+\pi^-) > 1$ GeV turns out to be especially small. Furthermore, as was shown in the last paragraph, a large number of the events appear to correspond to πN interactions. In Fig. IV.10 (a-b) the angular distribution of the π^+ in the dipion helicity system is plotted for the two $t'(\gamma, \pi\pi)$ intervals ($t'=t-t_{min}$, where t_{min} is the minimum momentum transfer for the given mass). The shaded events represent the Δ^{++} events. If the ρ' were diffractively produced in a center-of-mass helicity-conserving interaction ($\sin^2\theta_\pi^H$ distribution), then one would expect most of the ρ' events to occur with $|\cos\theta_\pi^H| < 0.5$, i.e., with $N(|\cos\theta_\pi^H| < 0.5)/N(\text{all}) = 11/16$. Fig. IV.10c shows the dipion mass distribution for events with $|\cos\theta_\pi^H| < 0.5$. The shaded areas correspond to events with momentum transfer squared to the dipion system less than 0.4 GeV^2. These events with $|\cos\theta_\pi^H| < 0.5$ and $t' < 0.4$ GeV^2 correspond to 1 event/(0.1 GeV) in the 1650 MeV region and 4 events/(0.1 GeV) in the 1250 MeV region, indicating with 90% confidence level that $\sigma_\rho(1600) < 0.1\ \mu b$ and $\sigma_\rho(1250) < 0.3\ \mu b$ per 100 MeV width of such resonances.

IV.2 Omega Meson Production

The analysis of the reaction

$$\gamma p \longrightarrow \omega p \qquad \text{(IV.9)}$$

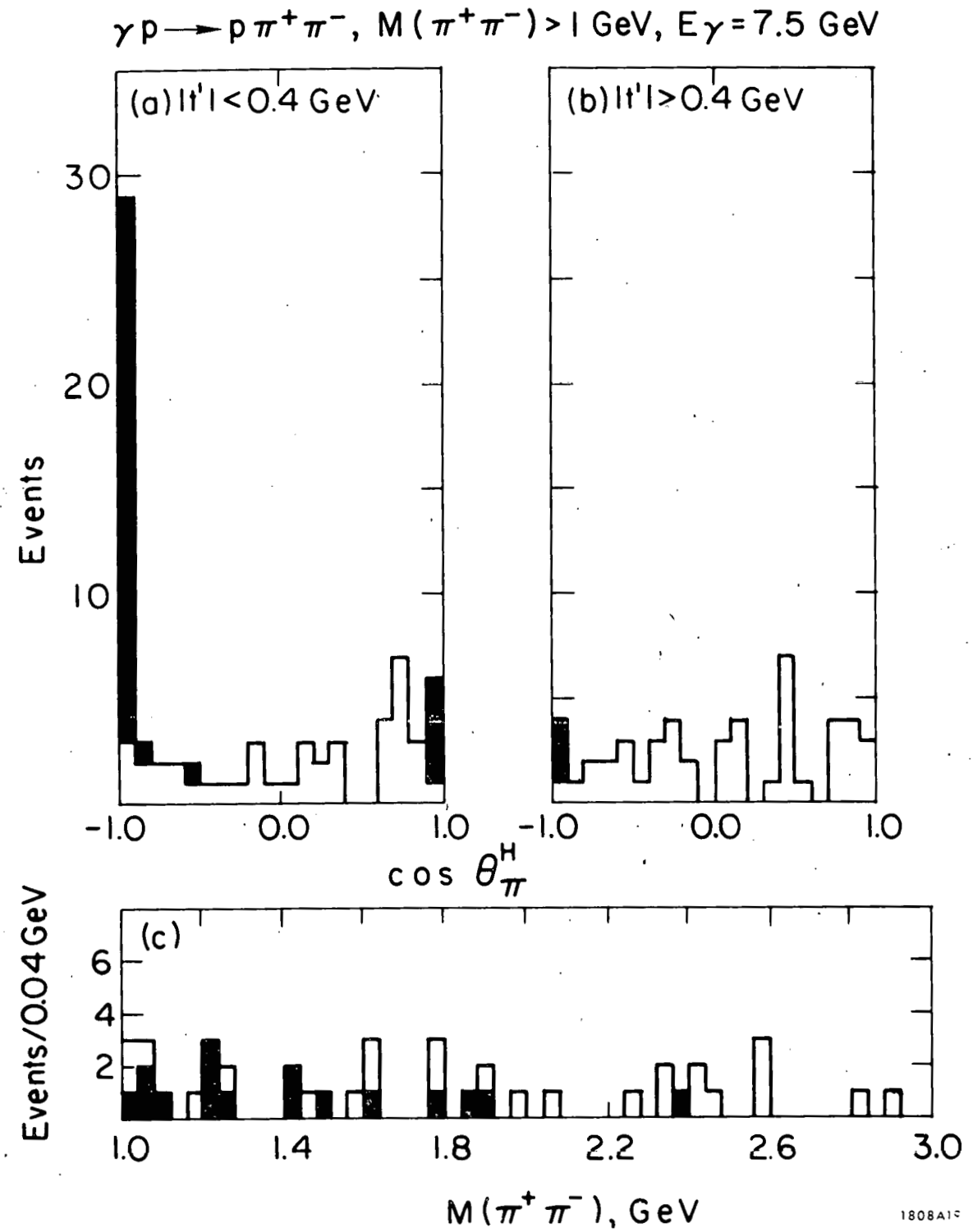

FIG. IV.10--(a), (b) Angular distributions of the π^+ in the helicity frame of the dipion system for events with $m(\pi^+\pi^-) > 1$ GeV for the 7.5 GeV data. Shaded area represents delta events. (c) Dipion mass distributions for those events with $|\cos\theta^H_\pi| < 0.5$. The shaded area represents events with $|t(\gamma, \pi\pi)| < 0.4$ GeV^2.

is more complicated than that of ρ^o photoproduction because the channel $p\pi^+\pi^-\pi^o$ is much more complex and difficult to analyze than the 3-body channel discussed above. In addition to the contamination by multi-neutral particle events and to complications due to the presence of bremsstrahlung events, this channel does not have a single resonance saturating the channel as the rho does in the $p\pi^+\pi^-$ final state. Not only is a prominent omega signal observed, accounting for about 15% of the events in this channel, but also significant production of the final states $\Delta^{++}\rho^-$ and $p\pi^o\rho^o$ is observed. The discussion of the cross section determination for the 1-C channels in section III.4 has given some indication of the contamination of the annihilation one pi-zero events by events of other channels and has determined a missing mass cut which optimizes the signal to noise ratio by removing most of the contaminating events.

Although omega production necessarily leads to a neutral particle in the final state, the narrow width of the ω meson makes the signal detectable over relatively large backgrounds. It has therefore been possible to determine omega cross sections for events induced by both annihilation and bremsstrahlung photons. Fig. IV.11 shows the $\pi^+\pi^-\pi^o$ invariant mass distributions for fits where track ionization is consistent with the reaction

$$\gamma p \longrightarrow p\pi^+\pi^-(mm)^o \qquad \text{(IV.10)}$$

for eight intervals of the reconstructed photon energy E_γ. In the three higher energy intervals, reaction (IV.10) is identified by a 1-C fit to the annihilation photon energy, with the missing mass cut determined in section III.4 and a cut on confidence level >0.005. The restriction to 1-C fits satisfying the

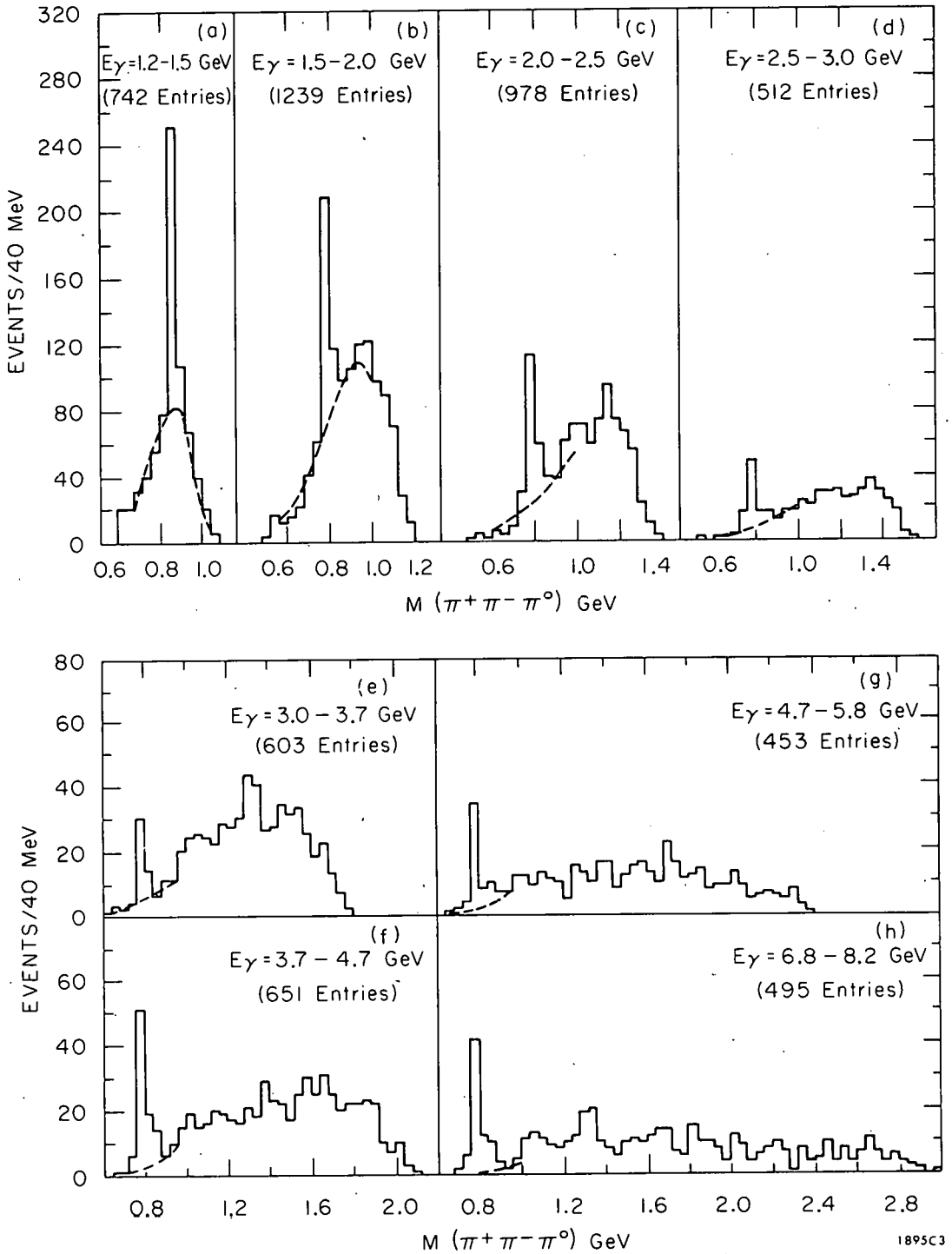

FIG. IV.11--$\pi^+\pi^-\pi^o$ invariant mass distributions for $\gamma p \longrightarrow p\pi^+\pi^-\pi^o$ with photon energies in the range of 1.2-8.2 GeV. Dashed lines indicate the phase space background assumed.

missing mass and probability cuts removes most of the multi-neutral and bremsstrahlung background. Although no such cuts are possible for the 0-C fits to events in the bremsstrahlung region, in every case the ω signal is clearly identifiable over background, increasingly so at higher energies.

In order to determine the ω cross-sections several corrections had to be considered: (a) loss of events with a short (invisible) proton; (b) contamination of the data by events not belonging to the channel $p\pi^+\pi^-\pi^o$, mainly events in which more than one π^o was produced and which nevertheless gave a good 1-C fit or a 0-C reconstruction at lower E_γ according to Eq. III.6; (c) contamination of the data by events of reaction (IV.10) produced by photons outside each selected energy band, which gave acceptable 1-C or 0-C fit with E_γ inside the selected energy band; (d) loss of omega events because of the cuts in the 3-pion mass spectrum introduced to define an omega event or because of the cuts used to eliminate background reactions. These cuts were (i) $0.68<m(\pi^+\pi^-\pi^o)<0.88$ GeV (ω-cut), (ii) $P(\chi^2)>0.005$ (probability cut) and (iii) $0.18<MM^2<0.10$ GeV^2 (missing mass squared cut). Since correction (a) is essentially a scanning loss, it can be best estimated by using our more abundant reaction, $\gamma p \longrightarrow \rho^o p$. It turned out to be negligible for E<3 GeV, and 10-14% in the energy range 3-8 GeV. For the study of corrections (b)-(d) the track and event simulation program PHONY has been used. Both $p\omega$ and phase-space events were generated and subjected to the same geometry-kinematics fitting and cuts as the real events. Study of the fake events has indicated that for the annihilation (1-C) events imposing the missing-mass cut ($-0.18<MM^2<0.10$ GeV^2) did not affect real ω events significantly whereas contamination (b) above is almost entirely removed (effects (c) and (d) resulted in a long low level tail on the expected ω

mass distribution). The net corrections amounted to about 10% and thus even approximate knowledge of them should give a good final cross-section. For the five lower energy intervals the increased uncertainty from the 0-C nature of the fit was generally countered by the better measuring accuracy. The overall corrections for effects (a)-(d) are specified in Table IV.4 and for all energy intervals they are smaller than the statistical accuracy of the data. A further correction of 10% was applied to account for the neutral ω decay modes which are not visible in the bubble chamber.

Previous experiments[9,10] have shown that the cross section for omega photoproduction decreases significantly with increased photon energy, a behavior indicative of a substantial contribution from the one-pion exchange (OPE) process (which has a cross section[63] approximately proportional to E_γ^{-2}). The data at high energy flatten out, indicating in addition a nearly constant cross section from a diffractive process. This work has extended the upper range of photon energy to 8.2 GeV, as well as making independent measurements in the energy range 1.2-8.2 GeV. The energy dependence of the cross-section is shown in Fig. IV.12. In Fig. IV.12a our results are presented together with the recent data at 2.8 and 4.7 GeV from the polarized-photon (laser) experiment at SLAC. A more comprehensive compilation of cross-sections for reaction (IV.9) is given in Fig. IV.12b.

From SU(3) it is expected[19] that the $\omega\pi\gamma$ coupling should be much larger than the $\rho\pi\gamma$ in the ratio 9:1. Thus one-pion exchange can contribute more to reaction (IV.9) than to ρ^o production and in fact be a substantial part. A fit has been made to the data of Fig. IV.12a (for E>2.0 GeV) by a curve of the type

$$\sigma(\gamma p \longrightarrow \omega p) = C_{OPE} E_\gamma^{-\alpha 1} + C_{DIFF} E_\gamma^{-\alpha 2} \qquad \text{(IV.11)}$$

TAELE IV.4

Number of observed events, corrected ω events, ω total cross sections and monochromatic total channel cross sections as a function of the incoming photon energy.

E_γ(GeV)	Events[a] Observed	No. of ω^o Events		$\sigma_T(\omega)$[c] (μb)	Total Channel Cross Sections (μb)
		Observed	Corrected		
1.2 - 1.5	742	220	235	6.9 ± 1.4	---
1.5 - 2.0	1239	180	194	6.7 ± 1.2	---
2.0 - 2.5	978	141	150	6.9 ± 1.5	---
2.5 - 3.0	512	66	75	6.2 ± 0.9	---
3.0 - 3.7	603	34	36[b]	2.8 ± 0.7	---
3.7 - 4.7	631	81	95[b]	2.9 ± 0.4	18.2 ± 2.0
4.7 - 5.8	430	52	57[b]	2.3 ± 0.4	13.5 ± 1.5
6.8 - 8.2	464	68	73[b]	2.0 ± 0.3	11.8 ± 1.2

(a) Unique 0C events for the bremsstrahlung data (1.2 - 3.7 GeV) and events surviving the missing mass ($-.18 < MM^2 < .10$ GeV^2) and probability ($P(X^2) \geq .005$) cuts for the 1C data (3.7 - 8.2 GeV).

(b) Including 10 - 13% forward scanning loss correction.

(c) Including ω neutral[6] decay modes (10% correction).

where E_γ is the photon laboratory energy in GeV. It has been assumed that the energy dependence of the OPE and diffractive contributions can be approximated by a power law. α_1 is expected[63] to be in the range 1.5-2.5, and α_2 should be small since the diffraction cross-section does not depend strongly on E_γ. The data are not sufficiently accurate for a good determination of all 4 parameters appearing in Eq. (IV.11). Hence, an energy dependence is assumed for the OPE part (α_1=2.) with constant diffractive term (α_2=0.). These values yield $C_{OPE}=(31.\pm5.)\,\mu b$ and $C_{DIFF}=(1.5\pm.3)\,\mu b$. The full curve on Fig. IV.12 represents the omega cross-sections calculated with Eq. (IV.11) using these values. A similar fit over a more restricted energy range (E =2.0-5.8 GeV), and with fixed $\alpha_1(1.6)$ and $\alpha_2(0.08)$ was attempted in Ref. 10 yielding $C_{OPE}=(18.4\pm5.8)\,\mu b$, $C_{DIFF}=(1.9\pm0.9)\,\mu b$. Ideally one would hope to detect terms proportional to E_γ^{-1} and $E_\gamma^{-0.5}$, to account for possible A_2 and f exchanges[65] and their interference with the diffractive (Pomeron) amplitude, but since the present data are insufficient, such terms are assumed to be small.

The parameterization (IV.11) determines independently the diffractive (natural) and OPE (unnatural parity exchange) contributions to the ω cross-sections at all energies. Thus, with some plausible assumptions about the two processes, the differential cross-sections and the density matrix elements for reaction (IV.9) can be calculated and compared with experiment. The calculated OPE contribution to the cross-section determined by the parameters above is shown as a function of the photon energy by the dashed line in Fig. IV.12a. For comparison, the unnatural exchange cross-sections for ω production at 2.8 and 4.7 GeV as determined recently in the polarized

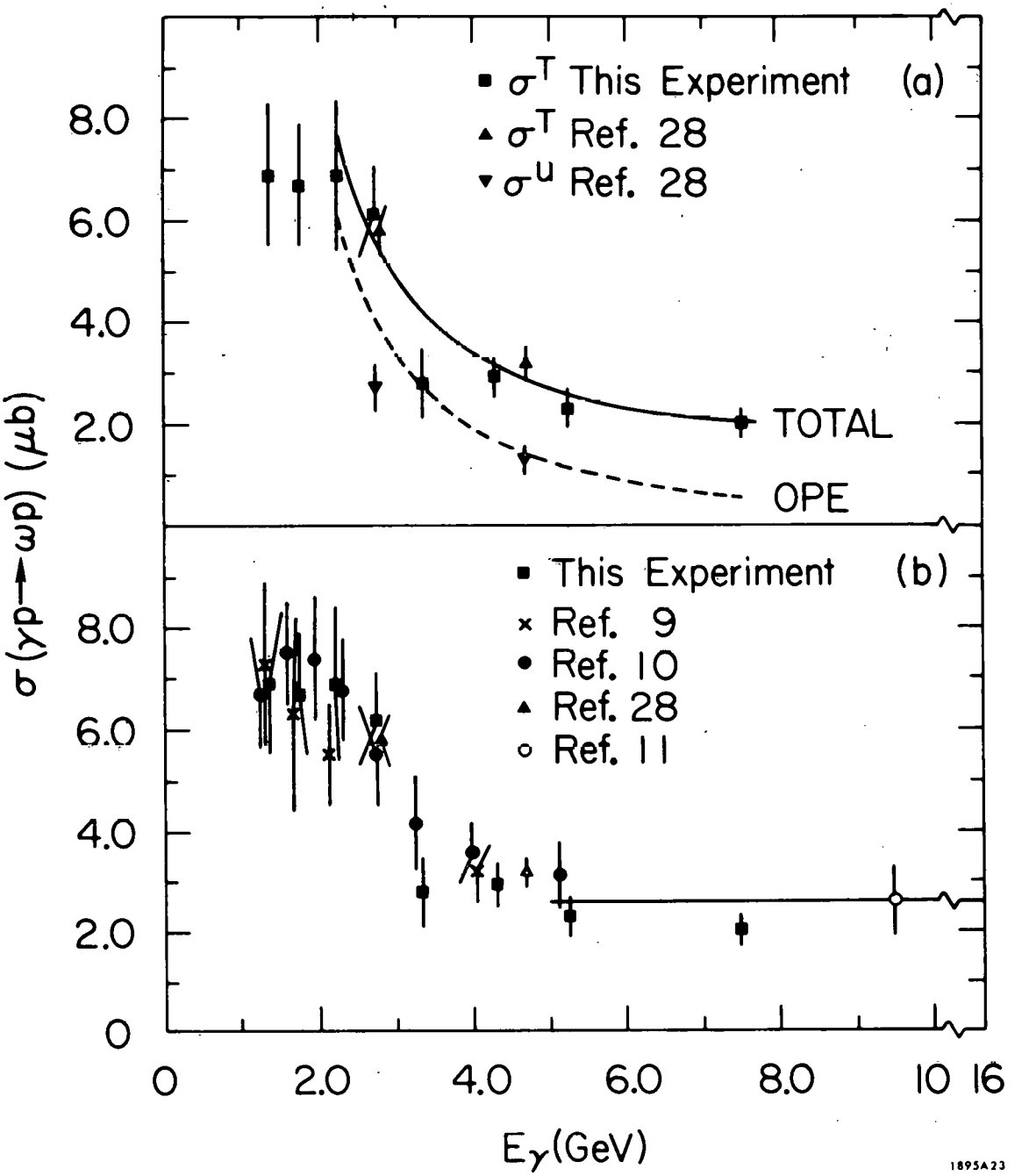

FIG. IV.12--(a) $\gamma p \longrightarrow \omega p$ total cross sections measured in this experiment and in Ref. 28. σ^u is the unnatural parity exchange cross sections for $|t| \leq 1.0$ GeV^2 at 2.8 and 4.7 GeV. (Ref. 28). The curves are best fits to Eq. (IV.11) for $\alpha_1 = 2.0$ and $\alpha_2 = 0$ (see text). (b) Compilation of $\gamma p \longrightarrow \omega p$ cross sections (Refs. 9,10, 11,28 and this experiment).

photon experiment are plotted. The agreement between the calculated and observed cross sections is good.

The observed differential cross section $d\sigma/dt$ for photon energies above 2.0 GeV is shown in Fig. IV.13 (a-f). The curves, which agree reasonably well with the data, have been calculated as follows. Since the diffractive part of the amplitude in the forward direction is purely imaginary and the OPE part is assumed real, the amplitudes do not interfere and the cross section may be written:

$$\frac{d\sigma}{dt} = \frac{d\sigma^{OPE}}{dt} + \frac{d\sigma^{DIFF}}{dt} \quad . \tag{IV.12}$$

The OPE part of the cross-section was calculated with final state absorption corrections, using a sharp cut off absorption model[66] with a radius of R=0.8 Fermi and $\Gamma(\omega\pi\gamma)=1.2$ MeV. The diffractive part of the cross section can be written:

$$\frac{d\sigma^{DIFF}}{dt} = A(\gamma p \longrightarrow \omega^{DIFF}p)e^{Bt} \tag{IV.13a}$$

with $B=(7.0\pm0.4)$ GeV^{-2}, which is the average value for the ρ^o slope obtained in the previous section. This also agrees with the value of $B=7.5\pm1.5$ GeV^{-2} for omega photoproduction by natural parity exchange at 4.7 GeV obtained in the SLAC polarized photon experiment.[28] Since the asymptotic omega cross-section (the diffractive part) obtained above is $1.5\pm0.3\,\mu$b, the forward cross section becomes:

$$A(\gamma p \longrightarrow \omega(DIFF)p) = \sigma_{\omega}(DIFF)\cdot B=10.5\pm2.1\mu b/GeV^2 \quad . \tag{IV.13b}$$

This value together with the corresponding forward ρ^o cross-sections, will be used in section IV.3 to derive the direct VDM couplings of photons to

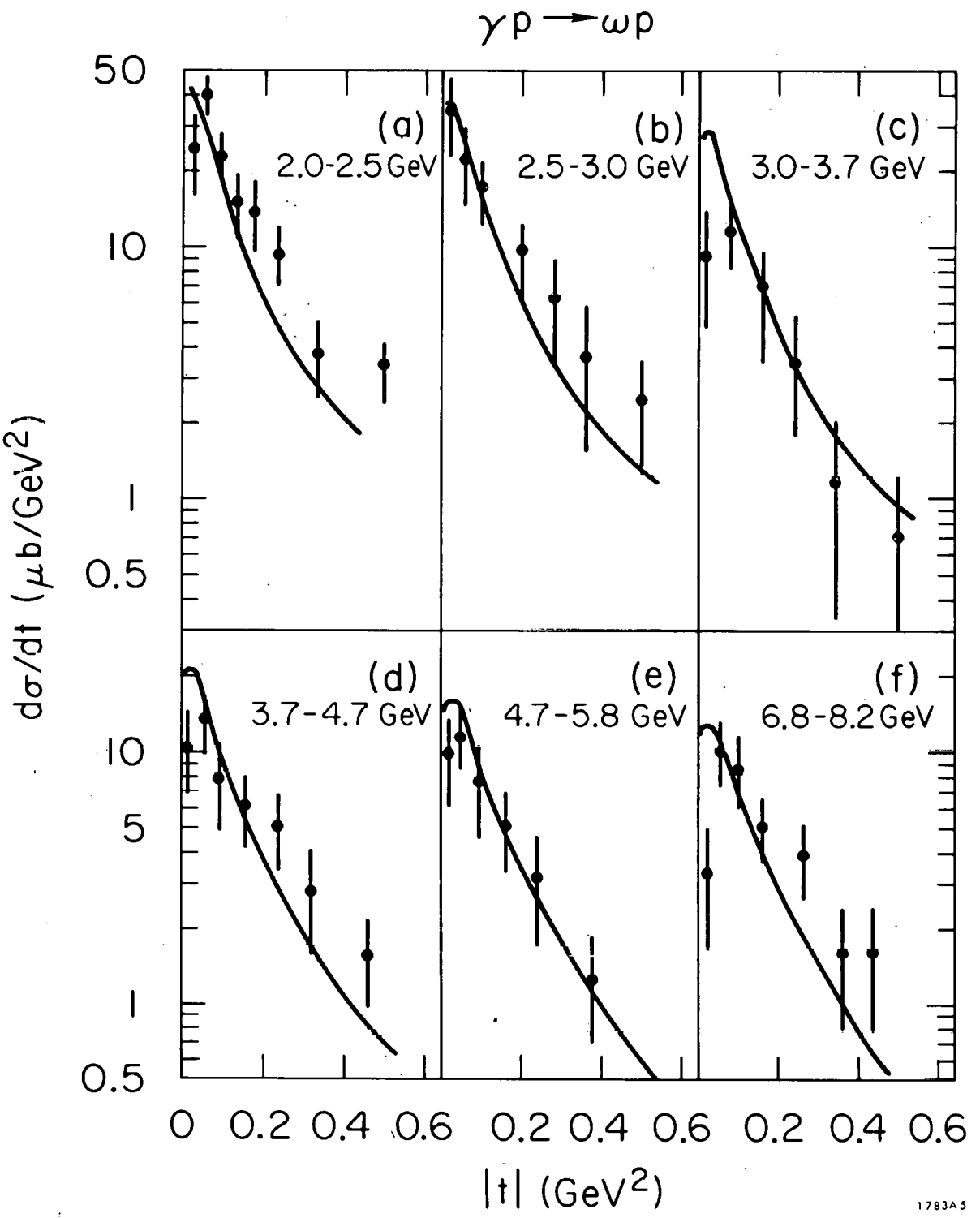

FIG. IV. 13--Differential cross sections $d\sigma/dt$ for the reaction $\gamma p \longrightarrow \omega p$ with photon energies above 2 GeV. The curves are the calculated cross sections (see text).

vector mesons as well as for comparisons of these cross-sections with results from Compton Scattering.

Finally, the omega decay density matrix elements ρ^H_{00}, $\mathrm{Re}\rho^H_{10}$ and ρ^H_{1-1} in the helicity frame were calculated using the relation:

$$\rho_{ij}(t) = \frac{\frac{d\sigma^{OPE}}{dt}\,\rho^{OPE}_{ij}(t) + \frac{d\sigma^{DIFF}}{dt}\,\rho^{DIFF}_{ij}(t)}{\frac{d\sigma}{dt}}$$

The diffractive part of the cross-section has been assumed to be helicity conserving and thus gives $\rho^{DIFF}_{00} = \rho^{DIFF}_{1-1} = \mathrm{Re}\rho^{DIFF}_{10} = 0$ in the helicity frame. The OPE density matrix was calculated with the sharp cutoff model mentioned above. The final results of the calculations as well as our experimental results are shown in Fig. IV.14. Again fair agreement between theory and experiment obtains.

IV.3 Vector Dominance Model Tests and the Photon-Vector Meson Couplings

In the preceding sections differential cross sections for the reaction $\gamma p \longrightarrow \rho^o p$ have been obtained, and a simple model has been used to extract the constant, and hence presumably diffractive, part of the omega cross section. Assuming the same slopes for rho and omega production, the omega diffractive forward differential cross section has been deduced. Since one of the defining characteristics of diffractive production is its asyptotic behavior, the most valid comparison of the rho and omega cross sections in the forward direction will be that made at our highest energy, 7.5 GeV. At this energy the values obtained are $A(\gamma p \longrightarrow \rho^o p) = 99 \pm 12 \mu b/\mathrm{GeV}^2$ (averaging the three methods in Table IV.2) and $A(\gamma p \longrightarrow \omega p) = 10.5 \pm 2.1 \mu b/\mathrm{GeV}^2$, yielding a

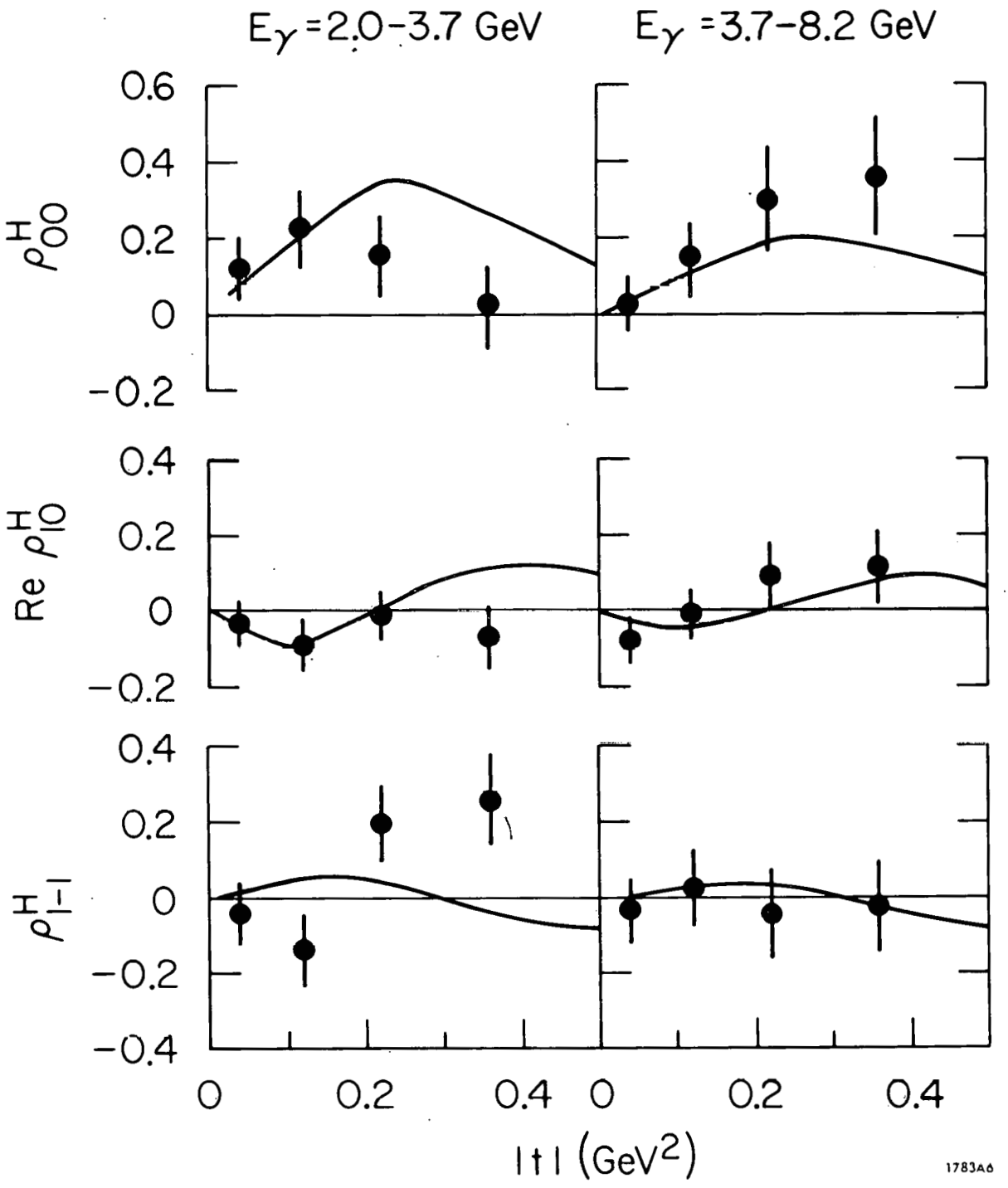

FIG. IV. 14--The spin density matrix elements ρ_{00}, Re_{10} and ρ_{1-1} in the helicity system for the reaction $\gamma p \longrightarrow \omega p$. The curves are the matrix elements calculated with the OPE model discussed in the text.

forward cross section ratio of

$$\frac{A(\gamma - \rho^o)}{A(\gamma - \omega)} = \frac{99 \pm 12}{10.5 \pm 2.1} = 9.4 \pm 2.0 \quad . \tag{IV.14}$$

It follows from VDM that this ratio should be the ratio of the photon-vector meson coupling constants.

Within the framework of VDM the diffractive part of the vector meson photoproduction can be written in terms of vector meson elastic scattering as

$$\frac{d\sigma}{dt}(\gamma p \longrightarrow V^o p) = g^2_{\gamma V} \frac{d\sigma}{dt}(V^o p \longrightarrow V^o p) \tag{IV.15}$$

where $g^2_{\gamma V}$ is given in terms of the vector coupling constant by

$$g^2_{\gamma V} = \frac{\alpha}{4} \left[\frac{\gamma^2_V}{4\pi}\right]^{-1} \quad . \tag{IV.16}$$

In general, the optical theorem can be written as the following relation between the total cross section and the spin averaged forward cross section for elastic scattering:

$$\frac{\sigma_T^2}{16\pi} = \frac{1}{1+\eta^2} \frac{d\sigma}{dt}(t=0) \tag{IV.17}$$

where η is the ratio of the real and imaginary parts of the forward scattering amplitude (i.e., $\eta = 0$ implies a completely imaginary amplitude at $\theta = 0^o$). When combined with Eq. (IV.15), the optical theorem becomes:

$$\sigma_T(V^o p) = \frac{64\pi}{\alpha} \frac{1}{1+\eta^2_{V^o}} \left[\frac{\gamma^2_{V^o}}{4\pi}\right] \frac{d\sigma}{dt}(\gamma p \longrightarrow V^o p)\Big|_{t=0} \tag{IV.18}$$

where V^o is any vector meson. Assuming equal total cross sections for the neutral rho and omega meson, as the quark model predicts,[49] Eq. (IV.18) gives a relation between γ^2_ρ, γ^2_ω, η^2_V and the forward cross section ratio IV.14.

Neglecting the real parts, the squares of which are known to be small,[67] the ratio of $g^2_{\gamma\rho}$ to $g^2_{\gamma\omega}$ is given by the ratio (IV.14) of forward cross sections:

$$\frac{g^2_{\gamma\rho}}{g^2_{\gamma\omega}} = \frac{\gamma^2_\omega}{\gamma^2_\rho} = \frac{A(\gamma - \rho^o)}{A(\gamma - \omega)} = 9.4 \pm 2.0 \,. \qquad \text{(IV.19)}$$

This agrees reasonably well with the colliding beam result which finds[13] $g^2_{\gamma\rho}/g^2_{\gamma\omega} = 7.5 \pm 1.5$. It is also very close to the most simple SU(3) treatments[19] which predict that this ratio should be 9:1.

Furthermore, VDM can also be used to expand the amplitude for Compton scattering in terms of the amplitudes for vector meson photoproduction:

$$a(\gamma p \longrightarrow \gamma p) = \sum_{V^o} g_{\gamma V^o}\ a(\gamma p \longrightarrow V^o p) \,. \qquad (V^o = \rho^o, \omega, \phi) \qquad \text{(IV.20)}$$

Using this expansion, the optical theorem, and writing $a(0) = i\sqrt{d\sigma/dt}\,/(1+\eta^2)$ the following relation between the total photoabsorption cross section and the imaginary (diffractive) part of the forward cross section for the photoproduction of vector mesons results

$$\sigma_T(\gamma p) = \left(\frac{\gamma^2_{\rho,\mathrm{eff}}}{4\pi}\right)^{-1/2} \sum_{V^o} \left\{ \frac{4\pi\alpha}{1+\eta^2_V} \left(\frac{\gamma_\rho}{\gamma_V}\right)^2 \frac{d\sigma}{dt}(\gamma p \longrightarrow V^o_t p)^{\mathrm{DIFF}}_{t=0} \right\}^{1/2} \qquad \text{(IV.21)}$$

Using the recent measurements[21] of $\sigma_T(\gamma p)$, this relation, together with the ratio of γ^2_ρ and γ^2_ω given by (IV.19), as well as assumptions on the magnitudes of γ^2_ϕ and η^2_V (η^2_V is estimated[67] to be about 0.04), determines a value for $\gamma^2_\rho/4\pi$.

Our experimental values for the right hand side of Eq. (IV.21) are given in Fig. IV.15, with $\gamma^2_\rho/4\pi$ adjusted for best agreement with the total

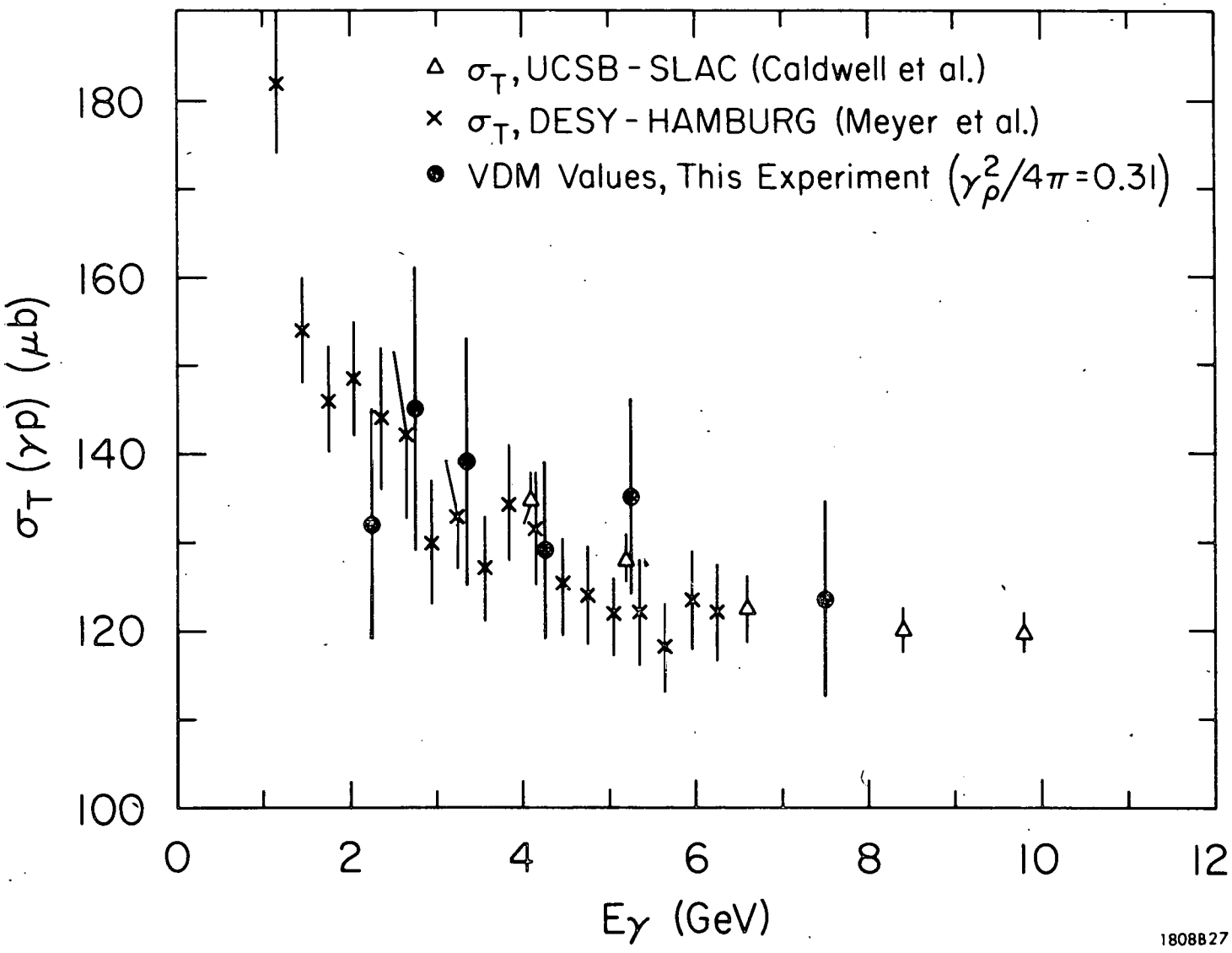

FIG. IV. 15--Comparison of measured γp total cross sections of Ref. 21, with VDM predictions based upon the present data using $\gamma_\rho^2/4\pi = 0.32$ (see text).

cross section measurements[21] also shown. The s dependence of both processes is seen to be similar, indicating that the coupling constants are essentially energy independent. The average of the Söding and phenomenological forward cross sections from Table IV.2 has been used since they both subtract the incoherent background which becomes more prominent at lower energies. The magnitudes of the omega and phi diffractive cross sections have been taken from section IV.2 and from Anderson et al.,[12] respectively, while the ratios of the couplings have been obtained from Eq. (IV.19) and Anderson et al. The best agreement is obtained for $\gamma_\rho^2/4\pi = 0.32 \pm 0.03$ (and not 0.50 as obtained in the storage ring experiments). A similar comparison made on 4.3 GeV γd data found the value $\gamma_\rho^2/4\pi = 0.28 \pm 0.04$. It is interesting to note that our experiment evaluated the total photoproduction cross section (see Ref. 1) at 7.5 GeV, obtaining a result precisely in agreement with the more complete experiment described in Ref. 21. This gives us confidence that no systematic problem is introduced by using the results of two different experiments in relation (IV.21) to obtain the best value of $\gamma_\rho^2/4\pi$. We thus conclude that photoproduction experiments in both hydrogen and deuterium in the energy range 3-8 GeV require a coupling constant of about 0.3 when compared with $\sigma_T(\gamma p)$ via relation (IV.21).

The recently reported direct measurements of Compton scattering cross sections[22] allow a further test of the VDM idea, which avoids the uncertainty of the extrapolation to t=0 for the ρ^o data and the assumption of a small real part in Compton scattering. In the approximation that the amplitudes (IV.20) all have the same phase (e.g., all imaginary) and have the same spin structure at all t values, one obtains the following relation between

Compton scattering and photoproduction:

$$\frac{d\sigma}{dt}(\gamma p \longrightarrow \gamma p) = \frac{\alpha}{4}\left(\frac{\gamma^2_{\rho,\mathrm{eff}}}{4\pi}\right)^{-1} \sum_{V^o}\left\{\frac{\gamma_\rho}{\gamma_V}\left[\frac{d\sigma}{dt}(\gamma p \longrightarrow V^o_t p)\right]^{1/2}\right\}^2 \quad \text{(IV.22)}$$

In the general case when the phases can differ VDM would require the left hand side of Eq. (IV.22) to be less than or equal to the right hand side (the rho appears to be transverse from the density matrix elements of Fig. IV.7). Fig. IV.16 shows our results for the right hand side of Eq. (IV.22), using the above value of $\gamma^2_\rho/4\pi$. The standard values in Table IV.3 (which are the raw data obtained from the number of dipion pairs with mass in the interval 0.715-0.815 GeV, where the Söding interference term is expected to cancel) have been used for the rho term, with the omega and phi terms estimated as explained above. Also shown are the directly measured Compton scattering cross sections on hydrogen.[22] The lines in Fig. IV.16 correspond to the ρ^o standard slopes from Table IV.2 and are normalized in the forward direction to the sum of the ρ^o standard cross section plus the omega and phi diffractive forward cross sections as in (IV.21). Thus the curves represent our best estimate for the right hand side of (IV.22) assuming only diffractive contributions. Excellent agreement between the photoproduction data and Compton scattering (via the VDM equation (IV.22)) is obtained at all values of s and t where data on both reactions is available.

Because the forward cross section has already been used in Eq. (IV.21) to determine the coupling constant, the real meaning of the agreement observed in Fig. IV.16 is that the slope that we observe in photoproduction (an average of 7.0 ± 0.4 GeV^{-2}) is in agreement with Compton scattering. This is a somewhat different conclusion than that reached in Ref. 22, since the slope they

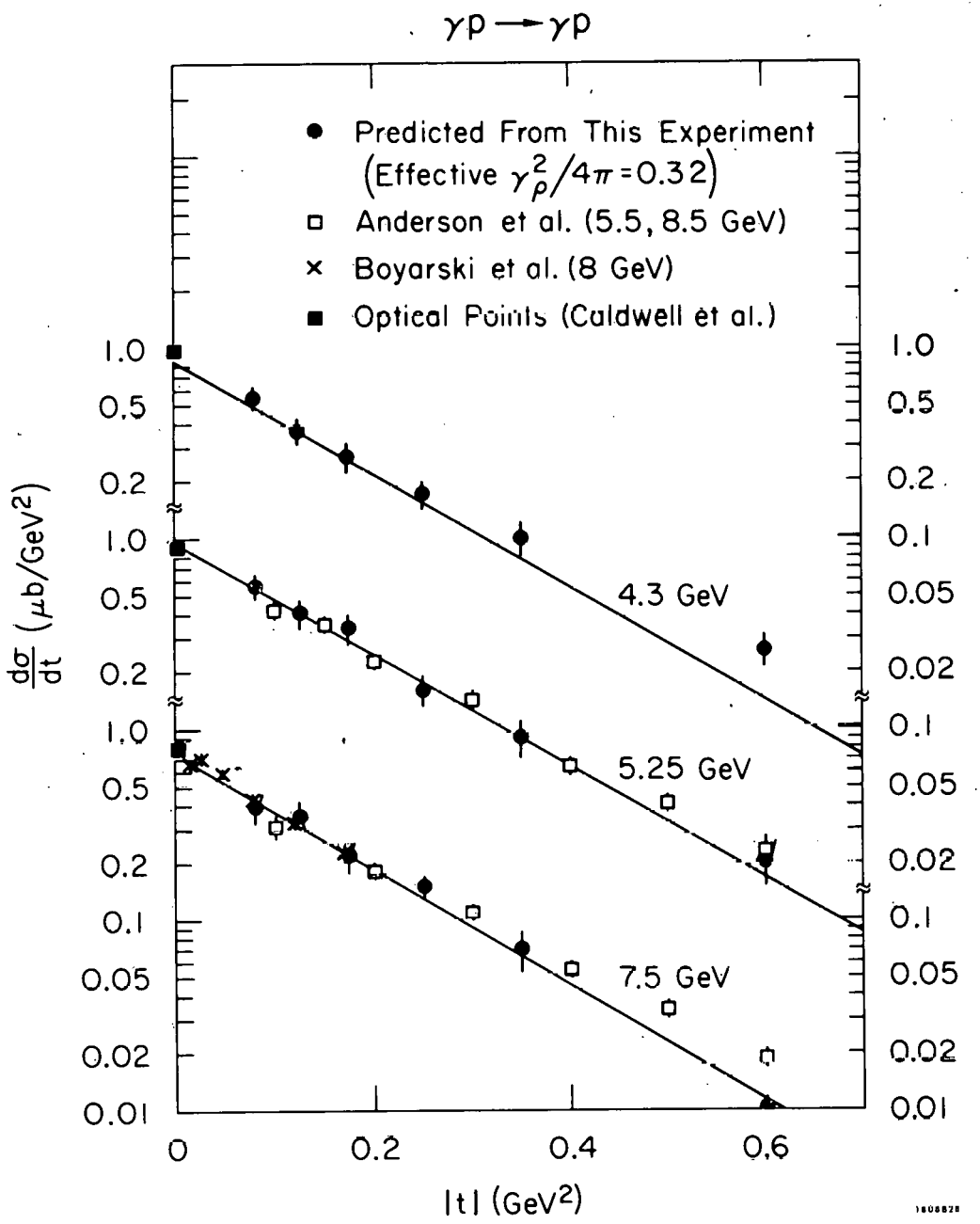

FIG. IV.16--$d\sigma/dt$ for Compton scattering calculated from the present photoproduction data of Table IV.3 using Eq. (IV.22) and $\gamma_\rho^2/4\pi = 0.32$. The straight lines represent our standard fits (see text). The VDM predicted cross sections are compared with recent Compton scattering measurements of Ref. 22 at 5.5, 8 and 8.5 GeV.

assumed for photoproduction was about 8.5 GeV^{-2}. In this context it should be noted that our forward rho cross sections and slopes are lower than some counter experiment values.[12] This discrepancy may be accounted for by the "inelastic" rho production observed in this and other experiments,[69] by using a larger mass interval to define the ρ^o or by using a different extrapolation function. Furthermore, if there were any anomalous behavior of the differential cross section for very small t values ($|t| < 0.04$ GeV^2), this experiment with its large background of electromagnetic pairs would be completely insensitive to it. We conclude from our comparison of photoproduction and Compton scattering that the two processes have the same t dependence, and within large errors and over a restricted range of comparison the same s dependence, so that by varying only one parameter, the γ-p coupling constant, it is possible to satisfy the VDM tests.

The meaning of the effective value of $\gamma_\rho^2/4\pi$ determined by our VDM tests in hydrogen is not at all clear. The magnitude of $\gamma_\rho^2/4\pi$ that is required is close to, but significantly smaller than, the storage ring value (which has photons on the vector meson mass shell). Furthermore in the comparison of single pion photoproduction with the production of vector mesons by pions, one also usually obtains rough agreement in magnitude with the VDM predictions for coupling constants around 0.30,[70] but in this case there may be disagreement in the t dependence of the two processes.[71] This coupling has also been evaluated from rho photoproduction on complex nuclei[12] and deuterium.[72] Although such studies did not yield a unique value for $\gamma_\rho^2/4\pi$, they seem to require larger values of $\gamma_\rho^2/4\pi$ (0.6-1.0) than this experiment or the electron-positron storage ring experiments. This implies that simply a change of coupling with meson mass cannot account for the deviation from

the storage ring value and therefore seems to lead away from a unique value of γ-ρ coupling at the photon mass shell. However, because of uncertainties in the nuclear effects involved, and the other differences in the experiments, the discrepancy between our results and the complex nuclei results needs further investigation.

Thus VDM appears to be violated in its most simple form. It is conceivable that more vector mesons (or multi-pion structures having the same quantum numbers as the photon) are required to saturate relation (IV.21) with the photon on its mass shell, even though no direct evidence for such objects can be found in this experiment. Another possibility is that the V-nucleon scattering amplitude changes when the V is off mass shell.[73] Similar conclusions have been reached in studies of photoproduction on deuterium.[68]

CHAPTER V

RESONANCE PHOTOPRODUCTION IN FOUR-BODY FINAL STATES

As discussed in Chapter III, the channels with a single neutral particle are much more complex and difficult to isolate from bremsstrahlung and multi-neutral background than those channels where all particles are visible. In Section III.4 cuts on the missing mass squared were determined that eliminate most of the events not belonging to the class of four-body final states produced by annihilation photons. This has been one of the main areas where the annihilation beam has provided superior results to earlier experiments using bremsstrahlung beams. Since the bremsstrahlung beams had no mechanism for determining the missing mass of an event (because their 0-C energy is calculated assuming a missing mass), only upper limits could be given for the resonance production which was observed. Equally troublesome was the complete obscuration of some resonance production in the single neutral final states by multi-neutral background.

The total cross sections as a function of the photon energy for the single neutral channels have been derived and presented in Section III.4 and Fig. III.9. The most prominent resonance found in these final states, the omega meson, has been discussed in Chapter IV together with the rho because they are related by the vector dominance model. As can be seen in Fig. IV.11, the omega events are quite well separated from the rest of the channel at the annihilation peak energies. Consequently, most of the work in this chapter has been done with a cut on the 3-pion mass spectrum to remove the omega meson. This cut removes the omega reflection in other particle combinations, making the analysis of the remaining events much more straightforward.

This chapter presents results on the quasi two-body reactions $\gamma p \longrightarrow \rho^- \Delta^{++}$ and $\gamma p \longrightarrow A_2^+ n$, as well as presenting observations on inelastic rho production by $\gamma p \longrightarrow \rho\pi N$ and a complete summary of fits to possible nucleon isobars. The fits to resonance production have all been performed using the multidimensional maximum likelihood program MURTLEBERT.[74] This method allows us to fit simultaneously associated and unassociated resonance production without double counting. It also automatically takes into account the reflections of the various resonances in computing the background to other channels. This simultaneous fitting is very advantageous for channels where many resonances are present, each in fairly small amounts.

The fractions of events in the channel $p\pi^+\pi^-\pi^o$ were obtained by a multidimensional maximum likelihood fit to the states: $\Delta^{++}\rho^-$, $\Delta^+\rho^o$, $\Delta^o\rho^+$, $\Delta^{++}\pi^o\pi^-$, $\Delta^+\pi^+\pi^-$, $\Delta^o\pi^+\pi^o$, $\rho^+p\pi^-$, $\rho^o p\pi^o$, $\rho^- p\pi^+$ and phase space, after the omega events had been removed. The cross sections obtained for the various final states are presented in Table V.1 for all three energies. The final states considered and the fitting program used were the same as those for the recent photoproduction experiments using the SLAC backscattered laser beam.[31] Furthermore, the methods for excluding multineutral events were similar, although they clearly could not be identical considering the different types of monochromaticity involved.

The fits were substantially improved by "shaping" phase space with the empirical factors

$$(1+a\cdot m^2(p\pi^+))\Big/\left[(1+b\cdot m^2(\pi^+\pi^-))\,(1+c\cdot m^2(\pi^+\pi^o))\,(1+d\cdot m^2(\pi^o\pi^-))\right]. \qquad (V.1)$$

These factors did not alter the delta-rho fractions, but they changed the cross sections for unassociated rho production significantly, while simultaneously

TABLE V.1

Cross sections obtained for the reactions $\gamma p \to p\pi^+\pi^-\pi^o$ and $\gamma p \to n\pi^+\pi^+\pi^-$, and for resonance production therein. Associated resonance production is excluded from the single resonance values and no correction (except ω) was made for decays into other channels.

	Final State	E_γ(GeV)		
		3.7 - 4.7	4.7 - 5.8	6.8 - 8.2
a)	$p\pi^+\pi^-\pi^o$	18.2 ± 2.0 μb	13.5 ± 1.5 μb	11.8 ± 1.2 μb
	ωp(*)	2.9 ± 0.4	2.3 ± 0.4	2.0 ± 0.3
	$\rho^-\Delta^{++}$	1.8 ± 0.4	0.9 ± 0.35	1.1 ± 0.2
	$\rho^o\Delta^+$	0.1 ± 0.2	0.5 ± 0.2	0.3 ± 0.2
	$\rho^+\Delta^o$	0.1 ± 0.2	0.4 ± 0.3	0.2 ± 0.2
	$\rho^- p\pi^+$	0.8 ± 0.5	1.7 ± 0.5	0.7 ± 0.4
	$\rho^o p\pi^o$	0.5 ± 0.5	(**)	0.9 ± 0.4
	$\rho^+ p\pi^-$	1.8 ± 0.5	1.9 ± 0.5	1.1 ± 0.4
	$\Delta^{++}\pi^o\pi^-$	0.5 ± 0.4	0.6 ± 0.3	0.0 ± 0.1
	$\Delta^+\pi^+\pi^-$	0.3 ± 0.3	0.0 ± 0.3	0.5 ± 0.2
	$\Delta^o\pi^+\pi^o$	0.0 ± 0.3	0.0 ± 0.3	0.0 ± 0.5
b)	$n\pi^+\pi^+\pi^-$	7.5 ± 1.5	4.6 ± 1.4	4.0 ± 1.2
	$\Delta^-\pi^+\pi^+$	1.4 ± 0.4	0.5 ± 0.3	0.2 ± 0.2
	nA_2^+	0.8 ± 0.3	0.6 ± 0.3	0.3 ± 0.3
	$\rho^o n\pi^+$	1.2 ± 0.7	(**)	2.0 ± 0.6

(*) Including 10% neutrals.
(**) Unacceptable fits: see text.

improving the chi-square of the fit in the various two-pion mass projections. It has been assumed that this empirical mass shaping allows a more accurate determination of the amounts of specific resonance production in the channel when all the deviations of the backgrounds from pure phase space are not fully understood.

There are numerous possible explanations for this deviation from the expected phase space shape. It may be, as suggested by some forms of duality, that all background is merely a manifestation of resonances in a crossed channel, in which case the usual Lorentz invariant phase space is an inappropriate assumption.[75] Another possibility is that the angular distribution of the resonances present (observed and unobserved) may change the shape of their reflections in other mass combinations, i.e., it may be appropriate to modify the usual phase space to a so called peripheral phase space.[76] Finally, if there were indeed a large contamination of multi-neutral events present, this would change the resulting phase space. The net result of these modifications is essentially to return to something like hand drawn backgrounds, but with each curve consistently projected into all mass combinations.

In the mass projections of the 3-pion final state (See Fig. IV.11) significant low mass enhancements can be noted at all energies, especially the higher ones. The shape of the data deviates strongly from the shape implied by phase space together with the reflections of all the resonances in other channels. Considering the presence of A_2^+ in the $\pi^+\pi^+\pi^-$n final state, as discussed in the next section, and the suggestive bumps at the A_2 mass visible in the 3.0-3.7 GeV and 7.5 GeV data, fits were made to final states including A_1^o and A_2^o. These fits allowed 0±2% at 4.3, 8±4% at 5.25 and 13±2% at 7.5 GeV of A mesons. This corresponds to an upper limit of 1μb on A_2^o production

at 7.5 GeV with 90% C. L. These percentages may be just a manifestation of the deviation of the shape of this mass spectrum from pure phase space, rather than actual presence of A_1^o or A_2^o mesons. Moreover, fitting with the A mesons included had no significant effect on the fractions of the final states (listed in Table V. 1) obtained in the data when the backgrounds were obtained using the shaping factors discussed above. This topic will be examined more fully in the Section V. 2.

V. 1 Associated Rho and Delta Production in the Final State $p\pi^+\pi^-\pi^o$

Associated rho and delta production in the reaction

$$\gamma p \longrightarrow \rho^- \Delta^{++} \qquad (V.2)$$

has been observed in several previous bubble chamber experiments.[9,10] Since the ρ^- cannot be produced diffractively, the next most simple assumption is that reaction (V. 2) proceeds mainly through one pion exchange (OPE). In this case the $\gamma p \longrightarrow \rho^- \Delta^{++}$ cross sections are proportional to $\Gamma(\rho\pi\gamma)$, the rho radiative decay width, which is small (1/9 of $\Gamma(\omega\pi\gamma)$) by SU(3)[19] and difficult to measure directly. Estimates of $\Gamma(\rho\pi\gamma)$ have therefore been given[9,10] using an OPE model. This experiment extends the cross section measurements for reaction (V. 2) up to 8.2 GeV. Thus the energy dependence of $\gamma p \longrightarrow \rho^- \Delta^{++}$ can be studied for a wide range of photon energies, serving as a test of the OPE assumption. In fact, the dependence of this cross section on the photon energy is found to be quite different than that found for reactions dominated by an OPE process.[63] This questions the validity of the estimates of $\Gamma(\rho\pi\gamma)$ which were based on this assumption.

Only the monochromatic events, which give constrained kinematic fits, were used in the study of the energy dependence of the delta-rho cross

sections. To avoid systematic biascs, the 1.3 and 5.25 GeV data, which had been previously published,[2,3] were reanalysed and the same selection criteria, cuts, resonance shapes and fitting procedures were used for all energy ranges. The cuts excluded events with missing masses not near the pi-zero, with low confidence levels, with very fast forward neutral systems, or with competing 3 or 4-constraint fits. Omega events have been removed by demanding $m(\pi^+\pi^-\pi^0)>0.81$ GeV.

A scatter plot of $m(p\pi^+)$ versus $m(\pi^0\pi^-)$ for the channel $p\pi^+\pi^-\pi^0$ at 7.5 GeV is shown in Fig. V.1a together with the $\pi^0\pi^-$ and $p\pi^+$ mass projections (Fig. V.1b and V.1c). The shaded areas correspond to Δ^{++} events in Fig. V.1b and to ρ^- events in Fig. V.1c. It can be seen that at this energy the associated $\rho^-\Delta^{++}$ production is well separated from the background and thus there are no difficulties in determining the cross section in spite of its smallness. Similar $\rho^-\Delta^{++}$ signals are obtained at 4.3 and 5.25 GeV with a somewhat larger background. The signals become more pronounced when cuts are introduced on the four-momentum transfer, $|t(\gamma,\rho^-)|<0.6(\mathrm{GeV/c})^2$. The fitted amounts of ρ, Δ and $\rho\Delta$ as found by MURTLEBERT in all charge states are given in Table V.1. In Table V.2 the slopes B of the t distribution for ρ^- production in reaction (V.2) are given, assuming a momentum transfer distribution of the form $A\exp(-Bt)$. The diagonal density matrix elements, in the Jackson system, for the ρ^- and Δ^{++} have been evaluated and are also given in Table V.2. In addition, the values of the shaping parameters a, b, c, d of Eq. (V.1) obtained in the fits are listed in Table V.2.

In Fig. V.2 the $\rho^-\Delta^{++}$ cross sections for our three monochromatic energies are plotted together with two recent cross section determinations at 2.8 and 4.7 GeV.[31] The events in both these experiments have much less

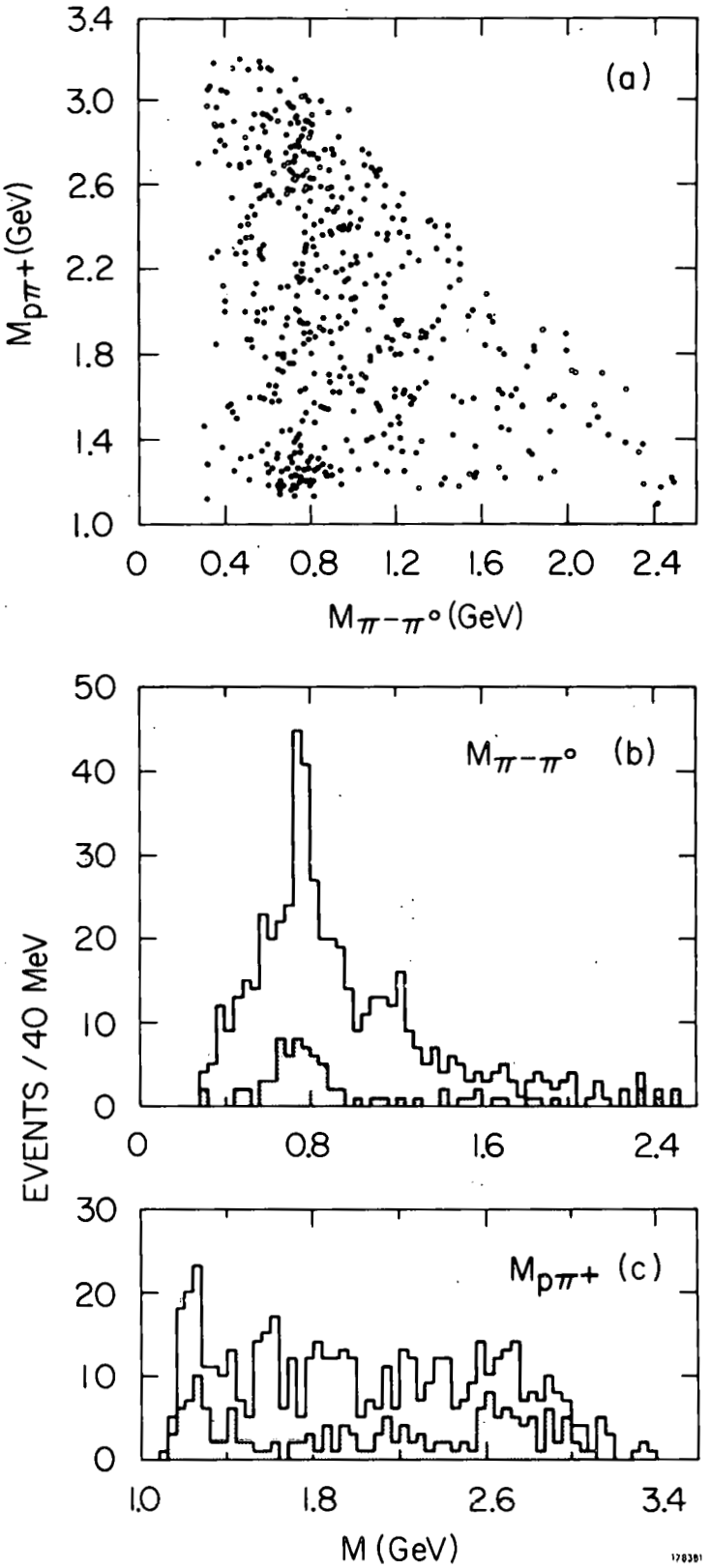

FIG. V.1--(a) Scatter plot of $M(p\pi^+)$ versus $M(\pi^0\pi^-)$ for $\gamma p \longrightarrow p\pi^+\pi^-\pi^0$ at 7.5 GeV. (b) and (c) are the $M(\pi^0\pi^-)$ and $M(p\pi^+)$ mass distributions respectively. The shaded areas are: $M(\pi^0\pi^-)$ distributions for Δ^{++} events ($1.12 < M(p\pi^+) < 1.32$ GeV) in (b), and the $M(p\pi^+)$ distribution for ρ^- events ($0.66 < M(\pi^0\pi^-) < 0.86$ GeV) in (c). Events with $m(\pi^+\pi^-\pi^0) < 0.81$ GeV were removed from the plot to exclude ω events.

TABLE V.2

Momentum transfer slopes B and density matrix elements obtained in this experiment for the reaction $\gamma p \longrightarrow \rho^- \Delta^{++}$. B is the slope of the t distribution, ρ^{ρ}_{00} and ρ^{Δ}_{11} the diagonal elements for ρ and Δ, all for this reaction. Errors in the latter include an uncertainty from the unknown background decay distribution. Also listed are the fitted values obtained for the mass shaping parameters of Eq. (V.1).

E_γ		3.7-4.7 (GeV)	4.7-5.8 (GeV)	6.8-8.2 (GeV)
$B(GeV^{-2})$		7.7 ±1.1	6.4 ±3.1	7.6 ±2.5
ρ^{ρ}_{00}		0.28±0.13	0.64±0.27	0.60±0.22
ρ^{Δ}_{11}		0.26±0.10	0.41±0.18	0.21±0.13
a	$m(p\pi^+)$	2.25±0.85	9.04±2.67	10.0 ±3.87
b	$m(\pi^o\pi^-)$	--	0.96±0.48	0.13±0.10
c	$m(\pi^+\pi^-)$	0.41±0.24	1.95±0.72	5.95±1.57
d	$m(\pi^o\pi^+)$	1.58±0.55	--	2.56±0.78

background because of their quasi-monochromatic photon beams than was the case for the bremsstrahlung events used in earlier experiments. Also, the same resonance parameters, resonance shapes and fitting programs have been used for both the present experiment and that of Ref. 31, minimizing systematic errors. A least square fit of the five cross sections to the form

$$\sigma(\gamma p \longrightarrow \rho^{-}\Delta^{++}) = CE_{\gamma}^{-a} \qquad (V.3)$$

gave $C=3.5\pm1.2$ and $a=0.6\pm0.2$ where σ is expressed in microbarns and E_{γ} in GeV.

There is no unique prescription for relating the energy exponent a in Eq. (V.3) to the production mechanism. Therefore three approaches are used to study this relationship: (a) comparing with similarly obtained exponents for reactions believed to be dominated by OPE; (b) extracting the energy dependence of σ from $d\sigma/dt$, which in a Regge model should be proportional to E_{γ}^{-n} with n=2, 1, 0 for pion, vector meson or Pomeron exchange respectively (at least for small t); (c) attempting to fit the data with a specific OPE model.

In approach (a) it has been noted[63] that for our energy range, reactions believed to be OPE-dominated have a in the range 1.6-2.5. In particular, the reaction $NN \longrightarrow \Delta\Delta$, an especially likely OPE candidate which has been studied up to 30 GeV,[77] has been shown to have an energy dependence with $a=2.5\pm0.3$. In addition the reaction $\gamma p \longrightarrow \pi^{-}\Delta^{++}$, another OPE candidate examined in this experiment, has an energy dependence yielding $a=1.74\pm0.16$ (See Fig. IV.9). Clearly the dependence of reaction (V.2) falls outside this range. No firm conclusion may be reached, however, since the effects

of the kinematic boundaries may be substantial, due to the increased importance of the minimum momentum transfer at lower photon energies.

Approach (b) takes into account these effects of the finite physical range of t varying with energy. This occurs because t_{min} (the minimum t) of the Chew-Low plot for reaction (V.2),cuts off a substantial fraction of the small t region and reduces the total cross section at low energies. The form $d\sigma/dt = AE_\gamma^{-a'} e^{Bt}$ is assumed in the formula

$$\sigma(E_\gamma) = \int dm_{\pi\pi} BW(m_{\pi\pi}) \int dm_{p\pi} BW(m_{p\pi}) \int_{t_{min}}^{t_{max}} dt \, \frac{d\sigma}{dt} \quad ,$$

where BW(m) is a relativistic Breit Wigner factor and $B = 7\ GeV^{-2}$, taken as representative of the values given in Table V.2. The integral was performed over the mass range within two full widths on either side of the resonance in question, and t_{max} put equal to infinity. The resulting $\sigma(E_\gamma)$ over our energy range was then fitted to the form of Eq. (V.3) and for each a' yields an effective exponent, a_{eff}. The fit determines that $a' - 2$ corresponds to $a_{eff} = 1.4$ and only for $a' = 1.2$ does one find $a_{eff} = 0.6$, our experimental value.

Approach (c) uses an OPE model with absorption introduced by a sharp cut-off.[66] This model has already been shown in Section IV.2 to give a fair description of our results for omega photoproduction, another quasi-two body reaction. It has two parameters, $\Gamma(\rho\pi\gamma)$, the rho radiative width, and R, the cut-off radius. The latter is usually determined by a fit to the t-dependence of the reaction studied and in hadron induced reactions is about 1 fermi.[66] Using the relation $R^2 \simeq 4B$,[78] the slopes in Table V.2 would also

imply a radius of about 1 fermi, which is the same order of magnitude observed for hadron-induced reactions.

The broken lines in Fig. V.2 show the cross sections obtained with this model for R=0.5, 0.7 and 1.0 fermi, all assuming[79]

$$\Gamma(\rho\pi\gamma) = (1/9)\ \ \Gamma(\omega\pi\gamma) = 0.134 \qquad (V.4)$$

the SU(3) value.[19] As R increases, the t-dependence becomes steeper, and the low energy cross sections are depressed more than the high by the effects of the kinematic boundaries. Hence the energy dependence found can indeed be reproduced by OPE, but only if $\Gamma(\rho\pi\gamma)>0.5$ MeV (with $R\approx 0.8$ fm). The same conclusion is reached when the OPE model of Wolf[80] is applied. Such a large value is in contradiction with the result of a search for the process $\rho \longrightarrow \pi\gamma$ which found[81] $\Gamma(\rho\pi\gamma)<0.6$ MeV at the 97% confidence level.

Apparently the energy dependence of the cross section for the reaction $\gamma p \longrightarrow \rho^- \Delta^{++}$ in the energy range 2.5-8 GeV cannot be reproduced using an OPE process and the SU(3) value of $\Gamma(\rho\pi\gamma)$. A similar possible discrepancy with an OPE mechanism for reaction (V.2) was recently reported by Eisenberg et al.,[82] who found in a comparison of γp and γd reactions that the ratio $\sigma(\gamma n \longrightarrow \omega\Delta^0)/\sigma(\gamma p \longrightarrow \rho^-\Delta^{++})$ at 4.3 GeV is in disagreement with OPE + SU(3) predictions. This experiment looked for the reaction $\gamma n \longrightarrow \omega\Delta^0$ and found the cross section to be less than 0.5μb in the mode where $\Delta^0 \longrightarrow p\pi^-$. By combining SU(3) and the OPE model, however, it follows that this ratio should in fact be 2, indicating again that the combined prediction of OPE and SU(3) is violated.

One possible explanation for this discrepancy is that OPE does not dominate these reactions. It is possible that vector meson exchanges are

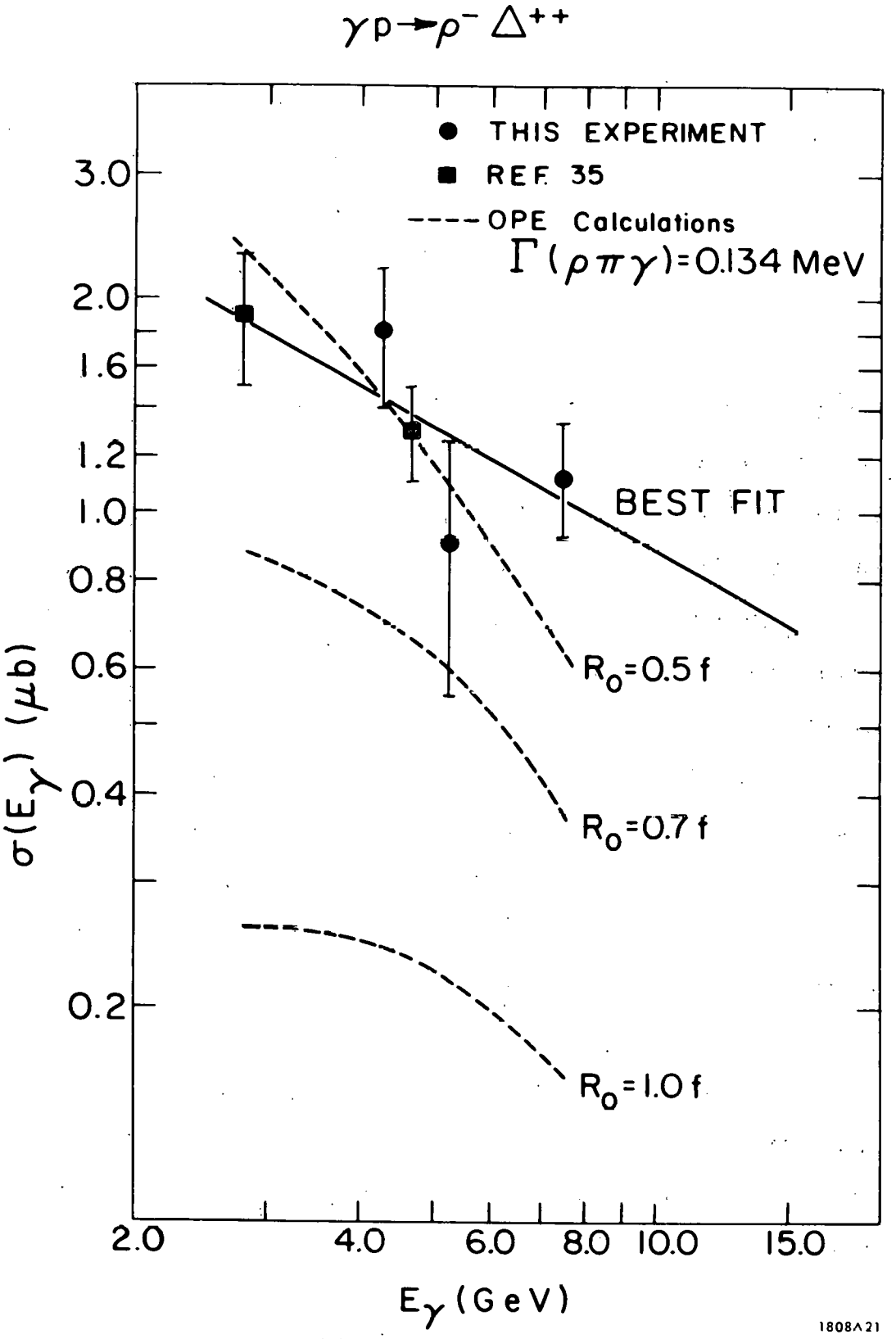

FIG. V.2--$\gamma p \longrightarrow \rho^- \Delta^{++}$ cross sections determined in this experiment and from Ref. 31, versus the photon energy E_γ. The full line is best fit of the data to Eq. (V.3) which yields $a = 0.6 \pm 0.2$. The dashed curves are the OPE calculated cross section for various absorption radii and fixed coupling ($\Gamma(\rho\pi\gamma) = 0.135$ MeV).

important in these reactions, since within the vector dominance model $\rho^+\rho^-\rho^o$ couplings could be quite strong.[83] Moreover in a Regge pole model the energy dependence of σ should be given by E_γ^{-1} for vector meson exchange. This could account for the unexpected energy dependence observed for $\gamma p \longrightarrow \rho^-\Delta^{++}$, but more accurate data on the production and decay of the final state $\rho^-\Delta^{++}$ are needed to determine the mechanism of this reaction.

Table V.1 lists the other charge states of delta-rho, but no significant quasi two-body production other than $\rho^-\Delta^{++}$ is found. The delta-rho charge states do not, for example, seem to appear in simple ratios of 3:2:1 which would be expected if OPE dominated the reactions $\gamma p \longrightarrow V\Delta$. Even allowing for the relative decay of Δ^+ and Δ^o into proton and neutron channels, the amounts of Δ^+ and Δ^o production observed do not support the simple OPE hypothesis. The cross sections for nucleon isobars other than Δ^{++} are all rather small, as can be seen in Fig. V.3 for the 7.5 GeV data. Δ^- production in the $\pi^+\pi^+\pi^-n$ channel is large at 4.3 GeV, but decreases rapidly with energy (See Fig. V.4). Although these data do not reveal much about nucleon resonance production in these final states, it is easily possible to conclude that there are substantial rho signals in all charge states not associated with any resolved baryon resonance production. This will be studied in detail in Section V.3.

V.2 A_2 Meson Production

The first observation of the photoproduction of the A_2 meson was reported in a previous publication on this experiment.[4] It was expected on the following grounds.[84] The A_2 is known to decay predominately into $\rho\pi$. Since it has spin-parity 2^+, it should couple only to transverse rhos.

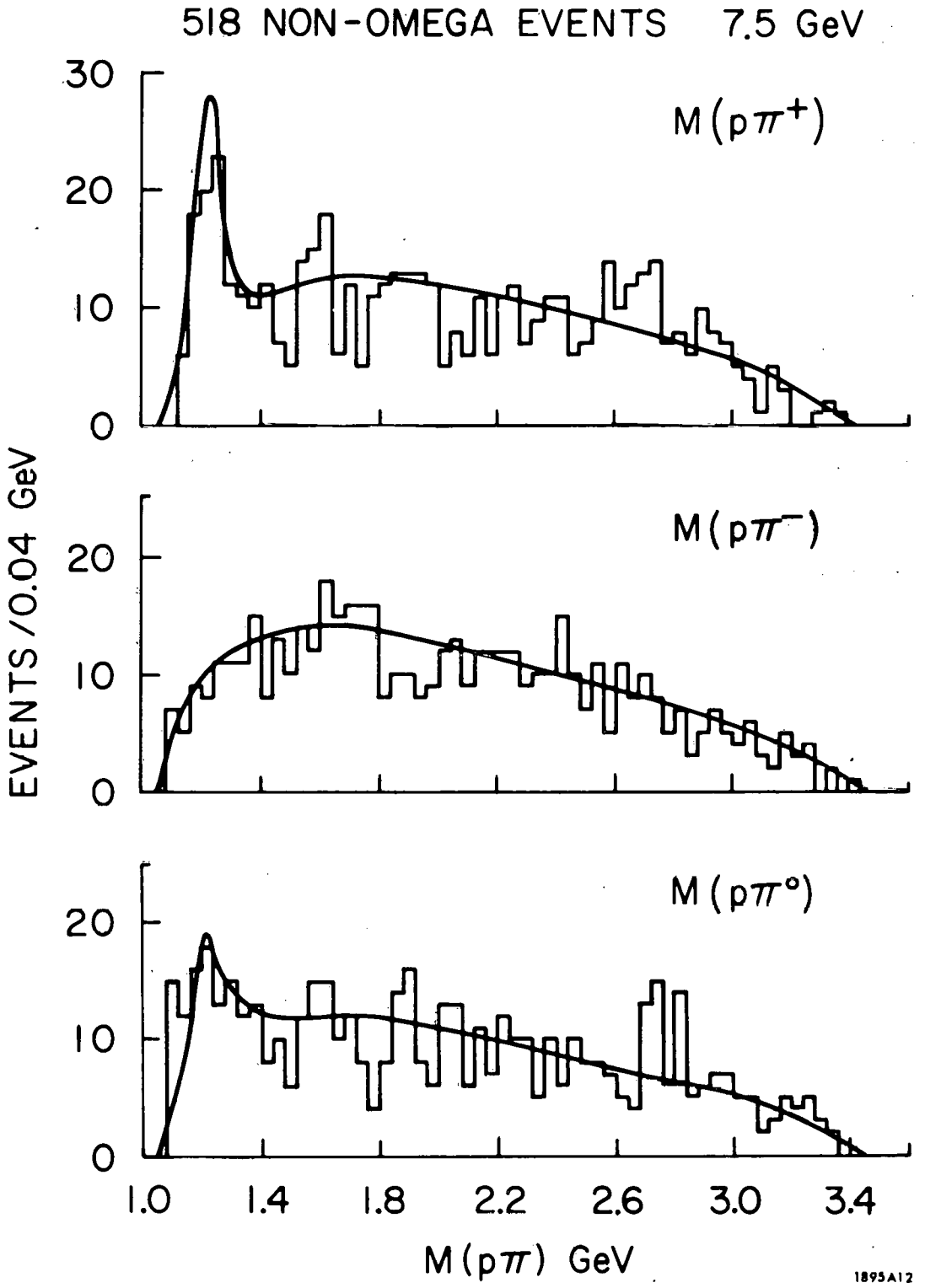

FIG. V.3-- M(pπ) in all charge states for 1-C fits in the 7.5 GeV data with $-0.18 < mm^2 < 0.10$ GeV^2, $P(\chi^2) > 0.005$ and omega events removed. The fit curves incorporate the resonances listed in Table V.1.

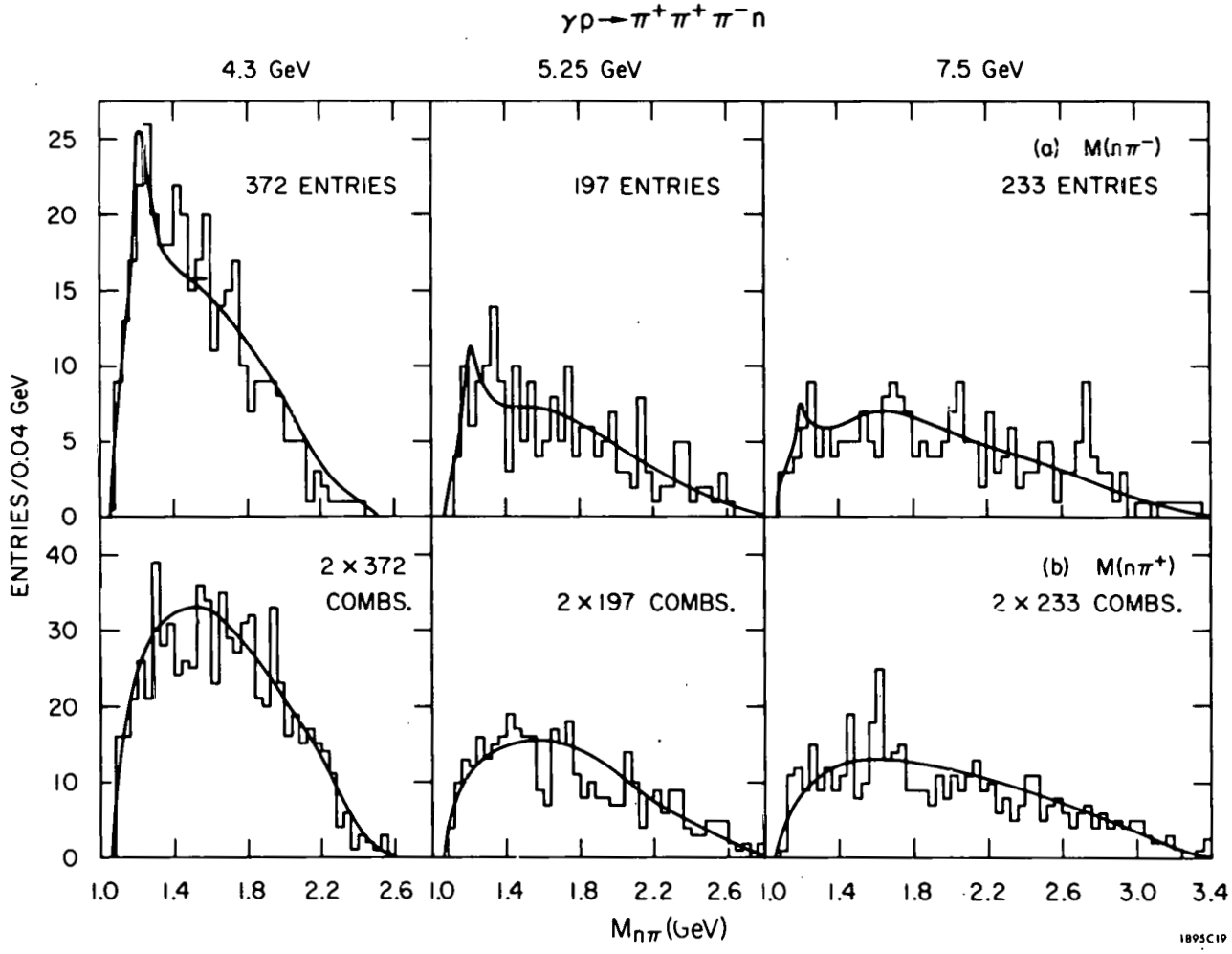

FIG. V.4 -- M(nπ) for all 1-C fits to $\gamma p \longrightarrow \pi^+\pi^+\pi^- n$ with $0.6 < mm^2 < 1.2$ GeV^2 and $P(\chi^2) > 0.005$. (a) M(nπ⁻) with a fit curve including Δ^- production. (b) M(nπ⁺) with fit curve to phase space and the reflections from the other resonances listed in Table V.3.

Invoking the vector dominance model, it should thus also couple to photons and show a substantial decay into the $\gamma\pi$ mode. Although this process has not been directly observed, if there is indeed an appreciable decay width, this coupling should allow the photoproduction of A_2 mesons via OPE in the reaction

$$\gamma p \longrightarrow A_2^+ n \,. \qquad (V.5)$$

The reaction is observed in our data with a cross section which decreases rapidly with photon energy. It is the only quasi two-body reaction observed in the channel $\pi^+\pi^+\pi^-n$.

Figure V.5 shows the invariant three-pion mass distributions for fits to reaction (5). All of the data shown are 1-C fits with missing mass squared inside our standard neutron cut, $(0.6,\ 1.2)\ \mathrm{GeV}^2$, and with confidence levels better than 5%. The shaded events are those with $|t(p,n)| < 0.5\ (\mathrm{GeV}/c)^2$, indicating that the production mechanism is highly peripheral. Figure V.5d combines the small momentum transfer events at all energies (i.e., the shaded events of Figs. V.5a-c) and has been used to fit the A_2 mass and width, yielding $M(A_2) = 1.30 \pm 0.01$ GeV and $\Gamma(A_2) = 0.070 \pm 0.044$ GeV. These agree with hadronic production data.[85]

Maximum likelihood fits to all the data in the channel $\pi^+\pi^+\pi^-n$ at our three annihilation energies yield the results summarized in Table V.1. Note that the cross sections in Table V.1 at 4.3 and 5.25 GeV are somewhat lower than those of Ref. 4 because of more accurate fitting and a revised normalization. The results are corrected for all experimental and analysis losses. Also note that the presence of a small A_2^+ signal at 7.5 GeV is supported by the structure of the data at the small momentum transfers. The fits in fact

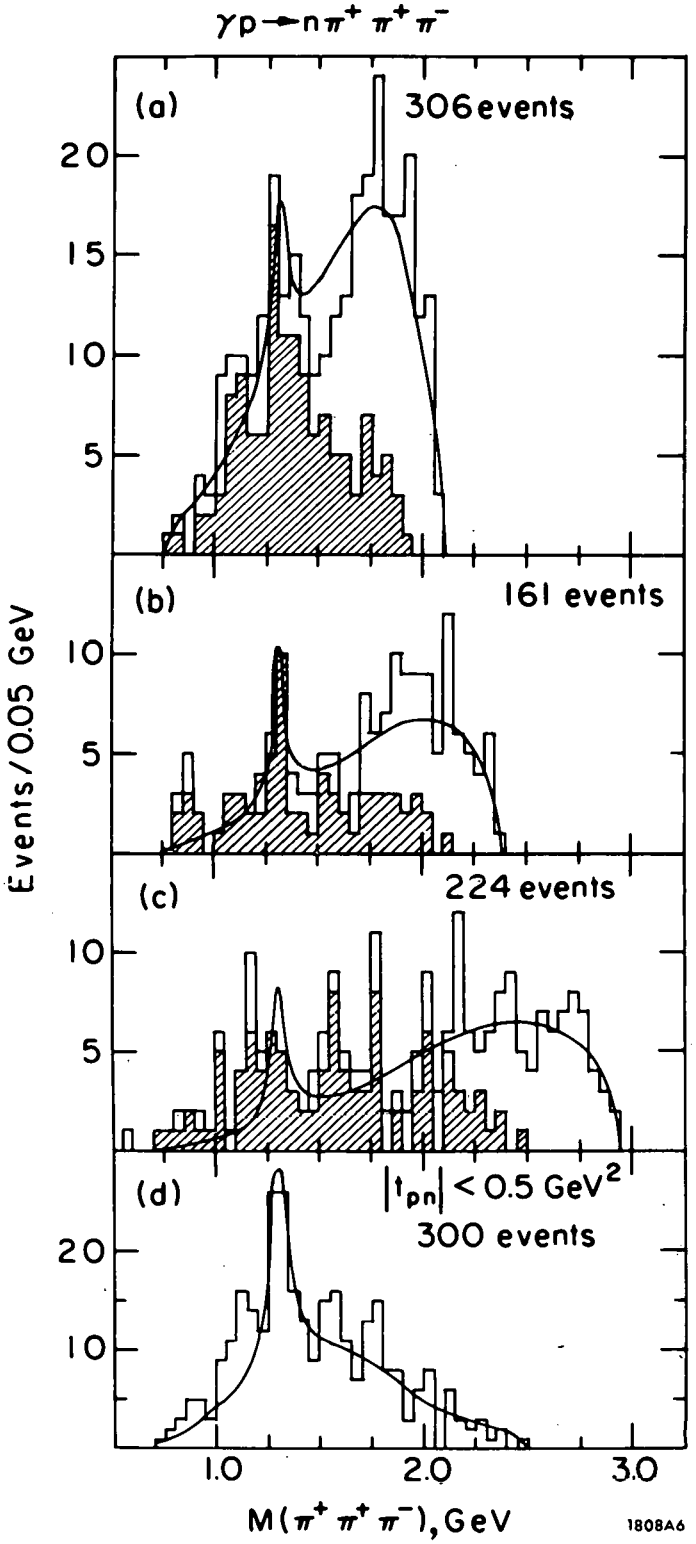

FIG. V.5--$M(\pi^+\pi^+\pi^-)$ distribution in the reaction $\gamma p \longrightarrow \pi^+\pi^+\pi^- n$ at (a) 4.3 GeV, (b) 5.25 GeV and (c) 7.5 GeV. The shaded areas represent events with $|t(p,n)| < 0.5$ GeV^2. (d) Mass distribution combining the three energies for above t cut. The curves are best fits to A_2^+ resonance ($M(A_2)$=1.30 GeV, $\Gamma(A_2)$=0.1 GeV) and phase space (see Table V.3).

reject the three-pion decay mode, yielding the branching ratio

$$\frac{A_2^+ \longrightarrow \rho^0\pi^+}{A_2^+ \longrightarrow \text{all}(\pi^+\pi^+\pi^-)} = 1.0\ {}^{+0}_{-0.2} \qquad (V.6)$$

which also agrees with hadronic production data. This association of A_2^+ with a rho in one of the two $\pi^+\pi^-$ charge combinations is also shown graphically in Fig. V.6 for the combined 4.3 and 5.25 GeV data. This figure shows the combined data, divided into two mutually exclusive subsets: those 3-pion events for which at least one neutral dipion combination is in the rho region and those for which no such combination is in the rho region. Although the A_2^+ signal is only found in those events associated with a rho, this is less convincing because the kinematics of the decay of an object of mass 1.3 GeV into three pions constrains the two pion combinations to be preferentially in or near the rho region.

The energy dependence of the A_2 cross section is consistent with that expected for an OPE production mechanism. As in Ref. 4 it is possible to derive the A_2^+ width by assuming that A_2 production in this channel is due entirely to OPE.[86] This yields

$$\Gamma(A_2^+ \longrightarrow \gamma\pi^+) = \frac{1}{10}\ \frac{g^2_{A_2\pi\gamma}}{4\pi}\ \frac{q^5}{m^4_{A_2}} \approx 0.5 \text{ MeV}. \qquad (V.7)$$

This value is obtained for an absorption radius of about 1 fermi in the OPE calculation. This same radius has been found to give reasonable results with our omega data (See Section IV.2).

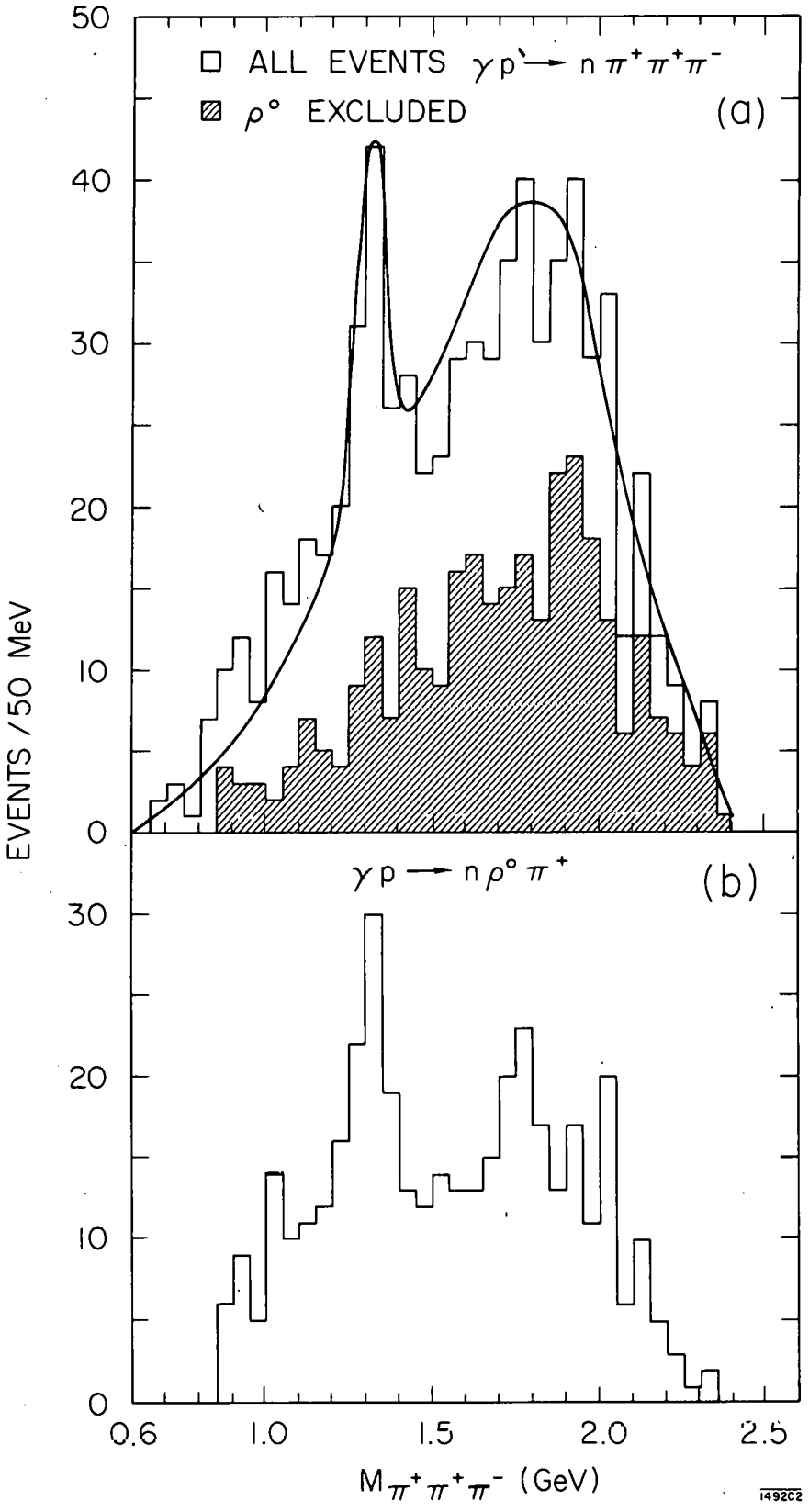

FIG. V.6--(a) $M(\pi^+\pi^+\pi^-)$ distribution for $\gamma p \longrightarrow \pi^+\pi^+\pi^- n$, combined data from 4.3 and 5.25 GeV. The shaded area represents the 3 pion effective mass for events with no $\pi^+\pi^-$ combination in the ρ band (0.60-0.85 GeV). The curve is a one dimensional fit to an A_2^+ resonance plus Lorentz invariant phase space. (b) The $M(\pi^+\pi^+\pi^-)$ distribution for events having at least one $\pi^+\pi^-$ combination in the ρ band.

The clear signal of the A_2 in the neutron channel leads us to reexamine our 3-pion mass spectra in the proton 4-body final states. These invariant mass plots for eight different photon energy intervals have been shown in Fig. IV.11. In both the 7.5 GeV data and the 3.0-3.7 GeV data there is a bump in the A_2 mass region. Since the 0-C data may contain a large proportion of multi-neutral events, no conlcusions about the 4-body final state should be drawn from it except in the case of extremely sharp and well separated resonances. In thc 7.5 GeV data, on the other hand, there is a excess of about 16 events/80 MeV over an average background level of 24 events/80 MeV in the mass interval 1.28-1.36 GeV. This is about a 3 standard deviation effect,and thus it is on the threshold of significance.

The A_2 has charge conjugation opposite to the γ, and so clearly any A_2^o production could not be diffractive. In addition, the isospin coupling relations are such that the A_2^o should not be produced by pion exchange. Therefore any production mechanism invoked to explain the presence of A_2 in thc $p\pi^+\pi^-\pi^o$ channel must be more complicated. Moreover, no structure can be said to exist in the A_2 region in either the 4.3 GeV or the 5.25 GeV data, although the entire low mass region is enhanced over what phase space predicts for these data, so a mechanism must be considered which favors production at higher energy if the 7.5 GeV effect is to be accorded any significance.

The structure has been subjected to multidimensional fits where A_2 (1300) accounts for $6.8\pm2.3\%$ of thc channel. This is again a three standard deviation signal corresponding to 35 ± 12 events or at this energy about 0.7 ± 0.25 μb. This signal is found to be largely associated with small momentum transfers to the final proton, $|t(p,p)| < 0.5$ $(GeV/c)^2$, whereas a very large portion of the background goes away (see Fig. V.7). The signal

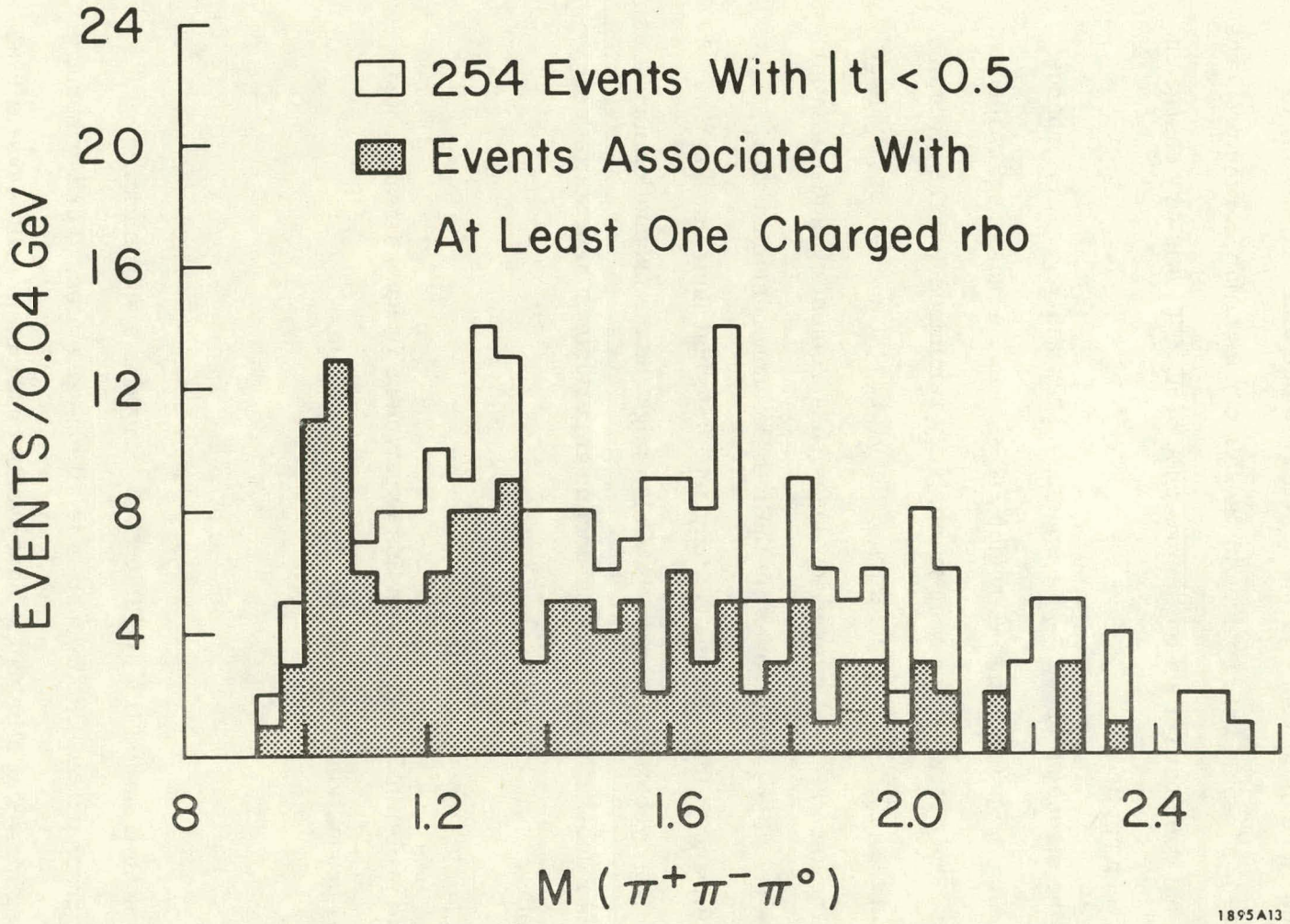

FIG. V.7--$M(\pi^+\pi^-\pi^0)$ at 7.5 GeV for $|t(\gamma, 3\pi)| < 0.5$ GeV^2. The shaded events have at least one charged dipion pair in the rho mass band.

remains quite strong when the final state pions are required to be in at least one charged rho combination. If the signal were due to an A_2^o meson, the decay mode $\rho^o\pi^o$ would be forbidden by isospin conservation, so the presence of a ρ^o signal does not reflect on the presence of A_2^o. This is why charge rho cuts have been applied.

In the structure of the 3-pion spectrum shown in Fig. V.7, enhancements can also be noted in the A_1^o region and also in the mass region 1600-1700 MeV. The overall mass spectrum is very reminiscent of the structure observed in the $m(\pi^+\pi^-\pi^o)$ spectrum at 8 GeV/c in $\pi^+ d$ interactions by Bugg et al.[23] They see a three-humped low mass enhancement structure similar to that observed here. They identify their three enchancements at A_1^o, A_2^o, and $\phi(1670)$, and at least for the A_2^o they speculate that their data may be explained by isovector exchange. This also might be the production mechanism for A_2^o in our data, if indeed this enhancement persists in high statistics experiments.

V.3 Inelastic Rho Production

The preliminary reports on this experiment[2,3] have already noted substantial production of rhos in the inelastic reaction

$$\gamma p \longrightarrow \rho\pi N. \qquad (V.8)$$

As can be seen from the fits of Table V.1, there is a substantial amount of unassociated rho production in all charge states. Furthermore, our missing mass cut eliminates most events produced in multi-neutral reactions. The relative abundance of neutral and charged rhos in $\gamma p \longrightarrow \rho\pi N$ is a function of their production mechanism. Charged rho production cannot be

diffractive, while neutral rho production will be suppressed if the rhos are produced via isovector exchange. Therefore the production mechanisms for various charge states may be reflected in their cross sections. Figure V.8 shows the invariant masses of the various dipion combinations in the channel $p\pi^+\pi^-\pi^o$ for the 7.5 GeV data with omega events removed. Significant rho production is seen in every charge state.

Although the 7.5 GeV data is more clearly separated, these signals are present at all energies as is shown in Fig. V.9 and Table V.1. The darkened events are those with small momentum transfers to the dipion system. Photoproduction of ρ^+, ρ^- and ρ^o is clearly visible, but not all of these events are peripheral. The cross sections in Table V.1 are from a multi-dimensional fitting program, as explained above, so the cross sections for single resonance production are clearly exclusive of those for associated resonance production. None of the rho cross sections has been changed by more than one standard deviation when possible A_1^o and A_2^o were allowed in the fits. For the 5.25 GeV data good fits could not be obtained to the $\pi^+\pi^-$ mass spectrum in either the proton or the neutron channels, because the rho signal was anomalously broad with a background unlike phase space. We are unable to account for this effect (see Section II.5), which does not occur at other energies, but which does occur to a lesser degree in the other rho charge states at 5 GeV. This effect probably diminished the $\rho^-\Delta^{++}$ cross section observed at 5.25 GeV. Since the signal is clear at the other annihilation energies, we prefer not to give a cross section for unassociated ρ^o production at this energy. We conclude that there is an appreciable inelastic rho production in the channel $p\pi^+\pi^-\pi^o$ which does not decrease rapidly with photon energy.

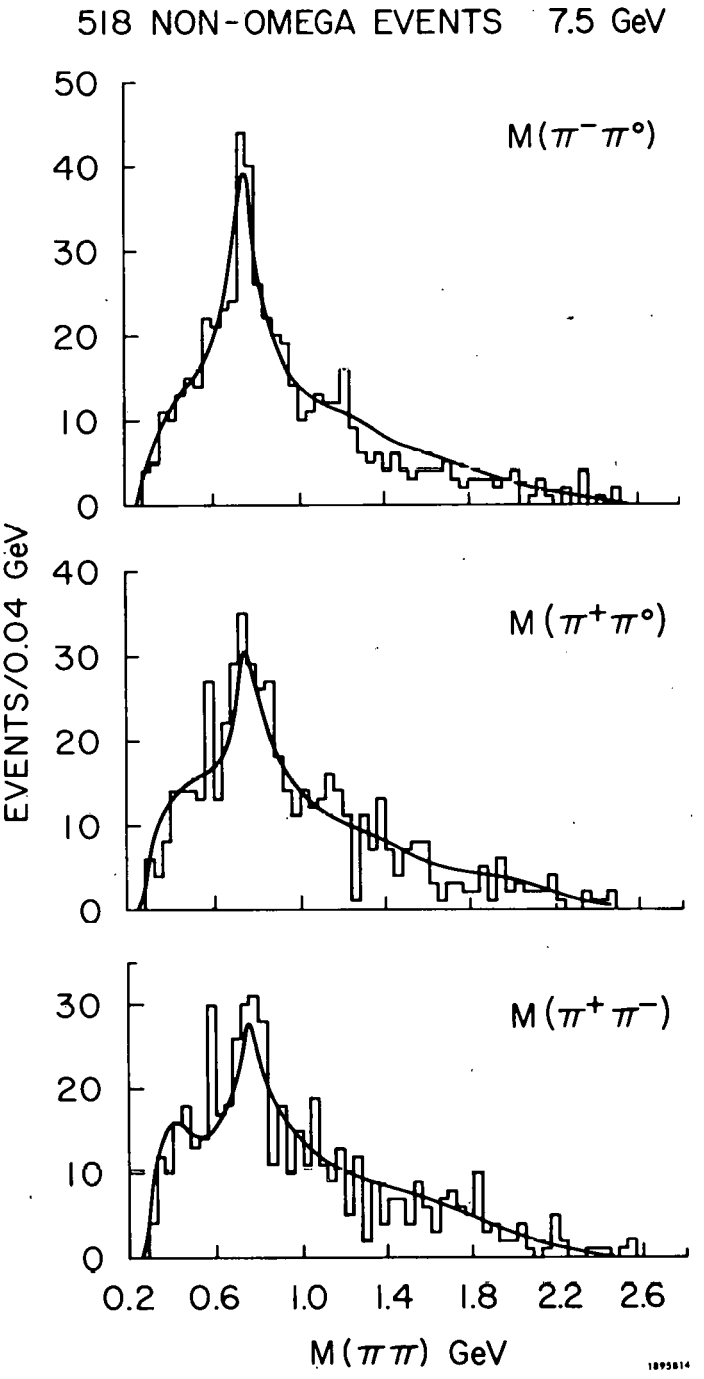

FIG. V.8-- Dipion masses in all charge combinations for 1-C fits in the 7.5 GeV data to $\gamma p \longrightarrow p\pi^+\pi^-\pi^0$ with $-0.18 < mm^2 < 0.10$ GeV^2, $P(\chi^2) > 0.005$ and omega events removed. The fit curves incorporate the resonances listed in Table V.1.

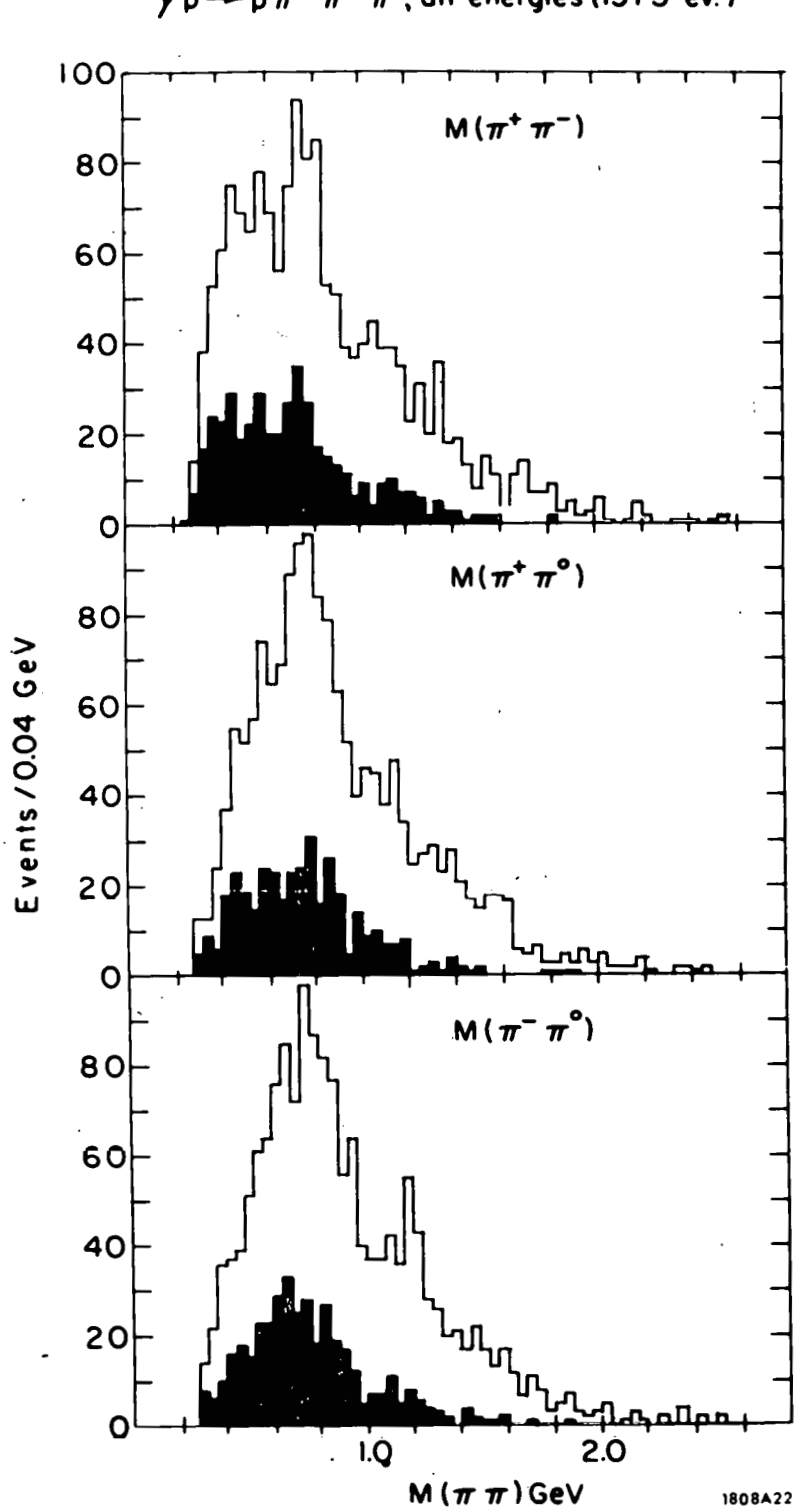

FIG. V.9--$M(\pi\pi)$ distributions for the reaction $\gamma p \longrightarrow p\pi^+\pi^-\pi^0$ at 4.3, 5.25 and 7.5 GeV combined. Shaded areas represent events with $|t(\gamma,\pi\pi)| < 0.5$ GeV^2. All ω ($M(\pi^+\pi^-\pi^0) < 0.81$ GeV) and $\rho^-\Delta^{++}$ events ($M(\pi^0\pi^-) = 0.60$-0.85 GeV and $M(p\pi^+) = 1.15$-1.30 GeV) are removed.

Figure V.10 shows the invariant dipion mass in the channel $\pi^+\pi^+\pi^-$n at 7.5 GeV. The fits in the neutron channel at all energies included the possibility of an A_2^+ decaying into ρ^o. The exact percentage of ρ^o in this channel varies as the shape of the rho is changed from the standard Breit-Wigner to a skewed shape by varying the exponent n in Eq. (IV.5), but in all cases it constitutes 40-50% of the neutron channel at 7.5 GeV. The signal is not so impressive at other energies, but is present at all energies with a cross section that apparently rises with energy. The SLAC backscattered laser beam experiment has also observed very prominent rho signals in all charge states in these 4 body channels.[31]

In order to gain information about the possible production mechanism of the vector mesons produced in these channels, the $\rho^\pm$ and ρ^o invariant masses for events with small momentum transfer ($|t| < 0.5$ GeV^2) between the photon and the vector meson are plotted in Fig. V.11. Excluded from the graphs are all events having ω, $\rho\Delta^{++}$ or A_2^+ production. Thus reflections from the quasi two-body reactions discussed above are eliminated as much as possible. It is evident from Fig. V.11 that there is quite a significant ρ^o production, associated with both $p\pi^o$ and $n\pi^+$, remaining after all these cuts and that it is peripheral production. The signal for charged rho production at small $|t|$ values is much weaker. This has led Wolf to suggest that these inelastic ρ^o may be at least in part diffractively produced.[24]

To examine the possibility of a diffractive production mechanism, note that if the ρ^o signal were produced by pure Pomeron exchange, then the pion-nucleon system produced at the nucleon vertex would remain in an isospin 1/2 state. Moreover, an isospin 1/2 state is expected to decay twice as often to the charge state $n\pi^+$ as to $\rho\pi^o$, inviting a comparison of these two channels. From Table V.1b, the ratio at 7.5 GeV is indeed consistent with two, 2.1±0.4. This is

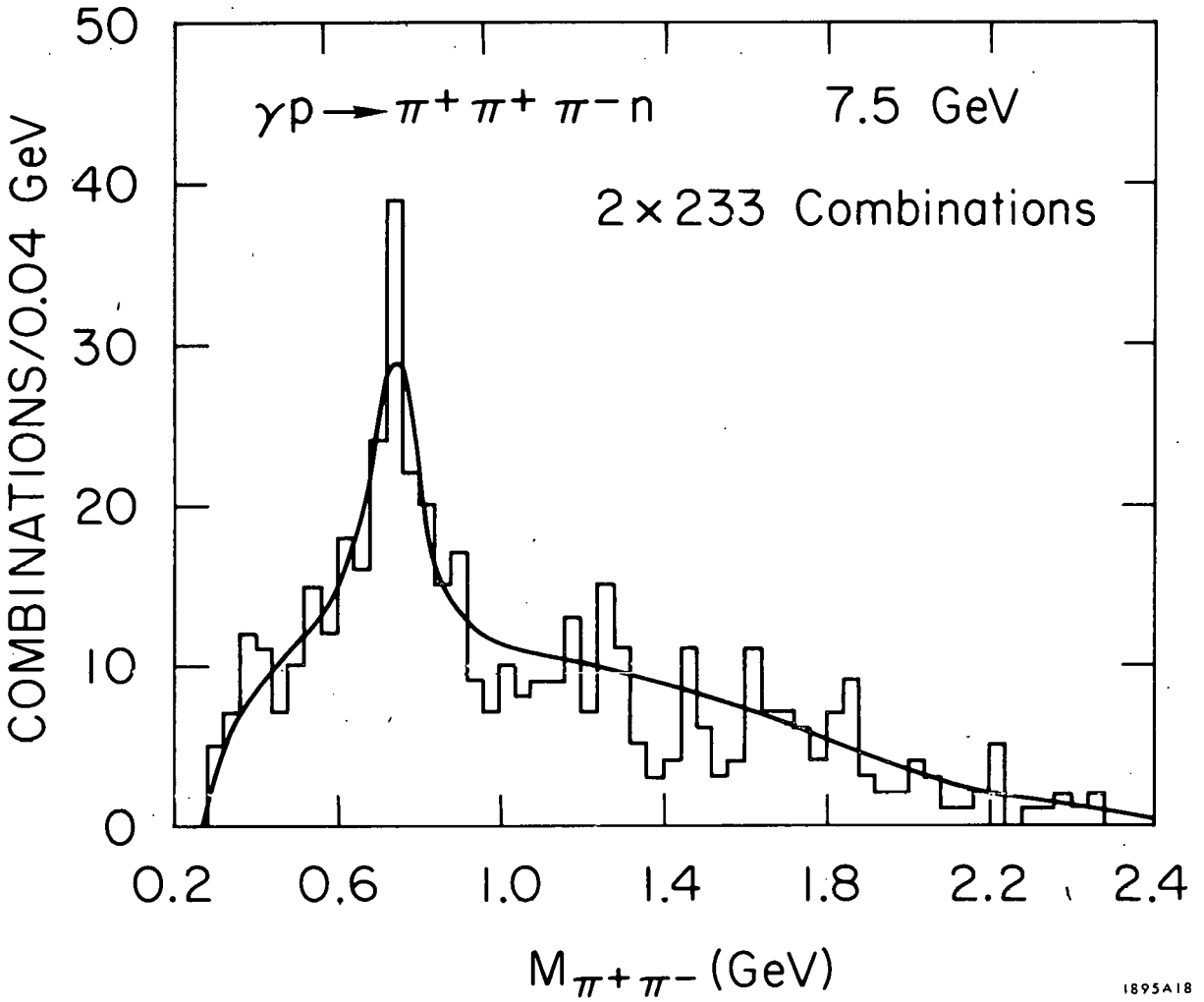

FIG. V.10-- $M(\pi^+\pi^-)$ for all 1-C fits to $\gamma p \longrightarrow \pi^+\pi^+\pi^-n$ with $0.6 < mm^2 < 1.2$ GeV^2 and $P(\chi^2) > 0.005$ in the 7.5 GeV data.

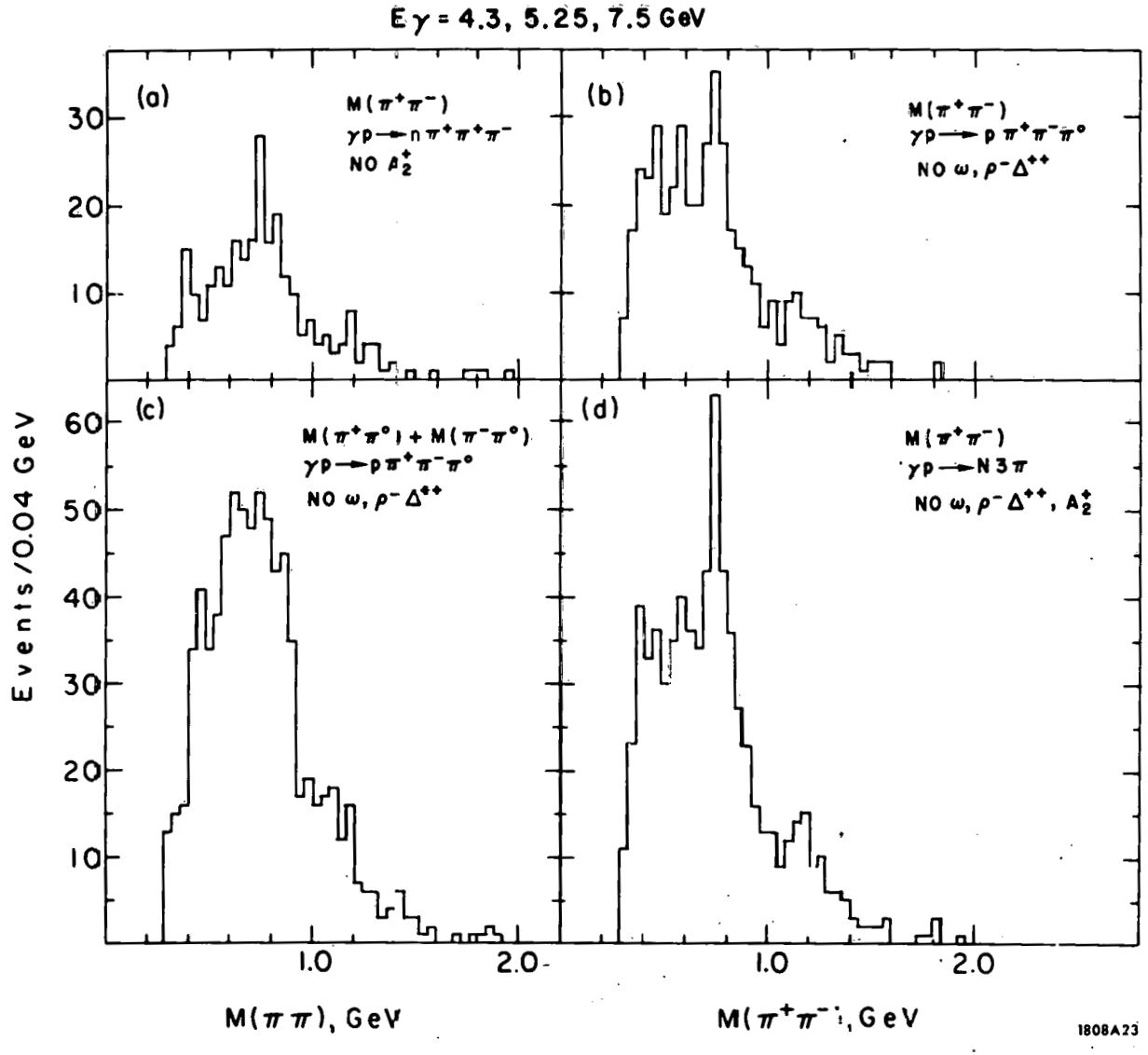

FIG. V.11-- Peripheral $M(\pi\pi)$ distribution ($|t(\gamma, \pi\pi)| \leq 0.5$ GeV^2) for reactions (III.1,2) at all energies. (a) $M(\pi^+\pi^-)$ for reaction (III.2) with A_2^+ events ($M(\pi^+\pi^+\pi^-)$=1.25-1.35 GeV) removed (b) $M(\pi^+\pi^-)$ for reaction (III.1), ω and $\rho^-\Delta^{++}$ events removed. (c) $M(\pi^+\pi^0)$ and $M(\pi^-\pi^0)$ for reaction (III.1), ω and $\rho^-\Delta^{++}$ removed. (d) Sum of (a) and (b).

consistent with the assumption of diffractive production. Also the results of the SBT collaboration for inelastic ρ^o production are consistent (within large errors) with twice as much ρ^o in the neutron channel and also with a natural parity exchange production mechanism.[31] However, it is not clear how to ascertain exactly what fraction of the unassociated ρ^o seen in each channel should be considered peripherally produced, so the usefulness of this ratio test is impaired. Also the large errors on all of these determinations as well as the systematic uncertainty in the correct ρ^o shape make this evidence far from compelling; indeed, the majority of this inelastic ρ^o production is associated with small momentum transfer to the final state nucleon rather than the final-state positively-charged pion-nucleon system. This latter fact tends to suggest that some three pion object is being produced diffractively which decays into a rho. Although this production mechanism is conceivable in the $\pi^+\pi^-\pi^o$ final state, there can be no diffractively produced 3-pion system in the neutron channel by charge conservation. Even in the proton channel, there is no obvious candidate for a diffractive three-pi system which could then decay into a $\rho^o\pi^o$.

If this peripherally produced ρ^o were associated with a "diffraction dissociation" process,[87] one could conclude that the ratio of elastic diffractive photoproduction to inelastic diffractive production is about 30($15\mu b/0.5\mu b$). This is similar to the ratios obtained in pion-nucleon and nucleon-nucleon reactions.[87] Unfortunately our small signal does not yield enough statistics to study this process in detail or even to prove that it is really diffractive. However, it is worth noting that when the invariant masses of the Nπ system associated with the ρ^o are plotted in Fig. V.12, no clear evidence is seen for

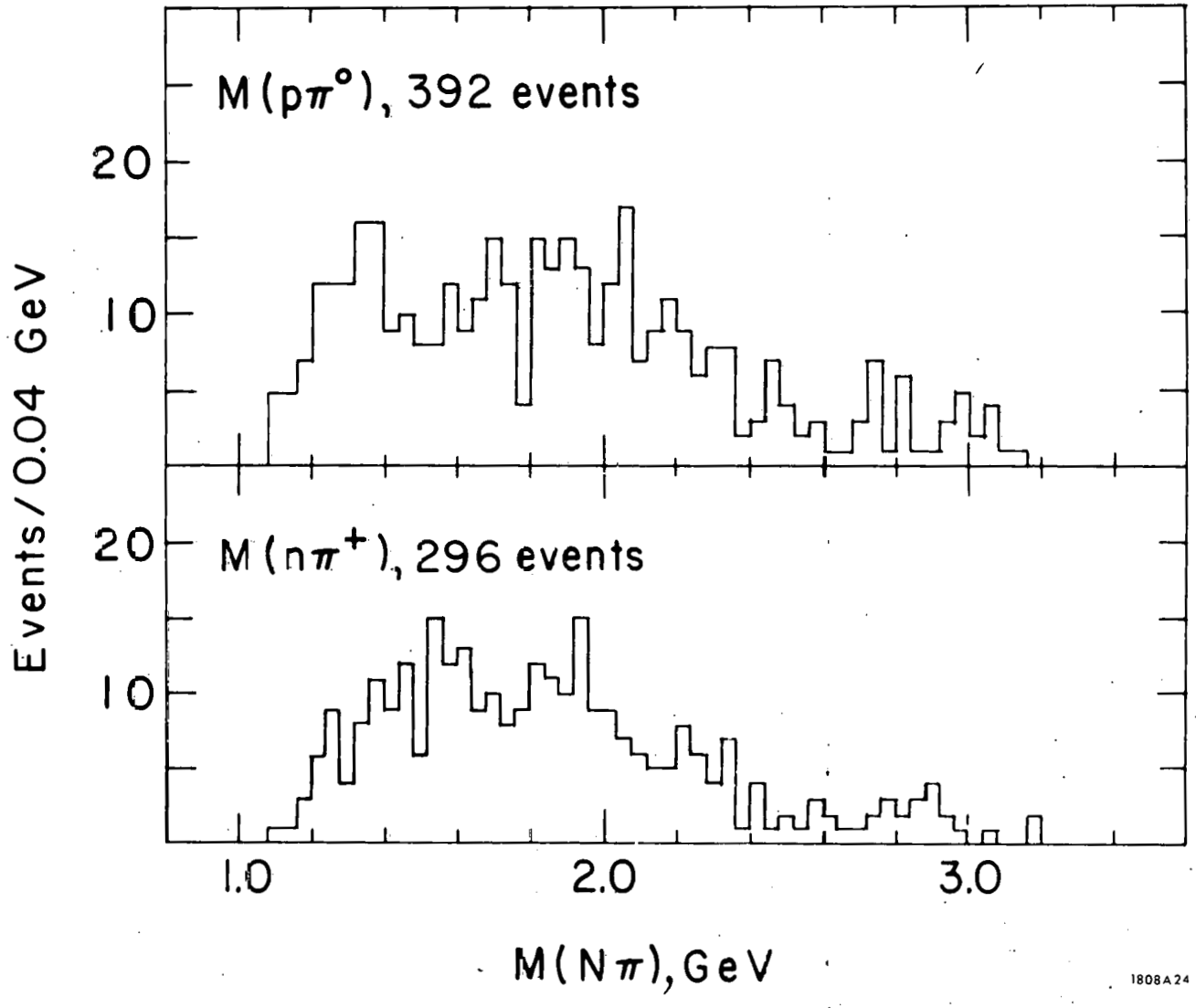

FIG. V.12-- $M(p\pi^0)$ and $M(n\pi^+)$ distribution in the reactions $\gamma p \longrightarrow p\pi^+\pi^-\pi^0$ and $n\pi^+\pi^+\pi^-$ respectively, for the events with $M(\pi^+\pi^-)=0.65$-0.85 GeV. ω, $\rho^-\Delta^{++}$, and A_2^+ events were removed from the sample. According to our fits about half the events in this figure originate in the reaction $\gamma p \longrightarrow \rho^0\pi N$.

the production of any of the known N*(I=1/2) resonances. It is possible that such an N* associated production would be seen at much higher photon energies.[24]

Finally, we wish to comment that the inelastic ρ production observed in this experiment, the final states $\rho^{o}\pi^{-}p$ and $\omega\pi^{-}p$ observed in γn reactions and the reactions $\gamma p \longrightarrow V^{o}\pi^{-}\Delta^{++}(V^{o}=\rho^{o},\omega)$ which were reported previously need not all have the same production mechanism. Some may be diffractive (like the ρ^{o} in Fig. V.11 above and the one observed in γn reactions),[82] others may be due to OPE (ω-production), and $\rho^{\pm}$ production may be due to charged vector meson exchange since the $\rho^{+}\rho^{-}\rho^{o}$ coupling could be large.[83] Much more extensive experiments would be required for the detailed study of these inelastic processes.

CHAPTER VI

CONCLUSIONS

Results on the photoproduction of neutral vector mesons and on the photoproduction of other 4-body final states have been presented in the preceding two chapters. The principal results are summarized here in the order of their appearance in the main body of the text.

Diffractive ρ^o Photoproduction (see Chapter IV.1): We confirm in our data the well established results of previous experiments,[9-12] namely that the ρ^o cross section is slowly decreasing above 2 GeV, which implies a largely diffractive production mechanism. This result holds whether the rho cross section is obtained from a phenomenological model,[16] the Söding interference model,[10,17] or a model-independent calculation using the double differential cross section. We extend previous observations[10,16] that s-channel helicity is conserved, possibly up to ~0.8 $(GeV/c)^2$, by our determination of the rho density matrix elements at 7.5 GeV. The data at 7.5 GeV are seen to be very cleanly separable into $p\rho^o$ and $\pi^-\Delta^{++}$ production, and no ρ' or higher mass recurrences, such as might be expected from the Venziano model,[15] are observed within stringent upper limits.

Omega Meson Production (see Chapter IV.2): Cross sections for omega production in the channel $\gamma p \longrightarrow p\pi^+\pi^-\pi^o$ are obtained in eight energy intervals between 1.2 and 8.2 GeV. A fit of these data to a constant plus a term proportional to E_γ^{-2} enables us to separate the "diffractive" and the one pion exchange (OPE) contributions to omega production. This mix of diffractive and OPE contributions is shown to reproduce the observed t dependence of the reaction $\gamma p \longrightarrow \omega p$.

Vector Dominance (see Section IV. 3): The omega forward cross section can be compared to our diffractive rho photoproduction to examine the predictions of the vector dominance model[14] plus SU(3).[18] We obtain the forward cross section ratio of 9.4±2.1 in agreement with simple SU(3) which predicts[19] a ratio of 9 and the value from the ORSAY storage ring results,[13] 7.5±1.5. Using the optical theorem[20] and existing total photoproduction cross section data,[21] our forward cross section data imply a value for $\gamma_\rho^2/4\pi$ of 0.32±0.03, which disagrees with the storage ring results[13] and heavy nuclei results,[12] but which does give a good agreement in both the s and t dependence with existing data on Compton scattering.[22]

Associated Rho-Delta Production (see Chapter V. 1): The energy dependence of the cross section for the reaction $\gamma p \longrightarrow \rho^- \Delta^{++}$ is shown to be inconsistent with the behavior expected on the basis of a simple OPE plus SU(3) calculation.[6] This raises the question as to whether the application[9,10] of these models in the derivation of the radiative decay width of the rho into a pion and a photon is valid and introduces new speculations about possible production mechanisms for this reaction.

Photoproduction of the A_2 Meson (see Section V. 2): The photoproduction of the A_2^+ meson was first observed in this experiment in the channel $\gamma p \longrightarrow \pi^+\pi^+\pi^- n$. In our combined data the signal is clear and is consistent with the usually accepted mass and width. An OPE model calculation has been used to estimate the strength of the $A_2\pi\gamma$ coupling, a decay mode not directly observed. The cross sections, however, are not only much smaller than those for $\rho^-\Delta^{++}$ production, but also they decrease more rapidly with energy, making it difficult to reach any firm conclusions on the production mechanism from this amount of data. Although A_2^o production in the channel

$\gamma p \longrightarrow p\pi^+\pi^-\pi^o$ could be neither diffractive nor OPE by spin and isospin conservation, there is a peripheral enhancement at exactly this mass in the 7.5 GeV data for which an upper limit is given. Very similar low mass enhancements in the neutral pi-rho system have been observed in 8 GeV/c π^+d interactions.[23] This similarity extends to several other features of this distribution.

Inelastic Rho Production (see Chapter V.3): A very large amount of the remaining events in the 4 body final states is due to rho production not observed to be associated with the production or decay of other resonances. It has been suggested[24] that some of the ρ^o signal may be produced diffractively, which is consistent with our data, but the presence of strong charged rho signals may indicate a significant vector meson exchange in these final states.

REFERENCES

1. J. Ballam, et al., Phys. Rev. Letters, 22, 1541 (1968); 22, 1544 (1968).
2. J. Ballam, et al., Phys. Letters, 30B, 421 (1969).
3. Y. Eisenberg, et al., Phys. Rev. Letters, 22, 669 (1969).
4. Y. Eisenberg, et al., Phys. Rev. Letters, 23, 1322 (1969).
5. Y. Eisenberg, et al., Phys. Letters, 34B, 439 (1971).
6. J. Ballam, et al., Phys. Rev. Letters, 26, 995 (1971).
7. J. Ballam, et al., Report Number SLAC-PUB-933 (1971), to be published.
8. J. Ballam et al., Nucl. Instr. and Methods, 73, 53 (1969).
9. Cambridge Bubble Chamber Group, Phys. Rev., 146, 994 (1966); 155, 1468 (1967); 169, 1080 (1969).
10. Aachen-Berlin-Bonn-Hamburg-Heidelberg-München Collaboration, Phys. Rev., 175, 1669 (1968); 188, 2060 (1969).
11. M. Davier, et al., Phys. Rev., D1, 790 (1970).
12. G. McClellan, et al., Phys. Rev. Letters, 22, 374 (1969); H. Blechschmidt, et al, Nuovo Cimento, 52A, 1348 (1967); H. Alvensleben, et al., Phys. Rev. Letters, 23, 1058 (1969); W. G. Jones, et al., Phys. Rev. Letters, 21, 586 (1969); M. Davier, et al., Phys. Rev. Letters, 21, 841 (1968); Phys. Letters, 28B, 619 (1969); R. Anderson, et al., Phys. Rev., D1, 27 (1970).
13. J. E. Augustin, et al., Phys. Letters, 28B, 503 (1969).
14. J. J. Sakurai, Ann. Phys., 11, 1 (1960); M. Gell-Mann and F. Zachariasen, Phys. Rev., 124, 953 (1961); L. Stodolsky, Phys. Rev. Letters, 18, 135 (1967); see also Ref. 49 for many specific calculations.

15. G. Veneziano, Nuovo Cimento, 57A, 190 (1968); J. G. Cordes and P. J. O'Donnel, Phys. Rev. Letters, 20, 146 (1968); J. A. Shapiro, Phys. Rev., 179, 1345 (1969).

16. H. H. Bingham, et al., Phys. Rev. Letters, 24, 955 (1970); J. Ballam, et al., Phys. Rev. Letters, 24, 960 (1970).

17. P. Soding, Phys. Rev. Letters, 19, 702 (1965); A. S. Krass, Phys. Rev., 159, 1496 (1967).

18. M. Gell-Mann and Y. Ne'eman, eds., The Eightfold Way (W. A. Benjamin, New York, 1964). See also Chaptor 14 of Ref. 49.

19. H. J. Lipkin, Phys. Rev. Letters, 16, 1015 (1966); H. Harari, Phys. Rev., 155, 1565 (1967).

20. Z. G. T. Guiragossián and A. Levy, Nucl. Phys., B11, 449 (1969).

21. D. O. Caldwell, et al., Phys. Rev. Letters. 25, 609, 613 (1970).

22. R. L. Anderson, et al., Phys. Rev. Letters, 25, 1218 (1970); A. M. Boyarski, et al., Report Number SLAC-PUB-872 (1971).

23. W. N. Bugg, et al., Phys. Rev. Letters, 23, 146 (1969).

24. G. Wolf, Nucl. Phys., B26, 317 (1971).

25. R. H. Milburn, Phys. Rev. Letters, 10, 75 (1963); R. H. Milburn, Report No. SLAC-41, 1965 (unpublished).

26. C. K. Sinclair, J. J. Murray, P. Klein, and M. Rabin, IEEE Trans. on Nucl. Sci., NS16, 1065 (1969).

27. J. Ballam, et al., Phys. Rev. Letters, 23, 498 (1969).

28. J. Ballam, et al., Phys. Rev. Letters, 24, 1364 (1970).

29. H. Bingham, et al., Phys. Rev. Letters, 25, 1223 (1970).

30. K. C. Moffiet, "Bubble Chamber Study of Polarized $\gamma p \longrightarrow \pi^+\pi^- p$ at 2.8 and 4.7 GeV" (Ph.D. thesis), UCRL 19890 (1970) (unpublished).

31. W. J. Podolsky, Photoproduction of Omega Mesons in a Hydrogen Bubble Chamber by 3 and 5 GeV Linearly Polarized Photons (Ph.D. thesis), UCRL 20128 (1971) (unpublished).

32. J. Ballam, et al., Report Number SLAC-PUB-941 (1971), to be published.

33. D. M. Binnie, Nucl. Instr. and Methods, 10, 212 (1961).

34. Y. Tsai, Phys. Rev., 137B, 730 (1965).

35. J. Ballam and Z. Guiragossián, Report Number SLAC-PUB-41 (1964) (unpublished).

36. A. Dufner, S. Swanson, Y. Tsai, Report Number SLAC-67 (1966).

37. G. Chadwick, SLAC-TN-66-13 (1966) (unpublished).

38. A. Levy and G. Wolf, SLAC-TN-68-16 (1968) (unpublished).

39. F. T. Solmitz, A. D. Johnson and T. B. Day, THREE VIEW GEOMETRY PROGRAM, Alvarez Group Programming Note P-117, Lawrence Radiation Lab (LRL)-Berkeley (1966); O. I. Dahl, T. B. Day. F. T. Solmitz and N. C. Gould, SQUAW, Alvarez Group Programming Note P-126, LRL-Berkeley (1968) (unpublished).

40. H. Spitzer, "Photoproduction of Rho Mesons in a Hydrogen Bubble Chamber at Photon Energy Levels up to 5.8 GeV" (Ph.D. thesis), SLAC-TRANS-79 (1967) (unpublished).

41. A. H. Rosenfeld and W. E. Humphrey, Ann. Rev. Nucl. Sci., 13, 103 (1963).

42. G. Wolf, SLAC-TN-68-13 (1968) (unpublished).

43. E. Burns and D. Drijard, PHONY, Trilling-Goldhaber Group Technical Note 143, LRL-Berkeley (1968) (unpublished).

44. T. M. Knasel, DESY 70-2/3 (1970) (unpublished).

45. J. Jost, J. Luttinger and M. Slotnik, Phys. Rev., 80, 189 (1950).

46. D. Notz, Diplomarbeit Universität Hamburg (see Ref. 44).

47. See Section 2.6 of Ref. 41 for a detailed discussion of this point.

48. J. Shapiro, Suppl. Nuovo Cimento, 18, 40 (1960).

49. B. T. Feld, Models of Elementary Particles (Braisdell Co., Waltham, 1969). For VDM see Sections 14.3.2, 15.3.2 and 17.1.3.

50. L. Criegee, et al., Phys. Letters, 28B, 282 (1968); G. Diambrini-Palazzi, et al., Phys. Rev. Letters, 25, 478 (1970).

51. A. M. Boyarski, et al., Phys. Rev. Letters, 22, 148 (1969); 25, 695 (1970).

52. G. McClellan, et al., Phys. Rev. Letters, 23, 718 (1969); N. Hicks, et al., Phys. Letters, 29B, 602 (1969); R. Anderson, et al., Phys. Rev., D1, 27 (1970); F. Bulos, et al., Phys. Rev. Letters, 26, 149 (1971); H. Alvensleben, et al., Phys. Rev. Letters, 26, 273 (1971).

53. There is no consensus about whan an "unskewed" rho should look like, so here we compare with the s-wave nonrelativistic form using m_ρ=765 MeV, Γ_ρ=140 MeV, arguing that it gives a minimum expected intensity, e.g., see H. Harari and Y. Zarmi, Phys. Rev., 187, 2230 (1969).

54. M. Ross and L. Stodolsky, Phys. Rev., 149, 1172 (1966).

55. G. Kramer and J. L. Uretsky, Phys. Rev., 181, 1918 (1969); P. D. Mannheim and U. Maor, Phys. Rev., D2, 2105 (1970).

56. S. Drell, Phys. Rev. Letters, 5, 278 (1960).

57. E. Ferrari and F. Selleri, Phys. Rev. Letters, 7, 387 (1969); J. Benecke and H. P. Durr, Nuovo Cimento, 56A, 269 (1968). The use of such form factor improves the fits, but may be questionable in photoproduction (D. R. Yennie, private communication).

58. J. Pumplin, Phys. Rev., D2, 1859 (1970); T. Bauer, Phys. Rev. Letters, 25, 485 (1970). Thanks to D. R. Yennie for discussion of this.

59. J. D. Jackson, Nuovo Cimento, 34, 1644 (1964).

60. D. R. Yennie (private communication).

61. With all momenta transformed to the rest system of the dipions, the helicity system z-axis is taken opposite the recoil proton direction, the y-axis in the direction of $\vec{p}_{recoil}$, $\vec{xk}$, where $\vec{k}$ is the photon momentum and $\hat{x}=\hat{y}x\hat{z}$; the π^+ direction is the polarization analyzer.

62. It has been suggestion that helicity conservation is an asymptotic property of diffraction scattering, see F. J. Gilman, et al., Phys. Letters, 31B, 387 (1970).

63. D. R. O. Morrison, Phys. Letters, 22, 528 (1966); A. Shapira, et al., Nucl. Phys., B23, 583 (1970); Z. M. Ma, et al., Phys. Rev. Letters, 24, 1031 (1970).

64. With all momenta transformed to the $p\pi^+$ rest system, the Jackson system z-axis is taken along the direction of the incoming proton, the y-axis in the direction $\vec{\pi}\vec{x}\vec{p}_{in}$, and $\hat{x}=\hat{y}x\hat{z}$, with the outgoing proton as the spin analyzer.

65. H. Harari, Proceedings of the 4th International Symposium on Electron and Photon Interactions at High Energies, Liverpool, England, Sept., 1969, edited by D. W. Braben (Daresbury Nuclear Physics Laboratory, Daresbury, Lancashire, U.K. 1970), p. 115.

66. B. Haber and G. Yekutieli, Phys. Rev., 160, 1410 (1967).

67. M. Damashek and F. J. Gilman, Phys. Rev., D1, 1319 (1970).

68. Y. Eisenberg, et al., Phys. Rev. Letters, 25, 764 (1970); Nucl. Phys., B25, 499 (1971); preprint WIS 71/9, to be published.

69. See analysis of G. Wolf, DESY report 70/64 (unpublished).

70. R. Diebold and J. A. Poirier, Phys. Rev. Letters, 20, 1532 (1968); 22, 906 (1969); Z. Guiragossián and A. Levy, Ref. 20. A recent comparison is given by D. Schildknecht, DESY report 70/31.

71. F. Bulos, et al., Report Number SLAC-PUB-855 (1971), to be published.

72. R. L. Anderson, et al., Contribution to the International Conference on High Energy Physics, Kiev (Sept. 1970).

73. A. Schwimmer and D. R. Yennie, private communication.

74. J. Friedman, MURTLEBERT, Group A Programming Note p-156, LRL-Berkeley (1966) (unpublished).

75. H. Harari, Phenomenological Duality, SLAC-PUB-914, to be published in Proceedings of the International Conference on Duality and Symmetry in Hadon Physics, Tel-Aviv, Israel, April, 1971.

76. Peripheral phase space is just the usual Lorentz invariant phase space multiplied by factors e^{Bt} for appropriate momentum transfers. This technique has also been used to improve the fits to these final states by A. Levy.

77. See Shapira, Ref. 63, and also the data compilation of J. D. Hansen CERN report HERA 70-2 (1970) (unpublished).

78. B. E. Y. Svensson, High Energy Phenomenology and Regge Poles, CERN 67-24, pp. 59-61 (1967) (unpublished). The relation $R^2 \simeq 4B$ can also be derived simply from the fact that $\sigma_T = 2\pi R^2$ and $\sigma^{el} = \pi R^2$ in the black disk model for scattering, using the optical theorem and $d\sigma^{el}/dt = A\exp(Bt)$.

79. M. Roos, et al., (Particle Data Group), Phys. Letters, 33B, August, 1970.

80. G. Wolf, Phys. Rev., 182, 1538 (1969).

81. See Ref. 79. The upper limit on the rho-pi-gamma width is given by G. Fidecaro, et al., Phys. Letters, 23, 163 (1966).

82. Y. Eisenberg, et al., Phys. Rev. Letters, 25, 764 (1970); Nucl. Phys., B25, 499 (1971); preprint WIS 71/9 (1971), to be published.

83. S. M. Berman and U. Maor, Nuovo Cimento, 36, 483 (1965); R. B. Clark, Phys. Rev., 187, 1993 (1969) and D1, 2152 (1970); M. Gluck and S. Wagner, Phys. Rev. (1971), to be published.

84. R. T. Poe, et al., Phys. Rev. Letters, 22, 551 (1969).

85. A_2 mass and width, see Ref. 79.

86. For the derivation of the appropriate OPE formula for the A_2 see H. Hogassen, et al., Nuovo Cimento 42A, 323 (1966). See in particular Appendix A, Eq. (A11) for the derivation of Eq. (V.7).

87. M. L. Good and W. D. Walker, Phys. Rev., 120, 1854 (1960). See also D. R. O. Morrison, Rapporteur's talk at the Kiev Conference (1970) and CERN/PHYS 70-64.